ITO BASED TRANSPARENT AND CONDUCTING THIN FILMS FOR SPACE, SOLAR ENERGY AND FLEXIBLE ELECTRONICS APPLICATIONS

Thesis

Submitted in partial fulfilment of the requirements for the degree of

DOCTOR OF PHILOSOPHY

by

SIBIN K. P.

DEPARTMENT OF PHYSICS
NATIONAL INSTITUTE OF TECHNOLOGY KARNATAKA,
SURATHKAL, MANGALORE-575025
August, 2018

DECLARATION
By the Ph.D Research Scholar

I hereby declare that the Research Thesis entitled **"ITO based transparent and conducting thin films for space, solar energy and flexible electronics applications"** which is being submitted to the *National Institute of Technology Karnataka, Surathkal* in partial fulfilment of the requirements for the award of the Degree of **Doctor of Philosophy** in **Physics** is a *bonafide report of the research work carried out by me*. The material contained in this Research Thesis has not been submitted to any University or Institution for the award of any degree.

_____

Sibin K. P.
(Register No. 145001PH14P03)
Department of Physics

Place: NITK, Surathkal
Date:

CERTIFICATE

This is to *certify* that the Research Thesis entitled **"ITO based transparent and conducting thin films for space, solar energy and flexible electronics applications"** submitted by Sibin K. P. (Register Number: **145001PH14P03**) as the record of the research work carried out by him, is accepted as the Research Thesis submission in partial fulfilment of the requirements for the award of degree of **Doctor of Philosophy**.

Research Supervisors

Dr. H. D. Shashikala
Professor
Dept. of Physics
NITK, Surathkal
Date:

Dr. Harish C. Barshilia
Chief Scientist and Head
Surface Engineering Division
CSIR-NAL, Bangalore
Date:

Chairman-DRPC
(Signature with Date and Seal)

Dedicated to my beloved family and gurus

ACKNOWLEDGEMENT

ABSTRACT

This thesis reports deposition, optimization and investigation of properties of transparent and conducting ITO and ITO/Ag/ITO multilayer thin films for space, solar energy and flexible electronics applications. ITO thin films were deposited on various substrates by pulsed direct current reactive magnetron sputtering system using an In:Sn (90-10 wt.%) alloy target. The influence of the deposition parameters (argon and oxygen flow rates, and substrate temperature) and effect of coating thickness on the optical, electrical, structural and microstructural properties of ITO thin films deposited on flexible fluorinated ethylene propylene (FEP) substrates was investigated in detail. The optimized ITO coating (10-15 nm thick) on FEP substrate exhibited high IR emittance (>75%), high average solar transmittance (>90%) and moderate sheet resistance (2-10 kΩ/square) needed for spacecraft application. Stability of the ITO coatings on FEP, Kapton® and aluminized Kapton® substrates was studied in simulated space environments. Environmental tests such as: relative humidity, thermal cycling and thermo vacuum were performed. Thermo-optical properties and sheet resistance of ITO coated FEP and Kapton® substrates were studied before and after environmental tests. In another objective of the thesis, ITO/Ag/ITO (IAI) multilayer coatings were designed for spectral beam splitter and flexible electronic applications and these coatings were deposited on glass, and flexible FEP and Kapton® substrates by magnetron sputtering method at room temperature. The thicknesses of the component layers, namely, Ag and ITO were varied to achieve high visible transmittance, high NIR-IR reflectance, low sheet resistance, and optimum cut-off wavelength. The optimized IAI multilayers for solar segregator application exhibited high visible transmittance (~91%) and high NIR-IR reflectance (>90%) with an optimum cut-off wavelength of ~900 nm. The optimization of IAI multilayer coatings for transparent conductor also reported in this thesis. High visible transmittance (~ 91%) and low sheet resistance ~7.1 Ω/square were achieved for IAI multilayer deposited on flexible FEP substrate.

Keywords: Transparent conductors, Indium tin oxide (ITO), ITO/Ag/ITO multilayers, Sputtering, FEP, Kapton®, Beam splitter, Flexible electronics.

CONTENTS

LIST OF FIGURES

LIST OF TABLES

ABBREVIATIONS

AFM	Atomic force microscopy
ASTM	American society for testing and materials
DC	Direct current
FEP	Fluorinated ethylene propylene
FESEM	Field emission electron microscopy
FOSR	Flexible optical solar reflector
FTIR	Fourier transform infrared spectroscopy
GEO	Geostationary earth orbits
HF	Hydrofluoric acid
IAI	ITO/Ag/ITO
IPA	Isopropyl alcohol
ITO	Indium tin oxide
IR	Infrared
JCPDS	Joint committee on powder diffraction standards
MLI	Multilayer insulation
NIR	Near-infrared
PES	polyethersulfone
PET	Polyethylene terephthalate
PMT	Photomultiplier tube
PV	Photovoltaic
RF	Radio frequency
RH	Relative humidity
RT	Room temperature
SCCM	Standard cubic centimetre per minute
TC	Thermal cycling
TCO	Transparent conducting oxides
TEG	Thermoelectric generator
THM	Transparent heat mirrors
TMP	Turbo molecular pump
TM	Transverse magnet

TE	Transverse electric
TVAC	Thermo-vacuum
URA	Universal reflectance accessory
UV	Ultra violet
VIS	Visible
XPS	X-ray photoelectron spectroscopy
XRD	X-ray diffraction

NOMENCLATURE

α	Absorptance
ά	Absorbance
ε	Emittance
ε_0	Permittivity of free space
ε_∞	Relative permittivity
ω_p	Plasma frequency
Ω	Ohm
λ	Wavelength
λ_c	Cut-off wavelength
ρ	Resistivity
ϕ	Figure of merit of transparent conductors
^{o}C	Degree Celsius
Å	Angstrom
m^*	Effective mass of the charge carrier
μm	Micrometre
a	Lattice parameter
Ar	Argon
Ag	Silver
c	Speed of light
C	Carbon
cm	Centimetre
e	Electron
E_F	Fermi energy level
E_p	Photon energy
E_g	Optical band gap energy
F	Fluorine
Hz	Hertz
I	Current
In	Indium

In_2O_3	Indium oxide
k_0	Extinction coefficient
k	Kilo
lit	Litre
M	Mega
ml	Millilitre
mm	Millimetre
m	Meter
N	Charge carrier density
n	Refractive index
n_s	Refractive index of the substrate
n_{Ag}	Refractive index of Ag
n_{ITO}	Refractive index of ITO
nm	Nanometre
O	Oxygen
pO_{2min}	Minimum partial pressure of oxygen
R	Total solar spectrum reflectance
R_a	Average roughness
$R_{av.}$	Average reflectance of solar spectrum
$R_{NIR.}$	Average reflectance in the NIR region of the spectrum
R_S	Sheet resistance
$R_{ITO(top)}$	Sheet resistance of top ITO layers
$R_{ITO(bootom)}$	Sheet resistance of bottom ITO layers
R_{Ag}	Sheet resistance of middle Ag layer
sec	Second
Sn	Tin
SnO_2	Tin oxide
t	Thickness
T	Total solar spectrum transmittance
$T_{av.}$	Average transmittance of solar spectrum
T_{vis}	Average transmittance in the visible region of the spectrum
T_s	Substrate temperature

V	Voltage
V_{CPD}	Contact potential difference
$V_0^{\bullet\bullet}$	Oxygen vacancy
W	Watt
Z	Figure of merit of beam splitter

CHAPTER 1

INTRODUCTION

Generally, most of the transparent materials are intrinsically insulators, but by incorporating an additional conducting coating on these substrates it is possible to make them electrically conducting yet optically transparent. Optically transparent and electrically conducting materials have enormous applications in energy and information technologies. This Chapter gives an overview about transparent conductors and their importance in solar, space and flexible electronic applications. It also outlines the objectives of the present thesis.

1.1   Transparent conductors

Transparent and conducting materials or transparent conductors (TCs) constitute a unique class of materials which combine two physical properties together - high optical transparency and high electrical conductivity. These properties are generally considered to be mutually exclusive of each other since high conductivity is a property possessed by metals while optically transparent materials are usually insulators. The ability to engineer materials that are simultaneously conductive, stretchable, and transparent is essential for emerging applications in flexible displays, solar cells, wearable electronics, artificial skin, conformable sensors, actuators, etc. (Bagal et al., 2015; Ellmer, 2012; Granqvist, 2007; Hecht et al., 2011). Transparent conductors show a transmission window in visible region of the solar spectrum (see Figure 1.1). At higher wavelength region the transmittance is decreased due to the reflection from charge carriers and at lower wavelength due to the band gap of the material (Edwards et al., 2004).

TCs have been known ever since the beginning of the 20th century. In 1907 Badeker had found that thermally oxidized CdO, Cu_2O and PbO thin films showed good electrical conductance with optical transparency (Badeker, 1907). However, the real application of TCs increased during the Second World War. One of the first use of TCs

is as a defrosting heating layer for the fighter plane cockpit windows, which allowed it to fly at high altitude during the war (Ellmer, 2012). Following the development of electronic industry after the World War, TCs were extensively investigated for optoelectronic devices. Thereafter, the demand of TCs has increased for a variety of applications. The actual and potential applications of TCs include: transparent electrodes for photovoltaic cells, transparent thin film transistors, transparent electrodes for flat panel displays, electrode for organic light emitting diodes (OLED), antistatic films, aircraft wind shields, anti-reflection coating, transparent electromagnetic shields, low emissivity windows, window defrosters, semiconductor lasers, etc. (Chopra et al., 1983; Ellmer, 2012; Gordon, 2000; Granqvist, 2007; Lampert, 2003).
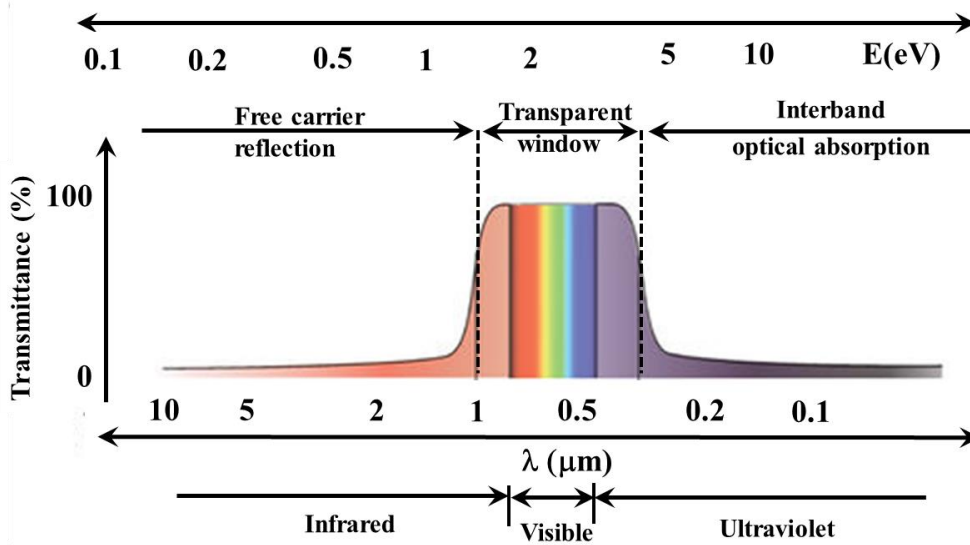
Figure 1.1: Schematic of the ideal transparent window of transparent conductors (Zhang et al., 2015)

1.2   Different transparent conductors

Following the findings of Badeker, scientists carried out investigation for developing different TCs (Chopra et al., 1983; Ellmer, 2012; Gordon, 2000). They found that some doped metal oxides show good conductance with good optical transparency; these are called transparent conducting oxides (TCOs). TCOs are the most important category in TCs. The peculiar combination of optical and electrical properties in TCOs is achieved by generating free electrons or hole carriers in metal

2

oxide semiconductors having a sufficiently large energy band gap (i.e., $\geq$ 3 eV), so that it is nonabsorbing or transparent to visible light (Coutts et al., 2000; Ramamoorthy et al., 2006; Stadler, 2012; Yu et al., 2016). In TCOs, charge carriers are usually generated by oxygen vacancies, doping the insulator with suitable dopants and also by defects (Edwards et al., 2004; Tahar et al., 1998). The coexistence of optical transparency and electrical conductivity in TCO films depends on the crystal structure, morphology, thickness, presence of intrinsic or intentionally introduced defects, etc. (Hao et al., 2008; Khusayfan and El-Nahass, 2013; Yu et al., 2016; Zhang et al., 2012). For a novel TCO material electrical resistivity will be $>10^{-4}$ Ω.cm, transmittance > 85% and optical band gap more than 3 eV with very low absorption coefficient in the visible range of the solar spectrum. Tin-doped indium oxide or indium tin oxide (ITO), aluminium doped ZnO, gallium doped ZnO, fluorine or manganese doped SnO_2 are the important TCOs (Agarwal et al., 2013; Singh et al., 2014; Stadler, 2012).

Thin metal films, metal nanowires, metal meshes, carbon nanotubes, graphene, conductive polymer, etc. are other TCs found in the literature (Ahn and Hong, 2014; Boscarino et al., 2014; Hecht et al., 2011; Jang et al., 2013; Layani et al., 2014; Sattler, 2016). Extensive research is still going on to find out new TCs or to improve the properties of the existing TCs.

1.3   Comparison of transparent conductors

The choice of TCs for a particular applications depends on its conductance, transparency, preparation cost, stability, adhesion on the substrates, ability to pattern, large area of deposition, etc. Therefore, a comparison of few properties of different TCs is shown in Figure 1.2. It can be seen from Figure 1.2 (a) that the transmittance and sheet resistance of all the TCs are inversely proportional, when the sheet resistance decreases transmittance also decreases. However, Ag nanowires, metal meshes, ITO and graphene show very high transmittance with very low sheet resistance. Another important factor of TCs to be considered is their cost. For applications such as space, cost of the TCs may not be a prime criteria, but it needs TCs with supreme quality and stability which can withstand the harsh space environments. However, the industrial applications needs TCs with the lowest cost, otherwise, the product will not be economically feasible. Figure 1.2 (b) shows the cost and conductance of different TCs.

3

The conductive polymer can be prepared at very low cost, but its conductance is very low compared to other TCs. Metal nanostructures show better conductance with the lowest cost. Graphene is a good candidate for very high conducting applications, but its preparation cost is very high. Among these TCs ITO is the most studied and is used for various applications. ITO is an average candidate in the case of conductance and cost. Metal nanostructures can be available for low cost, but they are limited in many applications due to their instability, corrosion, discontinuous film formation at the low thickness, etc. In addition to the superior transparency and conductivity, good stability and ease of pattering to make transparent circuitry and transparent electrodes for optoelectronic device applications makes ITO as the premium TC (Granqvist and Hultåker, 2002). ITO has a very long history. An ITO related patent, filed in 1947 (US Patent #2564707), was found in literature (Hecht et al., 2011). Although ITO has long been known, even today plenty of researchers are studying ITO because of its unmatchable importance in optoelectronic applications (Chen et al., 2016; Im et al., 2016; Peng et al., 2017; Remya and Deb, 2017; Wang et al., 2017). However, due to the extensive use of ITO in many applications, the indium resource in the earth has decreased. But, the recent developments in the recycling of indium metal from used and discarded devices has decreased the worry of extinction of indium metal from the earth (Dang et al., 2017, 2015; Zimmermann et al., 2014).
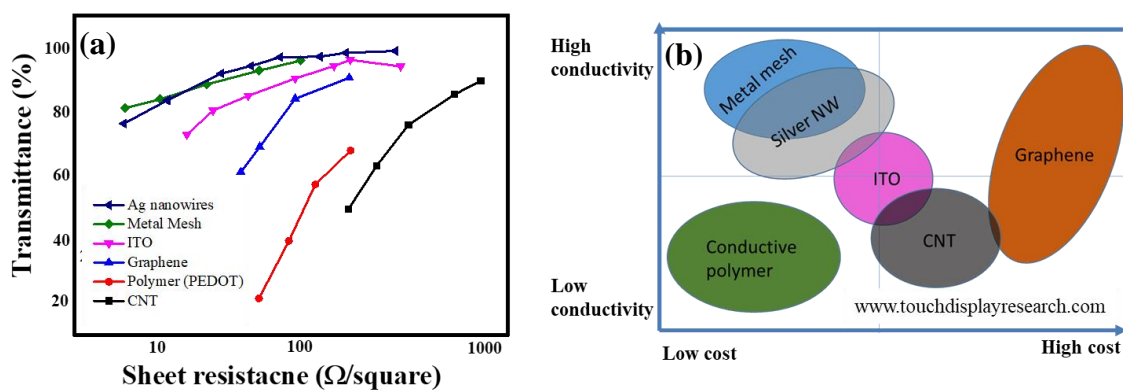
Figure 1.2: Comparison of different TCs: (a) transmittance vs. sheet resistance (b) cost vs. conductance (Colgrove, 2016).

4

1.4   Basic properties of ITO

Tin (IV) doped indium (III) oxide (In_2O_3: Sn) or indium tin oxide (ITO) is a highly degenerate n-type semiconductor having wide band gap (3.1-4.2 eV) (Bierwagen, 2015). Tin concentration in ITO may vary from 5-15%. It has very good electrical conductivity (10^3- 10^4 Ω^{-1} cm^{-1}) and optical transparency (80-95%). In bulk form, ITO is a yellowish solid but when its thickness reduces to few nanometres it shows colourless transparent nature. The density of ITO is 7.12 g/cm^3 and melting point is ~1900 ^oC. Similar to indium oxide, ITO shows a peculiar body-centered cubic bixbyite crystal structure (C-type, rare earth sesquioxide structure, space group 206, Ia3) with a lattice parameter a = 1.0117 nm (Fuchs and Bechstedt, 2008; Rosen and Warschkow, 2009) . The conventional unit cell contains 80 atoms or 16 formula units. This resembles fluorite 2 x 2 x 2 supercell. In this structure 25% of all oxygen anion sites are vacant and the oxygen vacancies are located along the four <111> axes. Depending on the relative positioning of anion vacancies, two types of indium sites exist in the unit cell. They are termed b and d site in Wyckoff notation (Inerbaev et al., 2007). Figure 1.3 shows the cubic bixbyite structure and two non-equivalent sites of indium cations in the In_2O_3 crystal. Out of 32 In ions 8 are occupied at b position, and remaining 24 In ions occupy d position.
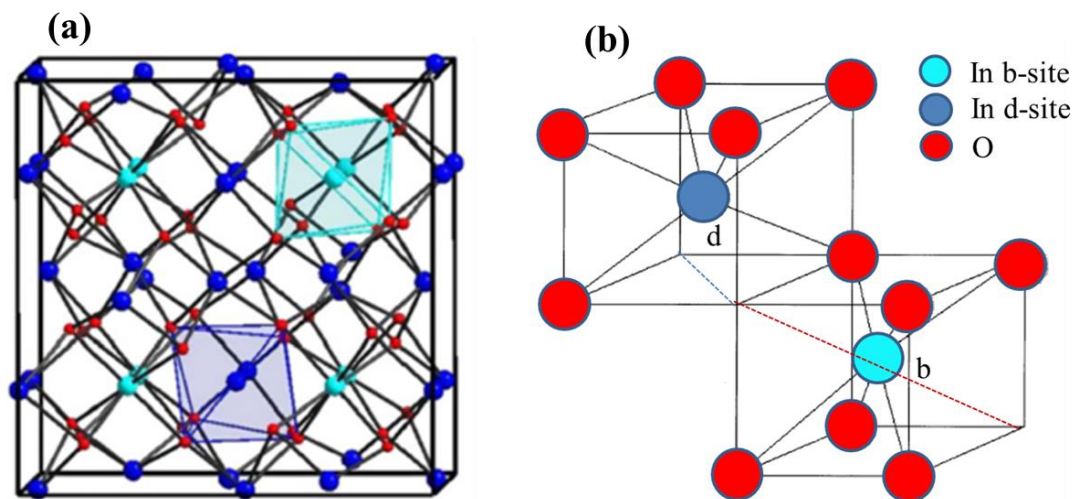
Figure 1.3:   (a) Cubic bixbyite unit cell (Karazhanov et al., 2007) (b) non-equivalent sites of indium cation In bixbyite structure (Quass et al., 1998).

1.4.1 Electrical and optical properties of ITO

Even though ITO is an oxide, the best ITO thin films show high electrical conductivity ($\sim 10^4$ Ω^{-1}cm^{-1}) and high optical transparency (>80%) in the visible range of the solar spectrum. In ITO, the electrical conductivity is mainly due to the doping of Sn^{4+} for In^{3+} and the presence of oxygen vacancies. Optimized ITO thin films contain 5-15% concentration of Sn^{4+} ions hosted in the site of In of the In_2O_3 structure. While Sn^{4+} replaces an atom of In^{3+} in ITO structure, an unpaired electron will get free from the bond. Oxygen vacancies provide electrons by acting as charged donors, this is generally symbolized by $V_0^{\bullet\bullet}$. Oxygen vacancy acts as a doubly ionized donor and one oxygen vacancy contributes two electrons to the electrical conductivity as shown in the following equation (Tahar et al., 1998).

$$O_0^X \rightarrow \frac{1}{2}O_{2(g)} + V_0^{\bullet\bullet} + 2e' \qquad (1.1)$$
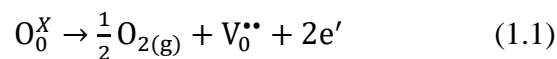
Oxygen vacancy forms shallow donor states just below the conduction band edge that trap two electrons per oxygen vacancy. The doping and oxygen vacancies result in the formation of the shallow donor or impurity states located close to the host (In_2O_3) conduction band. These electrons are thermally excited even at room temperature and move into the host conduction band (Edwards et al., 2004). The electrical conductivity of ITO thin film depends on this degenerate gas of current-carrying free electrons created in the conduction band and leaving the host band gap intact. Figure 1.4 shows the energy band diagram of ITO. This way the electrically conducting film remains optically transparent in the visible region. For describing the electronic structure of both the pure and doped materials Fan and Goodenough (1977) developed a one-electron electronic model.
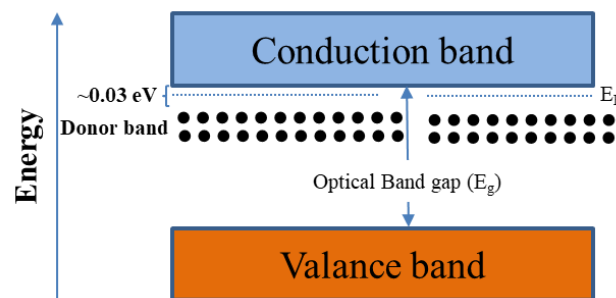
Figure 1.4: Schematic energy band diagram of ITO thin films.

Electrical conductivity of ITO thin film is obtained from the equation,

$$\sigma = \mu N e \quad (1.2)$$

where 'μ' is the electron mobility, 'N' is electron density and 'e' is the electron charge. Since electron density and mobility are inversely related as,

$$\mu = 9.816 \times 10^{14} N^{-2/3} \quad (1.3)$$

conductivity cannot be increased after an optimum value (Tahar et al., 1998).

The optical transparency for ITO is limited at short wavelength (UV) of the solar spectrum because of its band gap, photons with energy larger than E_g are absorbed. An effective transparent conducting oxide should have a very low absorption coefficient in the visible region of the solar spectrum. A second transmission edge exists in the NIR region, because of the reflection due to electron plasma (Edwards et al., 2004). With a strong frequency-dependent electron scattering Drude model can describe the relation of optical properties with the charge carriers. For an ITO film having charge carriers $N > 10^{21}$ cm^{-3}, the plasma frequency is given by (Edwards et al. 2001):

$$\omega_p \approx \left(\frac{Ne^2}{\varepsilon_\infty \varepsilon_0 m^*} \right)^{1/2} \quad (1.4)$$

where ε_∞ is the high frequency relative permittivity of the ITO lattice, ε_0 is the permittivity of free space, m^* is the effective mass of the charge carrier and e is the electron charge. This equation shows that in ITO the plasma frequency ω_p is directly proportional to charge carriers. But for a film to be non-reflective to light of wavelength λ_o, it should satisfy

$$\omega_p < 2\pi c / \lambda_o \quad (1.5)$$

Therefore, Equation 1.4 can be written as,

$$N < \frac{4\pi^2 \varepsilon_\infty m^*}{\mu_0 e^2 \lambda_0^2} \quad (1.6)$$

So for ITO, Equation 1.6 can be simplify as,

$$N < \frac{1.6 \times 10^{27}}{\lambda_0^2} \quad (1.7)$$

Therefore, for the efficient transmission of whole visible spectrum up to 780 nm the electron density of ITO in conduction band should not exceed more than

2.6×10^{21} cm^{-3} (Edwards et al., 2004). Increasing the charge carrier density more than this value decreases the transparency of film in the near-infrared region. However, within the limit of maximum charge density, by increasing the mobility of conduction electron, we can increase the conductance of the ITO film. But the mobility of conduction electron limits in ITO due to many reasons, mainly because of the ionized impurity scattering that is produced by excess Sn^{4+} doping and other film condition such as grain scattering, roughness, etc. So acquiring very high optical transmittance in addition to very low resistance needs very accurate optimization of deposition parameters.

1.4.2   Deposition methods of ITO thin films

Transparent and conducting ITO thin films can be prepared by many methods. Sputtering, thermal evaporation, chemical vapour deposition, spray pyrolysis, sol-gel, etc. are most important ITO deposition techniques (Gorgolis and Karamanis, 2016; Jung et al., 2004; Kim et al., 2000; Meng and Santos, 1998). Many studies have been carried out on the preparation of highly conducting transparent ITO thin films by different methods. The results reported in these studies suggest that deposition methods have a huge influence on the quality, electrical and optical properties of ITO thin films. The selection of deposition technique is mainly based on the application of ITO film (Hirschmann et al., 2014). Uniform coating, reproducibility and capability for mass production are also main criteria in the selection of deposition technique.

Sputter deposition is considered as the most suitable method to prepare high quality ITO thin films. Sputtering is commonly used as an industrial ITO film production technique. ITO thin films with excellent uniformity can be prepared in a large area by sputter deposition. Sputter deposition is a physical vapor deposition technique. ITO films are deposited either from a metal alloy (In:Sn) or oxide (In$_2$O$_3$:SnO$_2$) target at vacuum environment. Radio frequency (RF), direct current (DC) and pulsed DC are the main sources of power used in ITO deposition. Simple DC or pulsed DC power supply is appropriate for the ITO deposition from metal alloy target, but complex RF power supply is required for the deposition of film from oxide target. ITO can be prepared by reactive or non-reactive sputtering. Only argon or other non-

8

reactive gas is used in non-reactive sputtering, mostly oxide target is used in non-reactive sputtering. In reactive sputtering, argon (Ar) and oxygen (O_2) gas mixture is used for the deposition. Reactive sputtering is mainly used to deposit ITO thin films from a metal alloy (In:Sn) target. Oxygen reacts with the In and Sn metals ejected from the target and the indium tin oxide is deposited on the substrate. ITO sputtering can be done even at room temperature. Usually, ITO deposited at room temperature are amorphous; for crystalline ITO films high substrate temperature or post-annealing of ITO film is required. But it has been reported that polycrystalline ITO thin films have been sputter deposited on glass and polymer substrates at room temperature also (Kurdesau et al., 2006; Malathy et al., 2009). The advantages of sputtering are: we can systematically control all the deposition parameters to achieve required properties in ITO thin films. The ITO films prepared by sputtering are highly uniform and free from impurities, and also have good mechanical and adhesion properties.

1.4.3   Literature survey on properties of ITO deposited by sputtering method

Electrical conductivity and optical transparency of ITO coatings are two mutually opposite characters. High electrical conductivity in ITO coating can be achieved only by sacrificing the optical transparency of the films. So careful optimization of deposition parameters has to be done for achieving high transparent low resistance ITO coating. The following literature survey consolidates the work done by earlier researchers on sputter deposited ITO coatings.

Mientus and Ellmer (2001) have reported that during reactive sputtering a characteristic minimum partial pressure of oxygen (pO_{2min}) is needed to oxidize the metal atoms arriving at the substrate (Mientus and Ellmer, 2001). Whereas, oxygen partial pressure lesser than pO_{2min} leads to opaque films due to un-oxidized metal clusters and a large amount of oxygen causes complete oxidization of the films, which is highly resistive. Meng and Santos have reported that deposition rate of ITO coating linearly increased with increase in the substrate temperature, and the films prepared at higher temperature were thicker than those prepared at lower substrate temperature (Meng and Santos, 1998). The ITO films prepared at lower substrate temperature showed amorphous structure while increasing the substrate temperature they exhibited

crystalline structure. Jung et al. have reported that at low sputtering power, ITO coatings show poor crystallinity and low electrical resistivity, but they also reported that at higher power densities (than a critical point) the properties of ITO thin films became unfavorable (Jung et al., 2004). Chen et al. studied the influence of oxygen flow on ITO thin films during the sputter deposition (Chen et al., 2014). They reported that the optical absorbance of ITO film decreases with an increase in the oxygen flow rate. Lee and Park have reported that ITO film thickness affects the structure and morphology of the film (Lee and Park, 2006). They reported that ITO films having a thickness less than a critical value were amorphous and thicker films were more crystalline and the film morphology also became clear. Chang et al. have reported a direct method to study the fracture toughness of ITO thin films deposited on flexible substrates from the load-depth curve of nanoindetation (Chang et al., 2013). Their results showed that the fracture toughness of ITO thin films decreased by 6.8% as the substrate temperature increased from 25 to 75°C. Similarly, Sun et al. have reported the effect of heat treatment on the infrared emissivity of ITO film (Sun et al., 2011). They reported that the emittance of the ITO thin film changed with the heat treatment (room temperature to 350°C) because of the improved crystallinity (Ahn et al., 2014).

Many works have been done to understand the electrical and optical properties of ITO. Edwards et al. have reviewed the electronic structure of transparent conducting oxides (Edwards et al., 2004). Tahar et al. have studied the electrical properties of ITO. They noticed that the electrical properties of ITO thin films depend on the preparation method and deposition parameters used for a given deposition technique, and the subsequent heat treatment in various ambiances at different temperatures (Tahar et al., 1998). Granqvist and Hultåker have presented a survey on the progress of fundamental electronic band structure, techniques to boost the conductivity and alternative dopants and manufacturing techniques of ITO thin films (Granqvist and Hultåker, 2002).

Many researchers have studied the properties of ITO thin film deposited on different flexible substrates. Ahn et al. studied the characteristics of ITO resistive touch films deposited on PET substrate using an in-line DC magnetron sputtering (Ahn et al., 2014). They sputter deposited ITO at room temperature on a PET substrate and studied the effect of process parameters such as oxygen concentration ratio and working pressure on electrical properties of ITO thin film. They found that while increasing the

oxygen ratio from 1.6% to 3.4%, minimum resistivity and maximum mobility were achieved at 3.0% oxygen concentration. Eshaghi and Graeli studied the optical and electrical properties of ITO nanostructured thin films deposited on polycarbonate substrates (Eshaghi and Graeli, 2014). They found that a maximum transmittance was achieved at 200 nm ITO thickness, and maximum conductance was achieved at 400 nm thickness. Muneshwar et al. studied the electrical and optical properties of ITO thin film deposited on flexible Kapton® substrate at near room temperature using RF magnetron sputtering system (Muneshwar et al., 2010). They could develop crystalline ITO thin film on Kapton® substrate with maximum transmittance ~82% and minimum resistivity 8.2 x 10^{-4} Ω.cm.

Sierros et al. studied the dry and wet sliding wear of ITO coated on PET substrate (Sierros et al., 2009). They reported an abrupt increase in the sheet resistance of the ITO film for both wet and dry sliding wear conditions. Tran et al. have studied the effect of cyclic deformation on sheet resistance of ITO thin film deposited on PET substrate (Tran et al., 2015). They found that the fatigue life of ITO/PET sheet is increased with an increase in annealing temperature under a small fatigue loading. Yan et al. reported the effect of polyethylenimine (PEI) cathode interlayer on work function and interface resistance of ITO electrode in the inverted polymer solar cells (Yan et al., 2015). They concluded that PEI interlayer can be applied to lower the work function of ITO substrates.

1.5   ITO/metal/ITO hybrid structure

Apart from single thick ITO films, hybrid structures of ITO and the metal thin film also used as the transparent conductors in many applications to improve the mechanical and electrical properties of transparent electrode and also to reduce the ITO film thickness (Hecht et al., 2011; Subrahmanyam and Barik, 2006; Zudans et al., 2004). Many researchers have reported ITO-metal-ITO (IMI) multilayer as an effective alternative for single ITO electrode (Boscarino et al., 2014; Cattin et al., 2010; Guillén and Herrero, 2011; Lee et al., 2016; Lin et al., 2017). The middle ductile metal layer can improve the flexibility of ITO film. Moreover, very low sheet resistance (<10 Ω/sq.) can be achieved for IMI coating deposited even at room temperature with an almost same transmittance of ITO film (Y.-S. Park et al., 2009). Ag, Au, Cu, Al, etc.

11

are used as the intermediate metallic layers by different researchers (Girtan, 2012; Guillén and Herrero, 2008). However, Ag is found to be the best candidate for this application due to its lowest absorption coefficient and lowest refractive index (n ~ 0.05-i2.90) in the visible region of the solar spectrum (K. Hong et al., 2011).

1.5.1 Electrical and optical properties of ITO/Ag/ITO (IAI) multilayer

The sheet resistance of IAI multilayer mainly depends on the sheet resistance of middle metal layer when it is beyond the critical thickness needed for a continuous film (Bender et al., 1998; Indluru and Alford, 2009; Jeong and Kim, 2009). If each layer in IAI structure is considered as a parallel connection of three different resistances (see Figure 1.5), the total sheet resistance (R_s) of IAI structure can be calculated from the equation (Jeong and Kim, 2009);

$$\frac{1}{R_s} = \frac{1}{R_{ITO(top)}} + \frac{1}{R_{Ag}} + \frac{1}{R_{ITO(bottom)}} \qquad (1.8)$$

Where R_s is the total sheet resistance of IAI multilayer, $R_{ITO(top)}$ and $R_{ITO(bootom)}$ are the sheet resistance of top and bottom ITO layers respectively, and R_{Ag} is the sheet resistance of middle Ag layer.
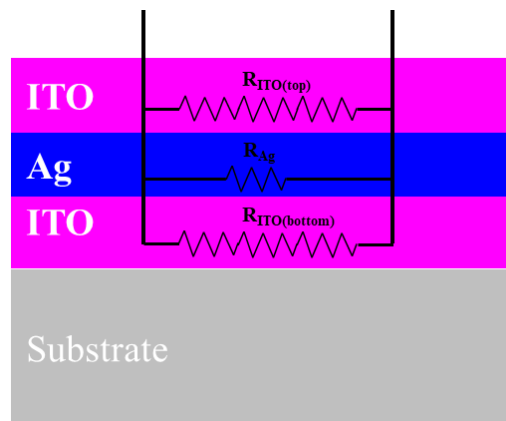
Figure 1.5 Schematic representation of equivalent electrical circuit of ITO/Ag/ITO multilayer (Bou et al., 2016).

12

Generally, the sheet resistance of a continuous metal film is much lower than that of the ITO layers. Therefore, according to equation 1.8, the overall sheet resistance of IAI multilayer will be approximately equal to the low sheet resistance of middle Ag layer.

Optical properties of IAI multilayer depend on the thicknesses of Ag and ITO layers. A metal film can also be transparent in the visible region if it has a refractive index near to zero, because the reflection coefficient of light from the substrate and air interfaces of the metal film are in the opposite phase so there will be a destructive interference (Kostlin and Frank, 1982). Therefore, the only loss of incident beam is due to the absorption of the metal film. But, the absorption of photon energy at a wavelength λ is proportional to $nk_0 d/\lambda$, where n, d and k_0 are the refractive index, thickness and the extinction coefficient of metal film, respectively; so the absorption can be reduced by reducing the thickness of the metal film (K. Hong et al., 2011). Ag is considered as the best candidate for this application due to its lowest refractive index in the visible region of solar spectrum ($n_{Ag} = 0.05 - i3.09$) (Lee et al., 1996). The optical transmittance of Ag layer can be further enhance by sandwiching it between two dielectric layer like ITO with high refractive index ($n_{ITO} \sim 2$) and low absorption in visible region of the solar spectrum (Kostlin and Frank, 1982). The antireflection effect of these multilayer stack results in high transmittance in the visible region. Optimum thicknesses of Ag and ITO in IAI multilayers can be found out using the admittance diagram technique. Figure 1.6 (a)-(c) shows the admittance diagram of ITO, Ag and IAI multilayers films. Figure 1.6 (a) shows the admittance plot of a single ITO thin film (refractive index is represented as n_{ITO}) deposited on substrate of refractive index n_s. Admittance starts from the substrate (n_s,0). As the ITO optical thickness increases, the admittance increases and at quarter wave thickness the admittance re-enters the real axis, that point has the highest reflection (low transmittance) due to constrictive interference of partial reflected waves from air and substrate interfaces (K. Hong et al., 2011). Further increasing the ITO layer thickness, the admittance will trace out a full circle for next quarter-wave and re-enter the (n_s,0) point which has the lowest reflection (high transmittance) due to the destructive interference of reflected rays. Increasing the ITO layer thickness even further results in the rotation of admittance on the same circle. The admittance of Ag layer is somewhat distorted from ideal circle, because Ag has an

imaginary part of the refractive index. The antireflection effect can attain when the admittance starts from admittance of substrate (ns,0) and ends at admittance of air (1,0), as shown in Figure 1.6 (c) (Kostlin and Frank, 1982; Zilberberg and Riedl, 2016).
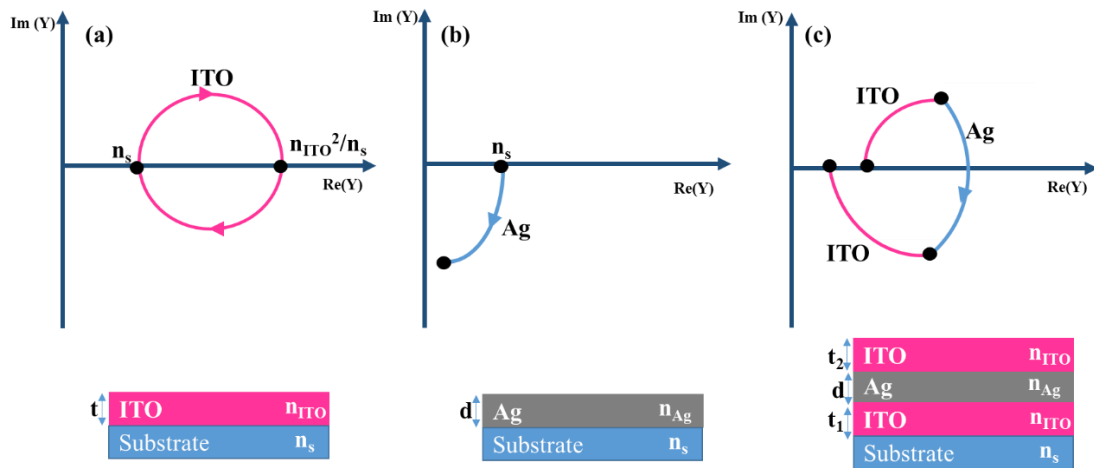
Figure 1.6: Admittance plots of (a) and (b) single ITO and Ag layers, and (c) IAI multilayers deposited on top of a substrate. n_s, n_{ITO} and n_{Ag} are refractive indices of substrate, ITO and Ag, respectively (Zilberberg and Riedl, 2016).

1.5.2 Literature survey on electrical and optical properties of ITO/Ag/ITO multilayers

Many works have been done to understand the electrical and optical properties of IAI multilayer. Hong et al. have reported that inserting a thin Ag (5-20 nm) layer between ITO resulted in significant decrease in sheet resistance from 66.1 to 7Ω/square (C. H. Hong et al., 2011). Jeong and Kim investigated the properties of IAI multilayer deposited by linear facing target sputtering on a glass substrate (Jeong and Kim, 2009). They found that optimization of middle Ag layer thickness is very important to get good optical and electrical properties because the surface plasmon resonance and antireflection effect critically depend on the Ag morphology. They reported that IAI multilayer with 16 nm Ag layer thickness showed lowest sheet resistance of 4.4 Ω/square with optical transmittance of 86.03% in the 400-550 nm wavelength range. Indluru and Alford reported that 8 nm is the critical thickness of Ag film to form a continuous film. Less than 8 nm Ag thin film formed island-like growth, which decreased the sheet resistance of IAI multilayer (Indluru and Alford, 2009). Kim et al.

14

studied the electrical and optical properties of IAI multilayer as a function of ITO layer thickness (Kim et al., 2007). They found that transmission window of IAI multilayer widened and red shifted with increasing ITO layer thickness.

Guillen and Herrero investigated the electrical and optical properties of IAI multilayer sputtered on soda lime glass at room temperature (Guillén and Herrero, 2009). They reported the sheet resistance of 6 Ω/square and transmittance above 90% for IAI multilayer with overall ITO layer thickness less than 100 nm. They also reported that the position of transmittance maximum can be tuned by varying the ITO layer thickness so that better spectral selection is possible in IAI multilayer for the specific application. In another work, Guillen and Herrero reported the thermal stability of IAI multilayer (Guillén and Herrero, 2008). They found that IAI multilayer deposited on a glass substrate is stable even at 350°C. Cheng et al investigated the durability of IAI multilayer against moisture (Chen et al., 2007). Their study showed that top ITO layer with good wettability intended to resist the moisture-induced degradation of IAI electrode. They also proposed that Ti-doped intermediate silver layer (ITO-Ag(Ti)-ITO) exhibited excellent resistance against moisture.

Many researchers have studied properties of IAI multilayer deposited on different flexible substrates. Kim et al deposited IAI multilayer thin films on polyethylene terephthalate (PET) substrate by sputtering at room temperature (Kim et al., 2010). They reported that sheet resistance of IAI multilayer was superior to those of ITO films that were deposited at a higher temperature. Their optimized IAI multilayer on PET substrate showed sheet resistance less than 6.7 Ω/square and transmittance 83.2% at 550 nm. Kim et al. reported roll-to-roll sputter deposition of IAI multilayer on PET substrate (Kim et al., 2017). They achieved a sheet resistance of 8.93 Ω/square and optical transmittance 82.4% for IAI multilayer on PET substrate. Park et al. reported properties of roll-to-roll sputtered IAI multilayer on flexible polyethersulfone (PES) substrate at room temperature (Y.-S. Park et al., 2009). Optimized IAI multilayer deposited on PES substrate showed sheet resistance of 4.28 Ω/square and optical transmittance of 89.28%. They also demonstrated the superior flexibility of IAI multilayer over to the single ITO electrode.

1.6   Applications of ITO and ITO/Ag/ITO multilayer films for space, solar and flexible electronics.

1.6.1   ITO thin films on flexible substrates for space application

Thin films of ITO are used in thermal control system of spacecraft applications (Reddy et al., 2013). Thermal control system in spacecraft has very crucial role to protect the inner components of spacecraft from the temperature gradients in space (Goldstein et al., 1982; Ichino et al., 1986; Miyazaki and Yamagata, 2009; Teissier et al., 2012). For better performance and reliability of the electronics and other components inside the satellites a steady temperature environment has to be maintained (Teissier et al., 2012). However, in space due to the lack of any medium around the satellite other than radiation there are no other conventional heat transfer methods possible to transfer heat from inside of the satellite to the outer space. Therefore, passive thermal control elements such as Kapton® based multilayer insulation (MLI) blanket, and fluorinated ethylene propylene (FEP) based flexible optical solar reflectors, etc. are used to control the outer and inner temperature of spacecraft. Rear side Ag-coated FEP substrate shows the lowest α/ε value (where "α" is absorptance and "ε" is emittance), therefore, the equilibrium temperature will be low on the surface (Chang et al., 2014; Ichino et al., 1986; Pipptin et al., 2001). On the other hand, highly reflective rear surface aluminized Kapton® is often used in MLI (implemented for thermal insulation purpose) as outer surface (i.e., space facing surface). It is well known that space environment frequently alters depending on altitude and sun seasons (Gilmore, 2002). The major space environment variables are temperature, low dense atoms, and molecules, electron clouds with different energies, charged particles, plasmas, atomic oxygen, etc. In particular, for communication satellites in geostationary orbit, the presence of energetic electrons is a major concern (Sharma and Sridhara, 2012). Aforesaid thermal insulation materials based on FEP and Kapton® are able to withstand most of the space environment but not for electrostatic charges because of their insulating surface nature. This electrostatic charge (i.e., ~20-30 kV) can cause serious damage to the satellite if it is not properly drained away (Goldstein et al., 1982; Miyazaki and Yamagata, 2009; Schmidt, 1980). To bleed off the accumulated static electric charges the moderate sheet resistance surface is preferred (Gilmore, 2002; Goldstein et al., 1982; Miyazaki and

Yamagata, 2009; Schmidt, 1980). Indium tin oxide film (ITO) is often utilized on FEP and Kapton® to bleed off electrostatic charges for space application. Apart from electrical conductivity, the ITO thin film also shows highly transparent behavior in the solar region of the spectrum and thus optical properties of the substrate (with rear surface reflective coating) are not hindered.

1.6.2 ITO/Ag/ITO thin films for solar energy application

The scarcity of conventional energy sources has forced to find out new sources of energy and energy-saving methods. Therefore, in the last few decades, active and passive use of solar power got much attention for the global energy production. It has been reported that hybrid solar power conversion by combining different solar energy conversion methods can be used to improve the efficiency of total solar energy conversion (Mojiri et al., 2013; Soule and Wood, 1986; Soum-Glaude et al., 2012; Uzu et al., 2015). Hybrid photovoltaic (PV)-thermoelectric generator (TEG) system is one of the established technology used to increase the efficiency of total solar energy conversion (Chendo et al., 1987; Chow, 2010; Herrando and Markides, 2016; Osborn et al., 1986). Many works have been carried out in this field to improve the efficiency and finding the new areas of applications (Jradi et al., 2011; Vorobiev et al., 2006; Wang et al., 2011; Yang and Yin, 2011). It has been reported that majority of the photovoltaic solar cells' spectrum response is most efficient when the energy of a photon is near to solar cell band-gap energy, the remaining lower and higher wavelength regions of the solar spectrum are only partially utilized. So, by spectrum splitting and directing the solar radiation not in the range of given solar cell's band gap to the thermoelectric generator (TEG) for producing electricity by thermoelectric effect will increase the efficiency of total solar conversion. Moreover, it can reduce the heat from the solar cell (Ju et al., 2012). Ju et al. have found that the optimum generated power of the PV/TEG hybrid system is achieved when the spectrum splitter has a cutoff wavelength (λ_c) around 900 nm (Ju et al., 2012). Figure 1.7 shows the total solar spectrum and the useful potions for solar cells and thermoelectric generator.
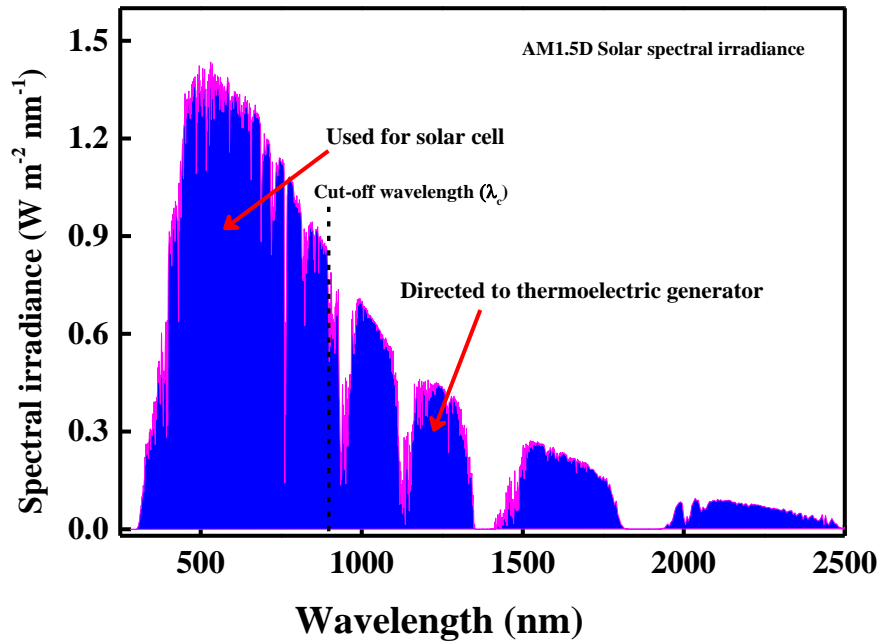
Figure 1.7: Segmentation of total solar spectrum irradiance for solar cells (left of the cutoff wavelength) and thermoelectric generator (right of cutoff wavelength) (Ju et al., 2012).

Different types of solar spectrum splitting methods for hybrid PV/TEG system have been suggested over the years (Imenes and Mills, 2006). They include: solar beam splitting transparent heat mirrors, holographic concentrators, liquid absorption, rugate filters, etc. (Imenes and Mills, 2006; Mojiri et al., 2013). The solar beam splitting transparent heat mirrors are investigated for many years (Lampert, 1981; Pracchia and Simon, 1981; Shou et al., 2012; Soule and Wood, 1986; Yuste et al., 2011). Transparent heat mirrors (THM) use a thin coating on a substrate of glass which can transmit the visible region and reflect the near-infrared (NIR) and infrared (IR) region of the solar spectrum (Fan and Bachner, 1976). An ideal THM should possess maximum transmittance in the visible region and maximum reflectance in NIR and IR regions (Lampert, 1981). Because of the unique properties of THMs, they can be used for various applications such as solar flat-plate collectors for solar heating and cooling, solar hybrid systems, energy efficient windows, thermal insulators for many structures, etc. (Al-Kuhaili et al., 2009; Granqvist, 1981). However, to achieve high visible

transmittance (T_{vis}) and high NIR and IR reflectance together is a difficult task. Many previous works have been carried to achieve the maximum transmittance in the visible region and maximum reflectance in the NIR and IR wavelength regions (Al-Kuhaili et al., 2012; Dalapati et al., 2016; Pracchia and Simon, 1981).

It has been reported that transparent and conducting film can be used for THM application due to its wide band gap and high charge density which gives high reflection in NIR and IR regions (Arfsten, 1984; Granqvist, 1981; Griffiths et al., 1992). Among these materials, tin-doped indium oxide (ITO) is considered as a premium one because of its high transmittance in the visible region and high reflectance in the NIR and IR regions due to its high charge carrier density. Moreover, by adjusting the preparation parameters such as thickness, oxygen content, etc., we can enhance the transmittance in a particular wavelength range (Guillén and Herrero, 2009). However, to further enhance the spectral selectivity, multilayer structures of ITO and a high reflecting metal layers are used (Kusano et al., 1986). A thin layer of Ag, Au, Cu, etc. was sandwiched between two thin ITO layers, and this type of multilayer system gives better selectivity than a single layer ITO (Lampert, 1981; Pracchia and Simon, 1981). In addition, the visible transmittance, NIR and IR reflectance and the λ_c of the solar spectrum can be adjusted by varying the thicknesses of ITO and metal layers. For the middle metal films, Ag is considered as a suitable candidate for the multilayer THM application, because of its high reflectance in NIR and IR regions and lowest refractive index and lowest absorption in the visible region of the solar spectrum (Durrani et al., 2004; Lee et al., 1996). Many researchers have investigated ITO/Ag/ITO (IAI) multilayer systems for solar spectrum splitting and transparent electrode applications (Choi et al., 1999; Granqvist, 2007; Jeong and Kim, 2009; Kusano et al., 1986).

1.6.3 ITO/Ag/ITO thin films for flexible electronics application

Transparent conductor is one of the key materials for high performing devices in energy (smart windows, transparent heat mirror, solar cells, etc.), information (display, OLED, etc.), and automobile sectors (Ellmer, 2012). Recent research is being directed towards flexible solar cells, OLEDs, displays, wearable electronics, etc. (Kim et al., 2017; Park et al., 2016; Y.-S. Park et al., 2009). The lightweight, low cost, easy

for storing and transport make flexible devices more adapted to day to day life. Even though ITO is one of the most successful transparent conducting materials and widely used in commercially available devices, due to the brittle nature of ITO film it has a limitation in many high performing flexible electronic devices (Biswas et al., 2015; Kumar et al., 2015). Cracks can develop during the bending of ITO electrode, which increase the electrical resistance and hence the performance of the device comes down (Kim et al., 2017; Y.-S. Park et al., 2009). Moreover, low sheet resistant ITO film requires high processing temperature (>300°C), which is not favourable for many plastic substrates with low melting temperature (Guillén and Herrero, 2008). Extensive work has been carried out on silver, carbon and metal network based flexible transparent electrodes. However the problems of processing temperature, uniform sheet resistance, high transmittance and mass production are yet to be resolved. Many researchers have reported flexible ITO-Ag-ITO (IAI) multilayer as an effective alternative for single ITO electrode. The middle ductile metal layer can improve the flexibility of ITO film. Moreover, very low sheet resistance (<10 Ω/sq.) can be achieved for IAI coating deposited even at room temperature with an almost same transmittance of ITO film (Y.-S. Park et al., 2009). IAI multilayer has been used as a transparent electrode in many flexible electronic applications such as solar cells, displays, OLEDs, electrochromic devices, etc. (Girtan, 2012; Guillén and Herrero, 2008; Kim et al., 2016, 2017; Lewis et al., 2004; Park et al., 2016). Kim et al (2017) used IAI multilayer deposited flexible PET substrate for the electrochromic application (Kim et al., 2017). They found that electrochromic P3HT film deposited on IAI/PET substrate exhibited excellent electrochromic performance with a high coloration efficiency, fast response speed compared to the P3HT film deposited on ITO/glass substrates. Kim et al. reported that IAI multilayer deposited PET substrate is a good electrode for the large-scale flexible OLED devices (Kim et al., 2010). Park et al. reported that organic solar cells fabricated on IAI deposited PES substrate showed a similar efficiency of 3.73% to the organic solar cell fabricated on commercially available high-quality ITO electrode (Y.-S. Park et al., 2009). Moreover, the solar cell fabricated on IAI multilayer was more flexible than that fabricated on ITO electrode.

1.7 Scope of the work

Aforesaid discussion undoubtedly proves that ITO and ITO/Ag/ITO multilayer thin films are potential candidature in state-of-the-art application domains, e.g., solar cell for energy harvesting application, optical solar reflector for spacecraft, and electrode for optoelectronic. However, it is also an important concern to note that in spite of their emerging and multifaceted applications possibility, the reports on the optical and electrical behaviour of ITO coatings on many substrates like FEP, Kapton® and aluminized Kapton® which are frequently used in solar and space applications, are scarce in the literature. Therefore, a detailed study of optical and electrical properties of ITO thin films deposited on different flexible substrates will be helpful for the space application as well as futuristic flexible electronic applications. The stability of ITO coating on flexible substrates is also an important matter to be considered. Hence, it is important to examine the stability of ITO coated FEP and Kapton® substrates in different environmental conditions.

It is clear from the literature that ITO/Ag/ITO multilayer is a good alternative for thick ITO film. The usage of ITO material can be reduced by using thin IAI multilayer. High optical transmittance and low sheet resistance similar to thick ITO film are achieved in IAI multilayers with an overall thickness less than 150 nm. One of the important characteristics of IAI multilayer is the ability to tune the solar spectrum selectivity of IAI multilayer by varying ITO and Ag layers thicknesses. In solar energy harvesting application, spectrum selectivity of TCs is an important factor to achieve high efficiency of the devices. Solar photovoltaic cells usually absorb only in the visible region of the solar spectrum, remaining lower and higher wavelength of the solar spectrum is not used for the photovoltaic conversion, and moreover, these lower and higher wavelength rays will increase the temperature of photovoltaic cells that is not good for the solar cells. So, splitting the solar spectrum not only reduces the heating problem of solar cells but also can be used in another type of solar energy conversion such as thermoelectric generator, where heat energy is used to produce the electricity. So, IAI multilayer with tuneable solar selectivity, i.e., high transmittance in the visible region and high reflection in NIR and IR regions of the solar spectrum is a good choice for hybrid solar energy conversion. Many researchers have tried to increase the optical transmittance and NIR reflection by adjusting the film thicknesses of the multilayers.

But none of the researchers reported the combination of the antireflection effect of the glass substrate and IAI multilayer to increase the figure of merit of IAI/glass spectral beam splitter. The optical transmittance of soda lime glass can be increased by a simple hydrofluoric acid vapour etching. Etching is so selective that it can be done only on single side of the glass substrate. Optimized etched substrates show good broadband antireflection of the solar spectrum. Therefore, the study of the optical properties of IAI multilayer deposited on one side etched glass substrate is really necessary to improve the efficiency of IAI multilayer solar segregator.

Due to poor mechanical properties of ITO it is restricted for some of the applications, in particular, for flexible optoelectronic device applications such as display panels, light emitting diodes, solar cells, etc., where choice of ITO is limited because of tendency of cracking due to bending or stretching, which ultimately can lead to deterioration of its mechanical integrity and electrical properties as well. Therefore, it is clear from the literature that highly transparent and conducting flexible IAI multilayer will be the best choice in place of single thick ITO layer. Researchers have found that optoelectronic devices fabricated on IAI multilayer show good mechanical, electrical and optical properties. IAI multilayers are deposited on different flexible substrates. However, in literature, study of properties of IAI electrode deposited on many important flexible substrates are missing. There is no reported data of IAI multilayer deposited on flexible FEP and Kapton® substrates. FEP substrate shows very high solar transmittance and good solar durability. Therefore, the study of highly transparent and conducting IAI multilayer on this substrate will be very much useful for the rapidly growing flexible transparent electrode applications. Similarly, Kapton® is another important substrate for flexible devices which can be used in high temperature applications. Thus, the study of IAI multilayer on Kapton® substrate also will be very much useful.

1.8   Objectives of the work

After thorough literature survey and looking at the scope of work on ITO and IAl multilayer films, the following objectives have been finalized for the proposed research work.

- Reactive sputter deposition of transparent and conducting ITO thin film on flexible FEP, Kapton® and aluminized Kapton® substrates.
- Study of electrical and optical properties of ITO coating on different substrates.
- Detailed study of space environmental stability of ITO coated FEP and Kapton® substrates in simulated space environments.
- Fabrication of hybrid ITO/Ag/ITO multilayer structure on different substrates (glass, and flexible FEP and Kapton®).
- Solar selectivity study of IAI multilayer deposited on plain and one side etched glass substrate.
- Study the optical, electrical and mechanical (flexible) properties of IAI multilayer deposited on rigid glass and flexible FEP and Kapton® substrates.

1.9. Outline of the thesis

The present thesis comprises of 7 Chapters and each Chapters are summarized concisely below.

Chapter 1: This Chapter gives introduction to transparent conductors and their importance in the field of harnessing solar energy, space and flexible electronics. An overview of literature survey on transparent and conducting ITO and ITO/Ag/ITO multilayer films are also discussed in this Chapter. This Chapter concludes with the scope and objective.

Chapter 2: Chapter 2 describes the detailed experimental methods used for the deposition of ITO and ITO/A/ITO multilayers on rigid and flexible substrates. Characterization technique used to analyze the optical, structural and electrical properties of the ITO and ITO/Ag/ITO have also been discussed in this Chapter.

Chapter 3: In this Chapter optimization of deposition parameters and characterization of ITO thin films on flexible fluorinated ethylene propylene (FEP) substrate for spacecraft applications is discussed.

Chapter 4: Stability of ITO coatings on different flexible substrates such as FEP, Kapton® and aluminized Kapton® substrates in simulated space environmental is discussed in this Chapter.

Chapter 5: This Chapter describes the deposition of a spectral beam splitter (i.e., ITO/Ag/ITO) which exhibits high transmittance and high reflectance in the visible and NIR/IR regions, respectively, is reported. In addition, the effects of ITO and Ag layer thicknesses on the visible transmittance, NIR/IR reflectance and also on the cut-off wavelength have been studied in detail.
.

Chapter 6: The optimization of ITO/Ag/ITO multilayers for the transparent conductor application is described in this Chapter. Estimation of the optimum ITO and Ag layer thicknesses is obtained through the calculation of the figure of merit deduced from the transmittance and the sheet resistance of the IAI multilayers.

Chapter 7: This Chapter dedicates the overall summary of the results with justification described in the previous Chapters. Moreover, this Chapter includes few propositions for the future work.

CHAPTER 2

EXPERIMENTAL DETAILS

Deposition technique of ITO and ITO/Ag/ITO multilayer thin films, substrate preparation, chemical and plasma etching of substrates, and characterization techniques used to characterize these thin films are described in this Chapter.

2.1   Reactive magnetron sputter deposition

ITO and Ag thin films were deposited on rigid and flexible substrates using an indigenously developed balanced magnetron sputtering system. Figure 2.1 shows the photograph and schematic representation of magnetron sputter system used in this work. The sputtering system consists of a cylindrical vacuum chamber, sputter guns, vacuum pumps, vacuum gauges, power supplies, mass flow controllers, etc. Vacuum chamber has the provision of four water-cooled sputter guns to prepare multilayer coatings without breaking the vacuum. However, only two of them were used to deposit ITO and Ag thin films. The sputter guns consists planar circular magnetrons with target diameter 0.076 m. They were mounted vertically downwards inside the chamber. The substrate holder was placed at the bottom of the vacuum chamber on a manually movable circular plat and the distance between the substrate to target was 5 cm. The substrate could be moved under the respective targets to deposit multilayers. The substrate holder consists of an inbuilt substrate heater made up of a quartz bulb and it is connected to a chromel-alumel thermocouple and a solid-state relay driven feedback circuit to measure and control the temperature. High vacuum is created in the chamber using a turbo molecular pump backed by a rotary pump. Rotary pump with 165 lit/sec pumping capacity is used to bring down the pressure from atmospheric to 10^{-3} mbar. Thereafter, a water-cooled turbo molecular pump with a maximum rotational speed of 27000 rpm and pumping speed 400 lit/sec capacity along with rotary pump was used to create a base pressure of below 7.0 x 10^{-6} mbar. A Pirani gauge was used to measure the rough vacuum, and a Penning gauge was used to measure the high vacuum inside

the chamber. Mass flow controllers (MKS) were used to control the flow rate of the sputtering gases.
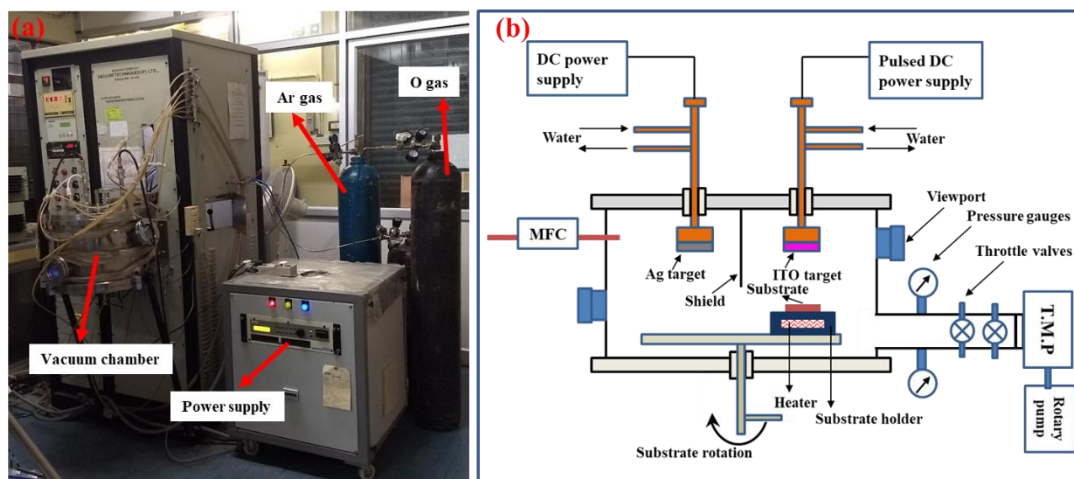
Figure 2.1 (a) Photograph of magnetron sputtering system used in this work. (b) Schematic diagram of the sputtering setup.

2.1.1 ITO deposition

ITO thin film were deposited using a 99.99% pure In:Sn (90%:10% wt.) alloy target of diameter of 0.076 m and thickness of 6 mm. The sputtering gases used in the experiments were argon and oxygen. The flow rates of oxygen and argon were controlled separately by mass flow controllers. Prior to all deposition, the target was cleaned under argon plasma for 1 min. All the ITO depositions were done using pulsed DC power supply (ENI, RPG-50) with frequency of 100 kHz and pulse width of 2976 ns. Substrate temperature was varied from room temperature to 140°C.

2.1.2 ITO/Ag/ITO multilayer deposition

ITO/Ag/ITO multilayer coatings were deposited by a DC balanced magnetron sputtering system without breaking vacuum of the chamber. Bottom and top ITO layers were deposited as described in previous section. Ag layers were deposited using a 99.99% pure Ag target of diameter 0.076 m and thickness 6 mm. All the Ag layer was deposited using a DC power supply at 5 W power. Only argon gas was used for the Ag deposition. Before each Ag layer deposition, target cleaning was carried out for 30 sec.

After depositing bottom ITO layer, the substrate was moved under the Ag target and the middle Ag layer was deposited. Thereafter substrate was moved to under the ITO target for the deposition of top ITO layer. All the ITO and Ag layers were deposited at room temperature for multilayer film.

2.2   Substrate preparation

Fluorinated ethylene propylene (FEP), Kapton®, aluminized Kapton®, borosilicate glass and Si were used as the substrates for ITO and ITO/Ag/ITO multilayer sputter deposition. Dupont^{TM} Teflon® FEP (Type A, ~125 µm thickness), plain Kapton® and aluminized Kapton® (thickness ~50 µm) of size 45 mm X 45 mm were also used as the substrates. Borosilicate glass (from Borosil) of dimension: 17 mm × 25 mm × 1.25 mm were used as the substrates. For holding the flexible substrates a substrate holder was made with a circular copper back plate and an aluminium cover plate. The flexible substrates were fixed between the copper plate and aluminium cover plate. Cover plate has a 40 mm x 40 mm rectangular opening to expose the substrate to the plasma. For keeping the substrate steady between back plate and cover plate, they were clamped with four screws in four sides. Some coatings were also deposited on ~10 mm X 10 mm size silicon substrates for characterization.

FEP and plain Kapton® substrates were ultrasonically cleaned in isopropyl alcohol for 2 min and dried with high purity nitrogen flush before placing into the vacuum chamber. The aluminized Kapton® substrates were not cleaned in any chemicals and they were loaded into the vacuum chamber as it is after nitrogen flushing. ITO was deposited on the opposite side of aluminium coated side of Kapton® substrate. The glass and Si substrates were cleaned by ultrasonication in isopropyl alcohol and acetone for 10 min each.

2.3   Plasma etching

Surface treatment of FEP substrate was carried out using a Plasma Matrix (BDISCOM) instrument in argon atmosphere. Figure 2.2 shows the photograph of etching instrument and a schematic representation of FEP plasma etching process. A stainless steel substrate holder was used to hold the FEP substrates for the plasma etching. After placing the substrate inside the plasma etching chamber, the chamber

was evacuated down to a base pressure 5.0 Pa using a rotary pump. After reaching the base pressure, 26% argon gas was passed in to the chamber using a mass flow controller. A stabilizing time of 60 sec was kept before starting the etching process. 100 watt RF power was used for the etching and the etching was done at room temperature. The duration of etching was varied from 2 - 12 min. Etched samples were immediately loaded into the vacuum chamber.
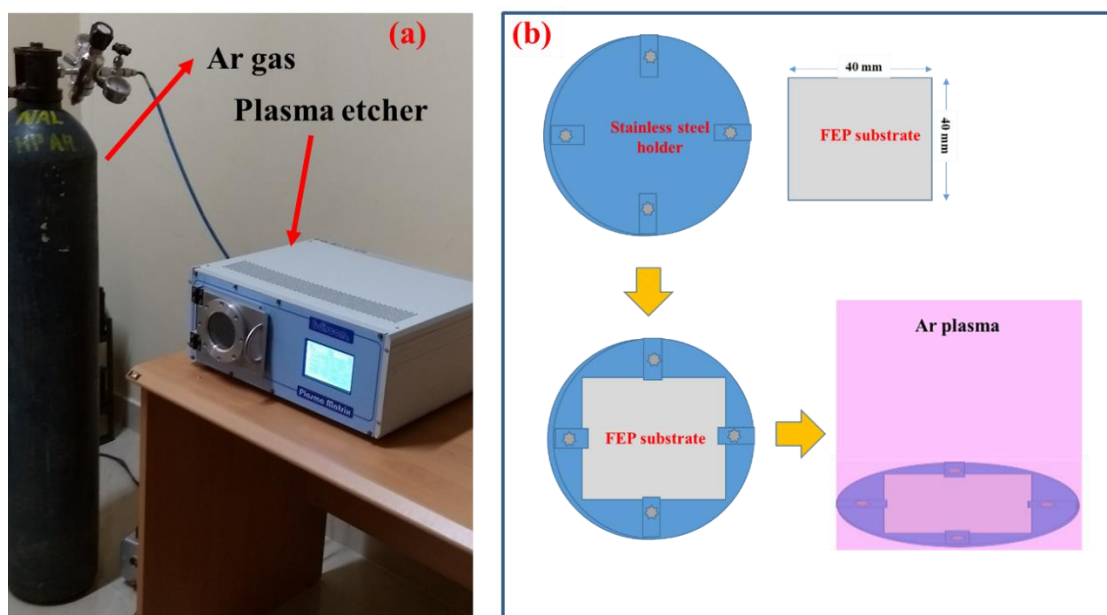
Figure 2.2: (a) Photograph of plasma etching setup and (b) schematic representation of FEP plasma etching process.

2.4   Chemical etching

Some glass substrates were chemically etched to increase the transmittance. Hydrofluoric acid (HF) with 40% concentration (procured from Merck) was used to etch the glass substrate. Figure 2.3 shows the schematic representation of HF vapor phase etching process. Etching was carried out at 50⁰C substrate temperature. Cleaned glass substrates were preheated at 50⁰C using a heater for one minute before the etching. 6 ml of HF was measured in a measuring jar and poured in to the Teflon container. Heated glass substrate along with sample holder and heater kept were on the HF container. Etching of the glass substrate was performed for 1 minute. The etching was done only on one side of the glass substrate. After etching, the glass substrate was removed from the holder and annealed at 350⁰C for 30 min in air furnace. Non-etched

side of the glass substrate was cleaned with IPA before loading into the vacuum chamber. The deposition was done on the non-etched side of the glass substrate.
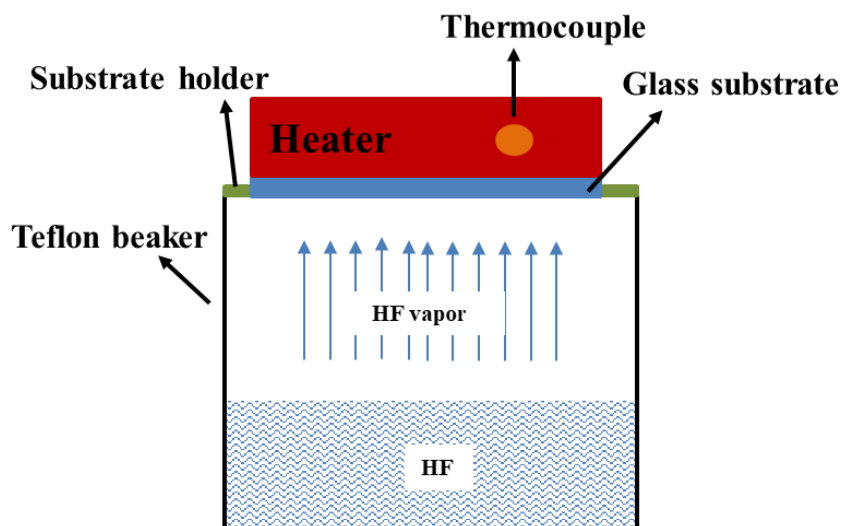
Figure 2.3: Schematic representation of HF vapor etching setup (Kumar et al., 2016).

2.5   Characterization techniques

2.5.1   UV-Vis-NIR spectrophotometer

Solar spectrum transmittance, reflectance and absorbance over the wavelength range from 250 to 2500 nm were measured using a PerkinElmer Lambda 950 UV-Vis-NIR spectrophotometer. Figure 2.4 shows the photograph of UV-Vis-NIR spectrophotometer used in this work. Spectrophotometer consists of light sources, monochromator, beam splitter, sample compartment, reflecting mirrors and detector compartment. A tungsten halogen lamb is used as the NIR and visible radiation source, and a deuterium lamp provides the UV radiation. In the present work, the transmittance and reflectance of the samples were recorded using a 150 mm integrating sphere accessory attached with the spectrophotometer. Integrating sphere is capable to record specular, diffusive and total (specular and diffusive) transmittance and reflectance of the samples with an accuracy of one place after the decimal. Two different types of detectors are used to record the whole transmittance and reflectance spectrum. A photomultiplier module (PMT) detector is used to record UV and visible region of the spectrum, and a PbS detector is used to record NIR region of the spectrum. The changeover of the detector takes place at 860.8 nm. The change of the detector can be

noticed in the recorded spectra as a small perturbation at that wavelength. Except for the angular reflection studies, all other transmittance and reflectance spectra were measured at angle of incidence of 8^0.
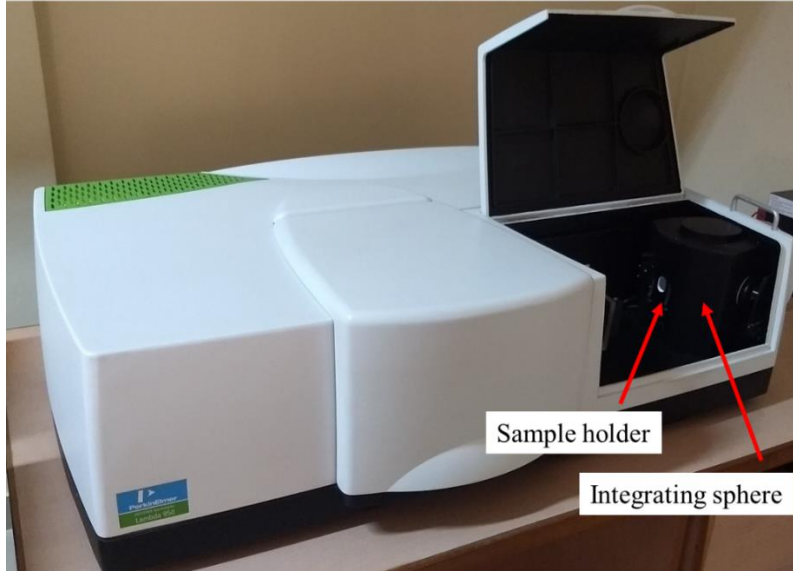
Figure 2.4: Photograph of UV-Vis-NIR spectrophotometer.

Optical haze measurements

Haze factor of transparent conductors are very important to be considered in the figure of merit of TCs. Haze is the forward scattered part of incident light through the film. Haze of the optical coating is defined as (Preston et al., 2013),

$$\text{Haze} = \frac{\text{Forward scattered light}}{\text{Total transmitted light}} \times 100\% \qquad (2.1)$$

In this work, optical Haze of the samples was measured as per the ASTM 1003 standard using an integrated sphere attached with UV-Vis-NIR spectrophotometer (ASTM D1003-00, 2000). Haze was measured as per the following formula,

$$\text{Haze} = \left(\frac{T_4}{T_2} - \frac{T_3}{T_1}\right) \times 100\% \qquad (2.2)$$

where T_1, T_2, T_3 and T_4 are the different configurations of the transmittance scans to obtain scattered and total transmittance spectra (Padera, 2009). Figure 2.5 shows the schematic representation of these configurations in the integrating sphere.

Where T_1 is the total transmitted light measured without any sample, and T_2 is the total transmitted light measured with the sample. During T_3 and T_4 transmittance measurements the reflectance port of integrating sphere was open, so the specular portion of the transmitted light will not reach the detector inside the integrating sphere, only the scattered portion of the transmitted light will be measured in this set up. T_1/T_2 gives the instrumental correction.
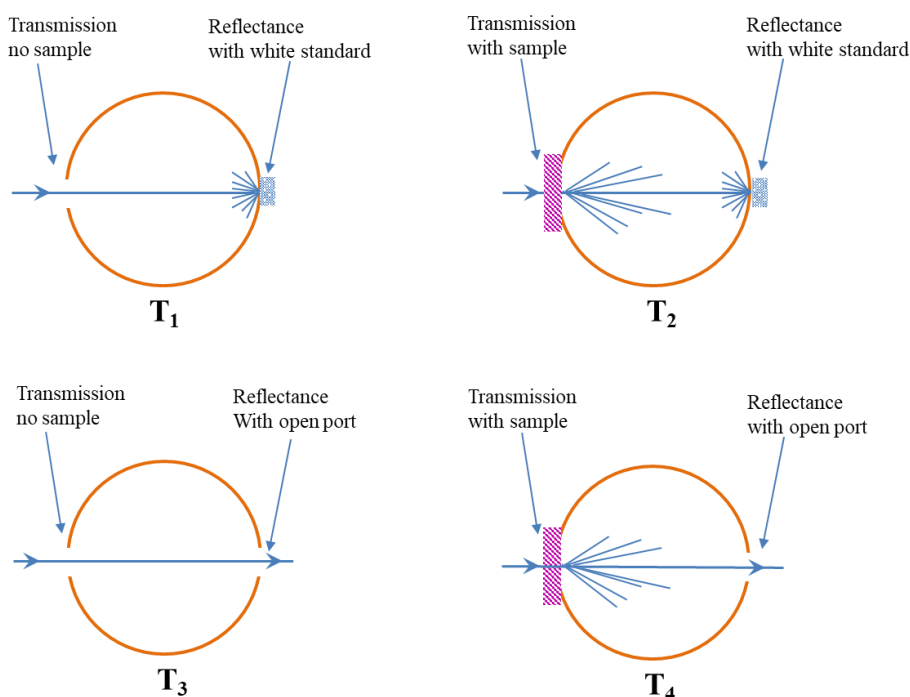
Figure 2.5 Different configurations of transmission spectra for the haze measurements (Padera, 2009).

Angular reflection studies

Angular dependent reflectance studies of the samples were carried out using a universal reflectance accessory (URA) attached to the spectrophotometer. Using URA, reflectance for different angles of incident of light (8 to 68⁰) can be measured in the wavelength regime of 250 to 2500 nm without realigning the accessory or repositioning the sample.

In the present work, the angular dependent absolute reflectance study (8 to 68⁰) was carried out using both p-polarized (transverse magnetic (TM)) and s-polarised

(transverse electric (TE)) components of the light. The light has been split using a prism attached to the spectrophotometer.

2.5.2 Emissometer

The thermal emittance of the ITO coating was measured using an emissometer (Model AE1, M/s Devices and Services). The spectral range of the thermal radiation emitted from the surface at 82ºC is in the range of 3 to 30 µm. The emissometer was heated to 82ºC, therefore the sample to be measured need not be heated. The emissometer was calibrated using standard samples of high and low emittance values of 0.88 and 0.05, respectively. The emissometer has accuracy of $\pm$ 0.01 units (Barshilia et al., 2008).

2.5.3 Fourier transform infrared spectroscopy (FTIR)

Fourier transform infrared spectroscopy (FTIR) used to record the transmittance, reflectance and absorption of samples in mid-IR and IR regions of the solar spectrum. FTIR works on the principle of interferometer that gives an interferogram, a plot of light intensity versus optical path difference (Smith, 2011). An FTIR spectrometer consists of three basic components namely: IR radiation source, interferometer and detector. The IR radiation sources are the inert solids that are heated electrically to stimulate thermal emission of radiation in the infrared region of the electromagnetic spectrum. The radiation from the source reaches the material through the interferometer. Interferometer consists of a beam splitter, and two perpendicular mirrors in which one of them is fixed and other one is movable. Beam splitter equally splits the incoming radiation. The transmitted and reflected parts are directed towards a fixed mirror and a movable mirror, respectively. The reflected rays from the mirrors recombine at the beam splitter. But, movable mirror is displaced to make a path difference between the two rays. Due the path difference in the recombined waves an interferogram is produced. These rays pass through the sample and reach the detector. When the IR beam is passes through the sample, some radiation is absorbed or transmitted or reflected by the sample. By Fourier transform the recorded interferogram of the sample property can be understood.

In this work, the total reflectance of ITO and ITO/Ag/ITO multilayer systems in NIR and IR (2 to 25 µm) regions of the spectrum were measured using a FTIR spectrometer (PerkinElmer Frontier) with an integrating sphere accessory (PIKE Technologies) for an average of 100 scans and 8 cm^{-1} resolution. The photograph of FTIR instrument used in this work is shown in the Figure 2.6. For the reflection studies background was taken using a gold standard as the reference. Total transmittance was measured in transmittance mode using transmittance accessory attached with the instrument.

Figure 2.6: FTIR instrument with integrating sphere accessory.

2.5.4 Sheet resistance measurement by four point probe method

In the present work, the sheet resistance of the samples was measured by four point probe method using a Jandel RM3000 instrument. Four point probe method is a powerful technique to find out the sheet resistance of very thin films and wafers. Four point probe setup consists of four metal tips with finite radius and pointed end. The four probes are equally spaced each other. The pointed edges are placed on the thin film. The outer two probes are connected to high impedance current source, and voltage across the two inner probes is measured using a voltmeter as shown in Figure 2.7.
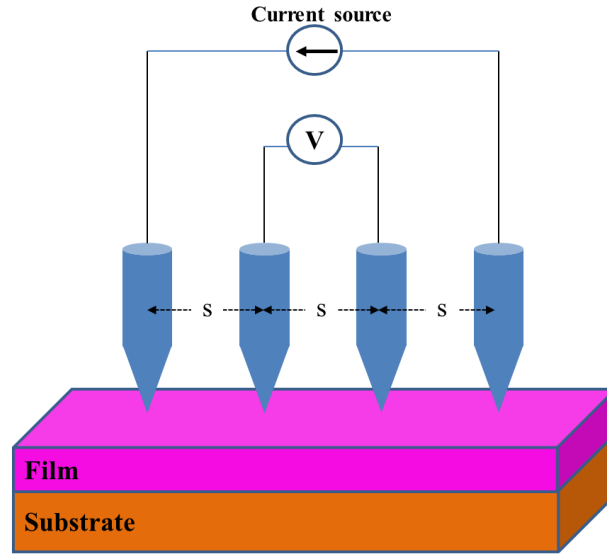
Figure 2.7: Schematic of four point probe method.

When the spacing s is 1 mm, the sheet resistance of the film can be calculated by measuring the voltage (V) across the inner two probes by applying current (I) through the two outer probes (Smits, 1958). That is:

$$R_s = \frac{\pi}{ln2} \times \frac{V}{I} \qquad (2.3)$$

where, $\frac{\pi}{ln2}$ is the correcting factor.

If the film thickness (t) is known the resistivity (ρ) can be calculated from the following formula

$$\rho = R_s \times t \qquad (2.4)$$

The sheet resistance measurements were carried out at five locations (i.e., four at corners and one at middle of the sample). The values reported herein are the average of five values.

2.5.5 Kelvin probe method

Kelvin probe was used to measure the work function of conducting specimen. It is a non-destructive, no-contact and indirect method to measure the work function of the sample. In Kelvin probe method the contact potential difference (V_{CPD}) of the sample and the probe tip is measured in close proximity. The V_{CPD} will be equal to the difference in work function of the sample and the probe tip (Rosenwaks et al., 2004).

34

Generally, gold tip with known work function is used in Kelvin probe technique. In this work, a Kelvin probe (Model SKP 5050) was used to find out the work function of ITO thin films. The calibration was done using a standard gold sample provided by KP Technology. Gold tip with a diameter of 2 mm was used for the work function measurements.

2.5.6 X-ray diffraction

The crystal structure of the samples was evaluated by X-ray diffraction (XRD) technique. XRD is a non-destructive technique used to determine the crystal structure, defects, lattice constant, identification of unknown materials, etc. XRD works on basis of Bragg's law (Cullity, 1956),

$$2dsin\theta = n\lambda \qquad (2.5)$$

where d is the interplanar distance between two parallel planes of the crystal structure, θ is the angle of incidence of X-ray on the sample surface, λ is the wavelength of the incident monochromatic X-ray and n is the order of the reflection. When the X-rays falls on the material, the reflected rays which satisfy the Bragg's equation will constructively interfere and provides peak at a particular 2θ angle. The crystalline solids, with periodically arranged planes, give high intense peaks at particular 2θ angles. However, due to the non-periodic and scattered arrangement of atoms in the case of amorphous solids, the reflected rays will be scattered and the XRD peaks are generally broad or null.

In this work structural characterization of the samples was performed using XRD of model Advanced D8 by Bruker. Measurements were done at thin film mode with a glancing angle 1°, and the data were recorded in the range of $5^{\text{o}} \leq 2\theta \geq 100^{\text{o}}$. Cu Kα radiation of wavelength 1.5406 Å was used for the characterization.

2.5.7 X-ray photoelectron spectroscopy

X-ray photoelectron spectroscopy (XPS) is a surface analysis techniques used to study the chemical structure of the materials (Lee and Flynn, 2006). XPS can be used to study the elemental composition, empirical formula, chemical state, electronic state and presence of different elements, etc. XPS works on the basis of photoelectric effect

(Brundle and Baker, 1978). When the high energy X-ray falls on the material photoionization takes place on the sample surface and the electrons will be liberated with a characteristic kinetic energy, the equation for this could be written as,

$$E_p = E_B + K_e \qquad (2.6)$$

where E_p is the incoming photon energy, E_B is the binding energy and K_e is the maximum kinetic energy of the ejected electron. Chemical bonding and the electronic structure of the material can be studied by analysing the kinetic energy distribution of the emitted photoelectrons from the sample.

In this work, the chemical composition of samples was determined using X-ray photoelectron spectroscopy (XPS– SPECS), using non-monochromatic Al Kα radiation (1486.6 eV). The binding energies reported here were calculated with reference to C1s peak at 284.6 eV with a precision of 0.1 eV. XPS survey scan was carried out in the range of 0 to 1150 eV. The survey spectra were recorded with pass energy of 70 eV and step increment of 0.5 eV. Whereas individual core level spectra were obtained with pass energy of 40 eV and step increment of 0.05 eV.

2.5.8 Field emission scanning electron microscopy

Field emission electron microscopy (FESEM) coupled with EDAX is used to study the morphology and elemental information of the samples with a magnificent range from 10 X to 300000 X. In FESEM electrons are used to scan the sample surface. The primary electrons are generated within a high vacuum column (10^{-6} Pa) from a sharp pointed tungsten filed emission source (Zhou and Wang, 2006). The electrons are accelerated in a high electric field gradient between 0.5 to 30 KV towards the anode. Within the high vacuum column these electrons are deflected and focussed by electronic lenses to produce a narrow scan beam that interacts the sample. During the bombardment of high energy electrons on the surface, secondary electrons, back scattered electrons, characteristic X-rays, photons and auger electrons are produced. Topographic information with excellent resolution can be attained by analysing the secondary electron from the sample surface. The back scattered electrons are produced due to the elastic collision between the electron and the atomic nucleus of the sample surface. Back scattered electrons are used to study the compositional and topographic

36

properties of the sample. X-rays are formed due to the displacement of inner shell electron by the primary electron, which can be used for the compositional characterization of sample. FESEM can produce very clear image with a resolution < 2 nm. In this work, surface morphology of the thin films and the substrates was studied using FESEM (Supra 40 VP, Carl Zeiss). Also, the thicknesses of the coatings were studied by cross-sectional FESEM images. For cross-sectional FESEM studies films were coated on silicon substrate.

2.5.9 AFM and 3D profilometer

Atomic force microscopy (AFM) gives a very detailed information about the surface morphology and the roughness of the samples (Karbach and Drechsler, 1999). AFM works based on the interaction between sample surface and the sharp probe, which scans over the surface of the sample. The probe is connected to a cantilever tip and a laser beam is used to measure the deflection of the cantilever tip. While scanning the sample surface, the cantilever deflects from its original position proportional to the topographical information of the sample surface. Even angstrom level deflection of the cantilever can be identified by the laser and it is recorded by a photodiode to generate corresponding surface image of the sample (Binning et al., 1986; Fix et al., 2005).

In this work, the surface morphology and roughness of the thin films and substrates were studied using AFM with tip size of 10 nm (Anton-Parr Instruments). 3D profilometer deve loped by Nanomap 500LS (AEP Technologies) with a tip size of 100-150 nm was used for measuring the thickness of ITO and ITO/Ag/ITO thin films.

2.5.10 Adhesion test

Adhesion of ITO thin film on FEP and Kapton® substrates was examined by tape peel off test as per ASTM D3359 standard using 3M Scotch® tape (3M-250) (ASTM D3359-07, 2007). For this, four sides of the ITO coated FEP or Kapton® substrates were fixed on a flat surface by adhesive tape. After that 3M Scotch tape was applied on the coating and then removed the tape normal to the ITO coating. The tape test was repeated two times to see the repeatability of the measurements.

2.5.11 Simulated environmental tests

Environmental tests such as thermo-vacuum (TVAC), thermal cycling (TC), relative humidity (RH) of ITO coated FEP, Kapton® and aluminized Kapton® substrates were performed at ISRO satellite centre (ISAC), Bangalore (Reddy et al., 2013). Relative humidity test was performed in a humidity chamber that is thermostatically controlled. Relative humidity of 95±5% at 50°C was maintained in the testing chamber. Thermal-cycling test was performed to study the effect of cycling temperature on the ITO coated FEP and Kapton® substrates. During TC test, the samples were first kept in a chamber maintained at temperature of -150°C for 5 min duration then suddenly the samples were moved to the separate chamber maintained at temperature +150°C and kept for 5 min. The samples were exposed to this cycling for 1500 times in a thermostatically controlled chamber. Thermo-vacuum test was performed in a thermostatically controlled vacuum chamber which maintained at a pressure of <1.33×10^{-5} mbar and simulated space environment conditions like temperature extremes of +150⁰C to -150⁰C. During TVAC test, the samples were kept at -150°C for 2 h and then the temperature was increased to +150°C and maintained at that temperature for 2 h. Like this 10 cycles were performed.

CHAPTER 3

OPTICAL AND ELECTRICAL PROPERTIES OF ITO THIN FILMS SPUTTERED ON FLEXIBLE FEP SUBSTRATE

In this Chapter optimization of deposition parameters and characterization of ITO thin films on flexible fluorinated ethylene propylene (FEP) substrate for spacecraft applications are discussed. The influence of the deposition parameters (argon and oxygen flow rates, and substrate temperature) and effect of coating thickness on the optical, electrical, structural and microstructural properties of ITO thin films deposited on FEP is also discussed.

3.1   Introduction

ITO coated metalized FEP substrate is used in most of the satellites stationed in geostationary earth orbits (GEO) as passive thermal control system by radiating back the incoming solar radiation. Figure 3.1 shows the schematic representation of FEP based flexible optical solar reflector (FOSR) with ITO coating. An efficient FOSR for GEO satellite applications should have high thermal emittance (>75%), high solar transmittance (>88%) and sheet resistance in the range of 2-10 kΩ/square. The high transmittance of ITO in FOSR can be obtained by reducing the thickness of ITO coating to few nanometers (Czeremuszkin et al., 2001). Therefore, there is a need to critically optimize the process parameters and hence the properties of the ITO thin films for FOSR applications. However, detailed description of ITO coated FEP substrates is missing in the literature.
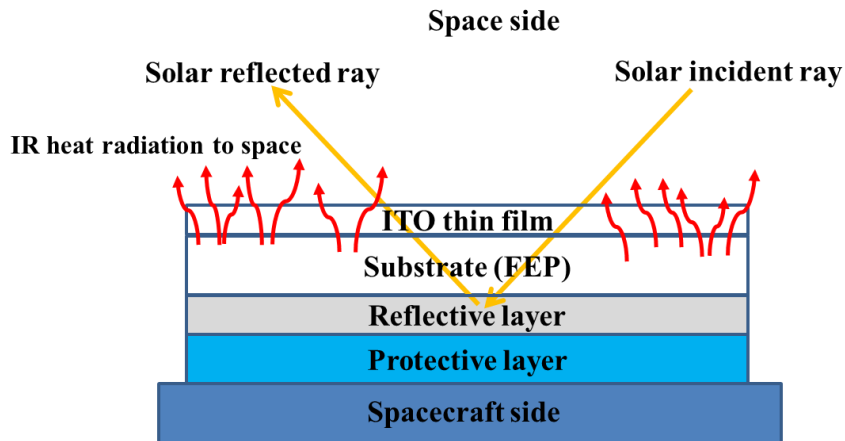
Figure 3.1: Schematic representation of FEP based optical solar reflector.

3.2   Experimental details

ITO thin films were deposited on flexible FEP substrates by reactive sputtering using a DC balanced magnetron sputtering system using In:Sn metal alloy target. FEP substrates of 40 mm × 40 mm size were used in all the experiments. Before introducing into the chamber, FEP substrate was cleaned with iso-propylene alcohol in ultrasonic agitator for 5 min and then blown dried with nitrogen gas. The sputtering gases used in the experiments were argon and oxygen. Prior to all deposition, the target was cleaned under argon plasma for 1 min. All the depositions were done using pulsed DC power supply which was kept constant at 60 W power.

In order to study the influence of argon and oxygen partial pressures on the ITO deposition the flow rates were varied from 11 to 17 sccm and 1.8 to 3 sccm for argon and oxygen, respectively. While for all other depositions the flow rates of argon and oxygen were kept constant at 11.5 sccm and 2.0 sccm, respectively. Substrate temperature was varied from room temperature to 140°C. However, all the optimized coatings were deposited at a substrate temperature of 140°C. By varying the deposition time, ITO thin films with different thicknesses were prepared. The thickness of the ITO coatings was varied from 5 to 1000 nm. ITO thin films were also coated on silicon and glass substrates at optimized parameters to measure the roughness, thickness and work function of the coatings.

3.3 Results and discussion

3.3.1 Optimization of ITO deposition parameters

To achieve highly transparent, conducting and adherent ITO thin films on flexible FEP substrate is a challenge because of its low melting point (260⁰C). Therefore, various process parameters were optimized systematically. From the preliminary experiments, it was noticed that the ITO thin films prepared at low target power (i.e., < 30 W pulsed DC), the optical and electrical properties were not stable in atmosphere as compared to the films deposited at higher target power. However, high target power caused deformity and warpage of the FEP substrate because of its low safe operating temperature. So, for compromising both the problems 60 W pulsed DC power is used for all the experiments.

Among all the deposition parameters, the flow rates of oxygen and argon are the most influential parameters for obtaining transparent and conducting ITO thin films (Chen et al., 2014; Jung et al., 2004). The influence of oxygen and argon gas flow rates during the reactive sputtering on the optical properties of ITO thin films on FEP substrate has been studied. ITO thin films are deposited at different oxygen and argon flow rates, keeping film thickness at 30 nm and substrate temperature at 140°C. The oxygen flow rate was varied from 1.8 to 3 sccm while keeping the argon flow rate at 11.5 sccm. From the transmittance spectra shown in Figure 3.2(a) it is clear that varying oxygen flow rate during the deposition changes the optical transmittance of ITO films on the FEP substrate. At higher oxygen flow rate (3.0 sccm) the average transmittance of ITO on FEP was excellent (93.7%), even the transmittance at NIR region was almost equal to the transmittance of uncoated FEP substrate. But the sheet resistance was very high (~2 MΩ/square), for these coatings. Upon decreasing the oxygen flow rate the transmittance and sheet resistance were also found to decrease. In ITO thin films the charge carriers originate through oxygen vacancy ($V_0^{\bullet\bullet}$) and Sn^{4+} doping in the site of In^{3+} (Edwards et al., 2004; Tahar et al., 1998). Here, only oxygen flow rate was varied, all other parameters were kept constant, so the charge carriers mainly originate from oxygen vacancy present in the film due to insufficient oxygen flow during the deposition.

A slight variation in the oxygen flow rate during deposition changes the optical and electrical properties of ITO thin film drastically. The high sheet resistance at higher

41

oxygen flow rate is due to the complete oxidation of ITO thin film. It is observed that if the oxygen flow rate is changed even by 0.2 sccm after the optimized value of 2.0 sccm the transmittance of ITO decreases significantly. This shows that the film becomes more metallic with more oxygen vacancies, which help to decreases the sheet resistance but deteriorates the optical performance of the film. Mientus and Ellmer have reported that an exact amount of reactive oxygen, pO_{2min}, is needed to oxidize the metal atoms arriving at the substrate to have the minimum resistance and good optical transmittance (Mientus and Ellmer, 2001).

Figure 3.2(b) shows the variation of solar transmittance of ITO coated FEP at argon flow varying from 11 to 17 sccm with the oxygen flow rate constant at 2.0 sccm, thickness of 30 nm and substrate temperature of 140°C. From this figure it can be noticed that argon flow rate has less influence as compared to the oxygen flow rate on the transmittance of ITO coating. Therefore, by comparing Figures 3.2(a) and (b) it is very clear that the transmittance in the visible region is affected mainly by the oxygen flow rate.
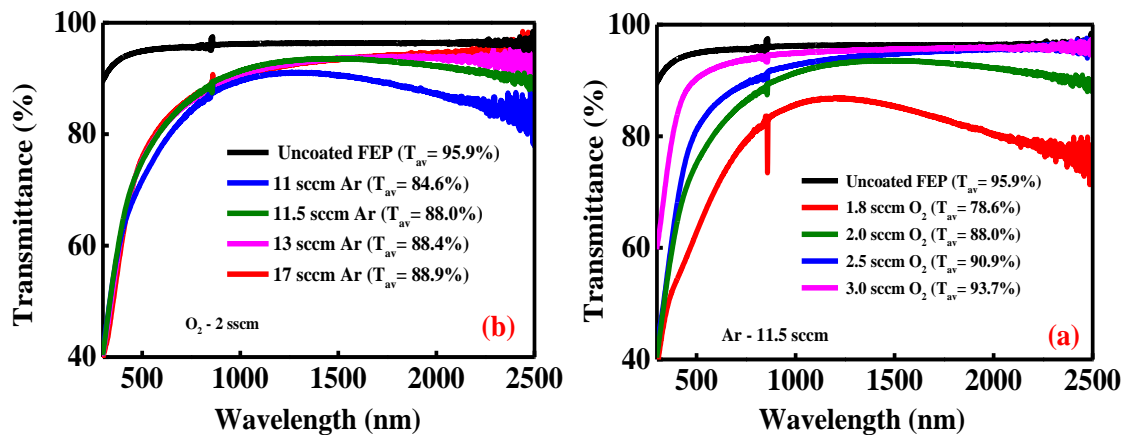
Figure 3.2: Total solar transmittance spectra of ITO thin films prepared at different: (a) oxygen flow rates and (b) argon flow rates.

As during the sputtering the substrate temperature (T_S) controls the crystallinity of the deposited coatings, the effect of substrate temperature on the transmittance and sheet resistance (R_S) of ITO films deposited on FEP substrate was investigated. For this a 30 nm thick ITO film was deposited on FEP substrate at different substrate

temperatures while keeping argon and oxygen flow rates at 11.5 and 2.0 sccm, respectively. Since the safe operating temperature of FEP films lies below 200°C, all the experiments were carried out at substrate temperature below 140°C. Figure 3.3 shows the transmittance spectra of ITO coatings deposited on FEP at substrate temperatures varying from room temperature (R.T.) to 140°C. The variation of sheet resistance is shown in Figure 3.4. Optical transmittance of ITO coatings did not change much with the substrate temperature, but a minor decrease in the transmittance at NIR region with an increase in the substrate temperature was observed. Chang et al. also reported that the substrate temperature merely affects the transmittance of the ITO on polyethylene terephthalate (PET) substrates (Chang et al., 2013). But in the case of sheet resistance considerable change can be seen while increasing the substrate temperature (see Figure 3.4). The ITO coated FEP substrate, which was prepared at room temperature, shows sheet resistance of ~900 Ω/square with an average solar transmittance of 88.5%. For the coating prepared at a substrate temperature of 140°C the sheet resistance decreased to ~400 Ω/square and the average transmittance was 88.0%. ITO thin films prepared at higher substrate temperature usually are crystalline in nature, at the same time ITO films prepared at lower substrate temperature are amorphous in nature. As the film grew thicker with a higher degree of crystallinity, the oxygen vacancies and the substituted Sn atoms would have a higher possibility to produce more free electrons, which increases the electrical conductivity. From the above data it can be concluded that the electron concentration is increased with an increase in the substrate temperature and that is attributed to the decrease of sheet resistance and transmittance at NIR region of ITO coated FEP substrate (Tuna et al., 2010).
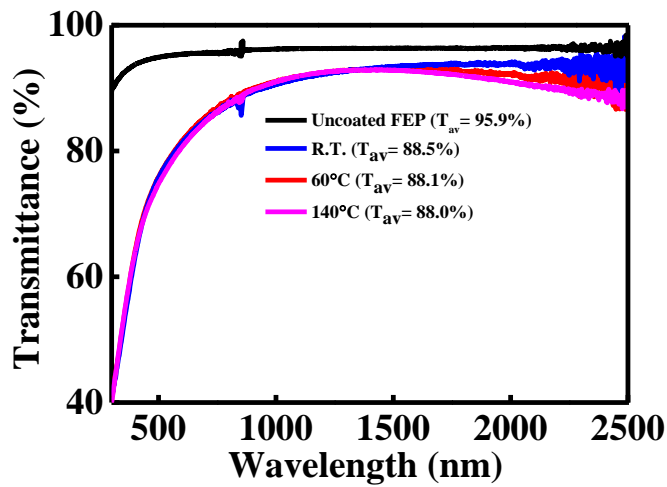
Figure 3.3: Solar transmittance spectra of ITO thin films prepared at different substrate temperatures.
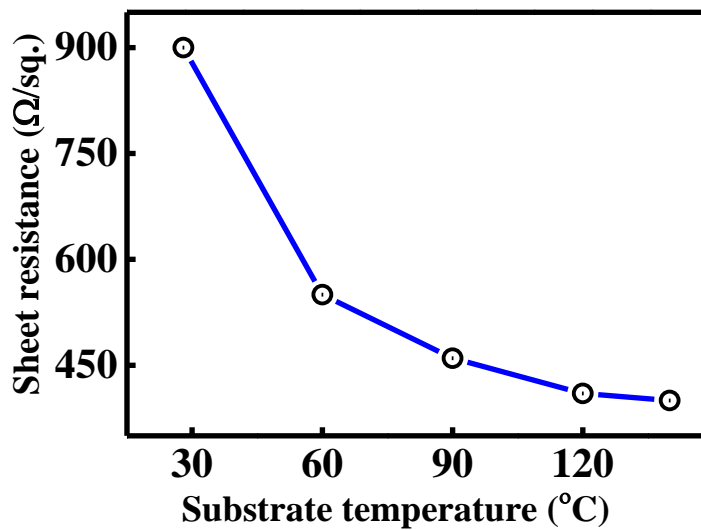
Figure 3.4: Variation of sheet resistance with substrate temperature of 30 nm ITO films prepared at 11.5 sccm argon and 2.0 sccm oxygen flow rates.

3.3.2 X-ray diffraction studies

The XRD data of sputtered ITO thin films on FEP substrate along with XRD data of an uncoated FEP are shown in Figure 3.5. It shows that at lower thicknesses sputtered ITO thin films are amorphous. Further, by increasing the thickness, the

crystallinity improves and ITO peaks are clearly visible above 180 nm. No detectable XRD signal was obtained for 5, 8, 10 and 20 nm thick ITO coatings. It has been reported in literature that the crystallinity of ITO thin films depends mainly on the substrate temperature and the thickness of the film (Lee and Park, 2006; Meng and Santos, 1998; Qiao et al., 2004). In the present case, amorphous ITO thin films were obtained when the substrate temperature was 140°C for lower coating thicknesses. Upon increasing the thickness (i.e., 180 nm) a weak (222) diffraction starts appearing and finally at 1000 nm thickness a prominent (222) diffraction peak along with some other (211), (400), (440), (622) diffraction peaks of cubic ITO having low intensities were observed. It is to be noted that the optimized ITO coatings of the present work for FOSR applications were amorphous in nature.
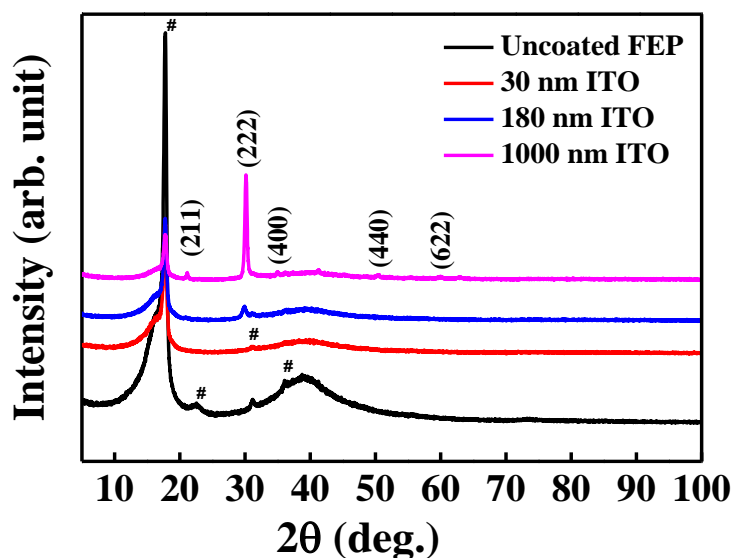
Figure 3.5: XRD patterns of 30, 180 and 1000 nm thick ITO thin films deposited on FEP substrate. # denotes reflections from FEP.

3.3.3 XPS studies

To find out the surface chemical composition of ITO thin films XPS of 30 nm thick ITO film deposited on FEP was taken. Figures 3.6 (a-c) show the core level XPS spectra of In, Sn and O, respectively.
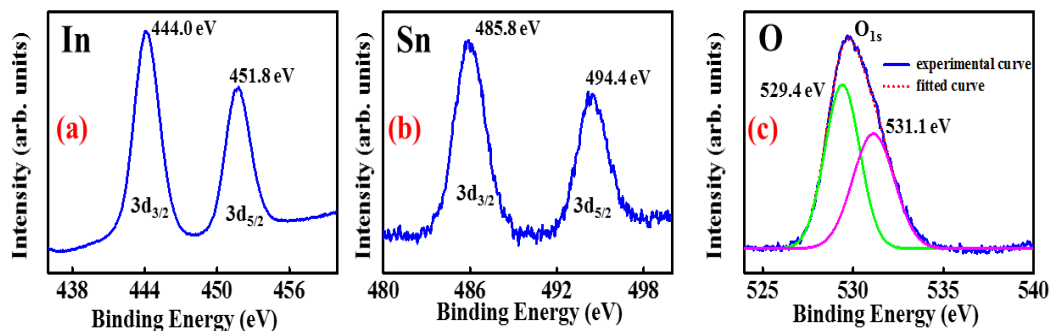
Figure 3.6: (a), (b) and (c) show the XPS core level spectra (In 3d, Sn 3d and O 1s) of ITO thin film having thickness of 30 nm.

The observed binding energies of In $3d_{3/2}$ and $3d_{5/2}$ peaks are 444.0 and 451.8 eV (Figure 3.6(a)) (Fan et al., 1977; Nelson and Aharoni, 1987; Tetsuka et al., 2008). The binding energies of Sn $3d_{3/2}$ and $3d_{5/2}$ peaks are found at 485.8 and 494.4 eV, respectively (Figure 3.6(b)) (Fan et al., 1977; Nelson and Aharoni, 1987; Tetsuka et al., 2008). O 1s spectrum (Figure 3.6(c)) could be fitted with two components, with binding energy values of 529.4 and 531.1 eV. From the literature it is found that the peak at lower binding energy (529.4 eV) corresponds to the bonded oxygen in the amorphous In_2O_3 region and the peak at higher binding energy (531.1 eV) comes from the oxygen deficient region of In_2O_3 matrix (Chen et al., 2014; Chuang, 2010). The O 1s spectrum of as-deposited ITO thin film does not show any oxygen contamination, hydroxide or any other impurity peaks, which suggests a stoichiometric nature of ITO thin films (Chen et al., 2004; Chuang, 2010; Sugiyama et al., 2000).

3.3.4 Microstructural studies

Figures 3.7(a), (b) and (c) show the FESEM micrographs of ITO thin films of 30, 60 and 90 nm thick on FEP substrates, respectively. From these micrographs a smooth growth pattern of ITO film on FEP at lower thickness with dense morphology can be observed. At higher thickness granular microstructure was formed, which is reported to be typical for the ITO thin films deposited at lower substrate temperature (Herrero and Guille, 2006; Kumar et al., 2011; Qiao et al., 2004). Lee and Park also noted that as the ITO film grew thicker, grain size of the film became larger and film

morphology changed from the homogeneous and smooth morphology with vague grain boundary to the non-homogeneous and rough morphology with clear grain boundary (Lee and Park, 2006). These FESEM results are corroborated with the XRD results, which showed grain size increase with an increase in the thickness of ITO film. The surface morphology and roughness of ITO thin films have been also studied by AFM. Silicon substrate is used for the surface roughness studies because the surface roughness of the FEP substrate was comparatively higher ($R_a = \sim5.49$ nm). Figures 3.7(d), (e) and (f) show the AFM data of 30, 60 and 90 nm ITO with an average roughness of 0.49, 0.76 and 0.92 nm, respectively. The thickness of the ITO films was evaluated from the cross-sectional FESEM images and 3D-profilometers deposited on silicon substrates. Figures 3.8(a) and (b) show the cross-sectional FESEM images of 180 and 1000 nm ITO films deposited on Si substrate, displaying thicknesses of ~180 and ~1000 nm, respectively, which are consistent with profilometer data as shown in Figures 3.8(c) and (d).
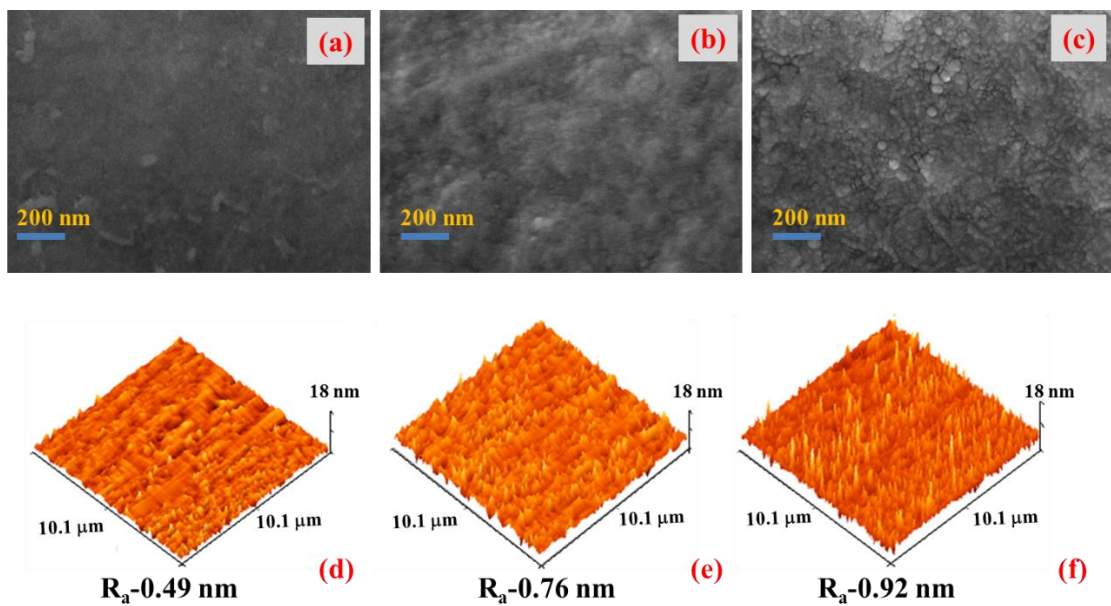
Figure 3.7: (a), (b) and (c) show the FESEM images of 30, 60 and 180 nm thick ITO deposited on FEP and (d), (e) and (f) show the corresponding AFM images deposited on silicon substrates.
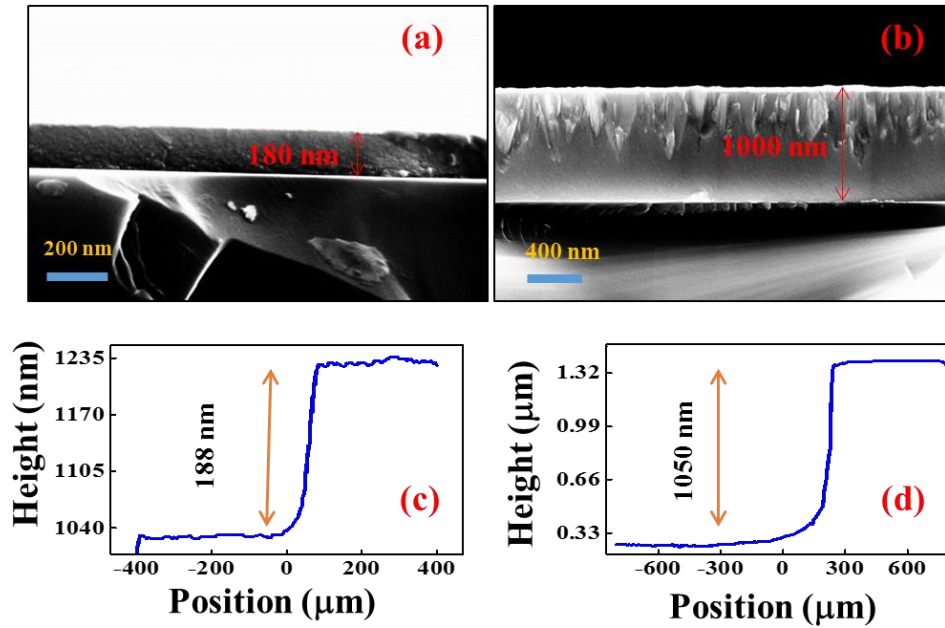
Figures 3.8: (a) and (b) show the cross-sectional FESEM images of ~180 and 1000 nm thick ITO thin films. (c) and (d) show the thickness profiles of the same.

3.3.5   Optical and electrical characterization

Figure 3.9 shows the transmittance and reflectance spectra of ITO coated FEP substrates with different thicknesses in the solar spectrum (300-2500 nm) region. For more clarity the data has been presented in two thickness regimes: 5 to 30 nm and 60 to 180 nm. Figures 3.9(a) and (b) show the transmittance and reflectance spectra up to 30 nm thickness, which clearly depicts that, at lower thicknesses, the transmittance and reflectance spectra are smooth. However, as the film thickness increases from 60 to 180 nm (Figures 3.9(c) and (d)), multiple peaks are visible in the transmittance and the reflectance spectra due to the interference of light passing through the transparent ITO film (Bingel et al., 2013). The reflection spectra in low thickness regime (Figure 3.9(b)) also show that there are no multiple reflection peaks present at lower thicknesses. However, as the thickness of the film increases (Figure 3.9(c)), multiple reflection peaks appeared at lower wavelength and red shift was observed in the spectra. As the refractive index of ITO coating is higher (~2.0 at 550 nm) than the FEP substrate (~1.34 at 550 nm), at quarter wavelength thickness (e.g., high intense peak at 680 nm wavelength for ~180 nm thick ITO coating), reinforcement occurs between the light

48

waves reflected from both sides of the film (ITO being a transparent material), resulting in an increase in the reflectance (Bingel et al., 2013; Heavens, 1955; Kerkache et al., 2009). The shift in the peak position in reflectance maxima with film thickness further corroborates this statement.

Figure 3.10 shows the variations of average transmittance and sheet resistance of ITO thin film with an increase in the coating thickness. It has been observed that average transmittance and sheet resistance decreased with an increase in ITO film thickness. The highest average transmittance was observed for 5 nm thick ITO film (~95.1%), while 8, 10, 15, 20 and 30 nm ITO films showed average transmittance of 94.8, 94.0, 92.0, 90.9 and 88.0%, respectively.
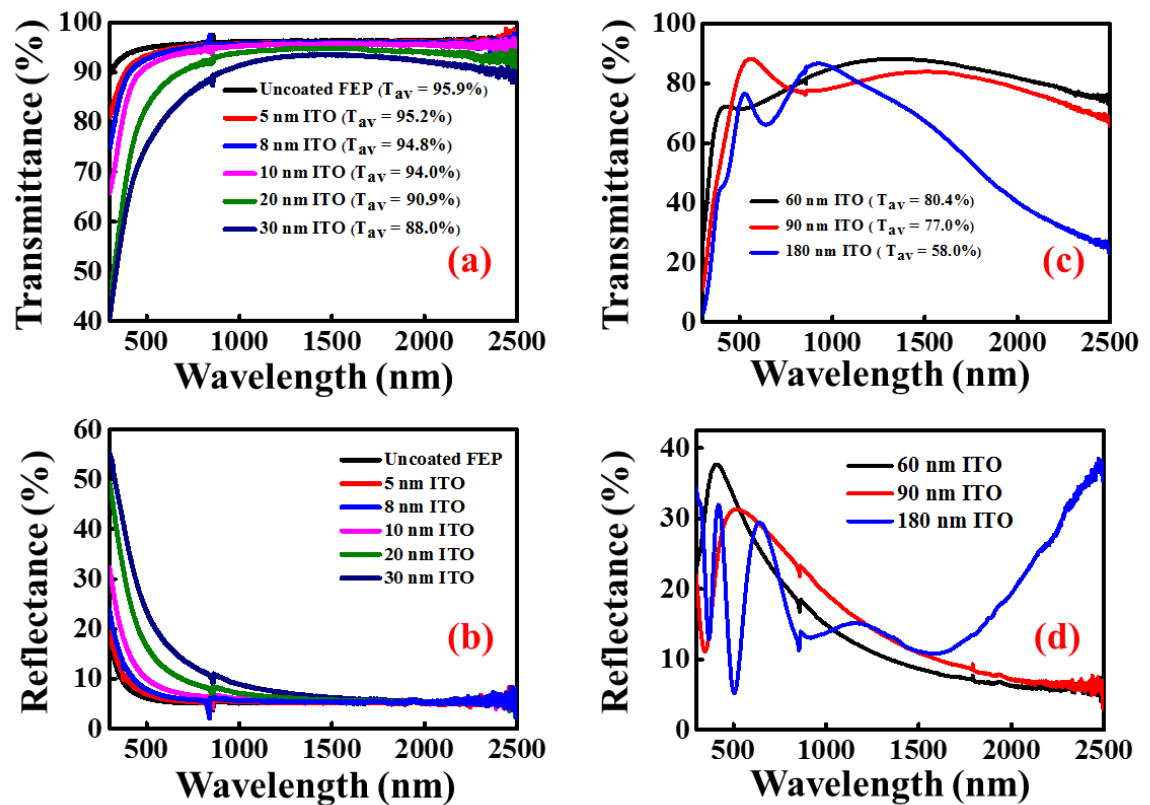
Figure 3.9: UV-Vis-NIR transmittance and reflectance spectra of different thickness ITO films. For clarity the data has been recorded in two thickness regimes: (a) and (b) 5 to 30 nm and (c) and (d) 60 to 180 nm.
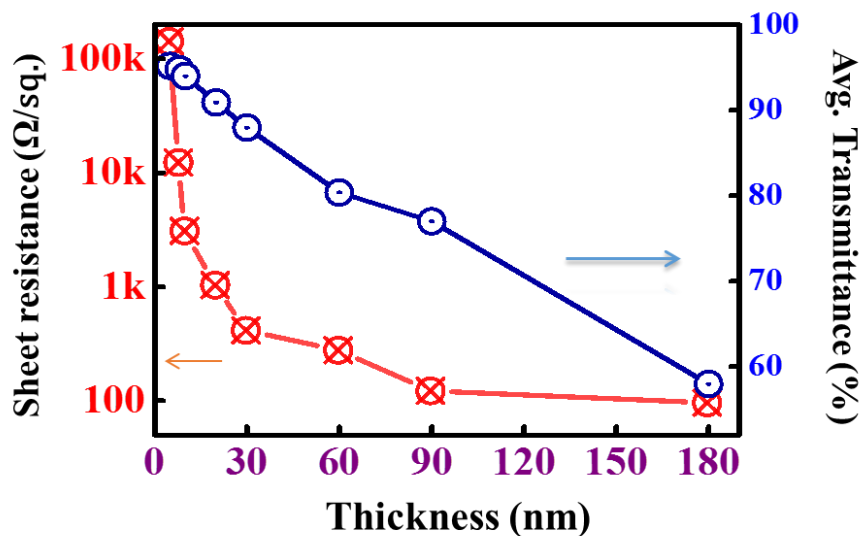
Figure 3.10. Average transmittance and sheet resistance of ITO thin films deposited on FEP as a function of thickness.

As the ITO thickness increases from 5 to 8 nm, an abrupt decrease in the sheet resistance value (140 kΩ/sq. to 12 kΩ/sq.) has been observed, but only a minor decrease in the average transmittance was noticed; 10 to 15 nm ITO coatings also showed decrease in the sheet resistance as 3 to 2 kΩ/square However, at higher thicknesses the sheet resistance remains low and decreases marginally with thickness (400, 267, 117 and 92 Ω/square for 30, 60, 90 and 180 nm, respectively). For thickness <30 nm, the average transmittance did not change much but in the visible region, the transmittance was seen to be decreasing continuously (Figure 3.9(a)). This is mainly attributed to the grain growth of ITO as the thickness increases there is a greater chance for the scattering of light to take place (Bingel et al., 2013; Kerkache et al., 2009). But at higher thickness, the average transmittance decreased significantly. The transmittance and the sheet resistance at higher thickness mainly depend on the charge carriers present in the film (Eshaghi and Graeli, 2014; Wang et al., 2013). When the thickness of ITO thin film increases, the density of the charge carriers increases as more number of free electrons are available for the conduction and also because of improved crystallinity (as seen in Figures 3.5 and 3.7) which helps for less scattering (or increased mobility) of electrons. These reasons lead to high conductivity of the ITO thin film. Also, the enhanced crystallization at higher thickness increases the probability of doping of Sn^{4+} in the

place of In^{3+} ions in a crystallized In_2O_3 site (Edwards et al., 2004; Lee and Park, 2006). The NIR transmittance at higher thicknesses (Figure 3.9(c)) showed a considerable decrease compared to lower thickness ITO films. This is attributed to the well-known free carrier absorption (Bingel et al., 2013; Edwards et al., 2004). The free carrier density produced through Sn^{4+} doping and $V_0^{\bullet\bullet}$ affects the plasmon frequency absorption at NIR region, as described by the equation (1.4). After plasma edge, transmission will be low and reflection will be more as seen in Figures 3.9(c) and (d) (Edwards et al., 2004). The abrupt decrease in the transmittance spectra in the UV region (Figures 3.9(a) and (c)) is attributed to the strong absorption due to the band gap of ITO thin film (Granqvist, 2007).

3.3.6 Band gap energy calculation

From the absorption spectra of different thicknesses of film sputtered on FEP substrate, the optical band gap was calculated using the relation (Han et al., 2006):

$$\acute{\alpha}E_p = k_1(E_p - E_g)^{1/2} \qquad (3.2)$$

where, $\acute{\alpha}$ is the absorption coefficient, E_p is the discrete photon energy (eV), k_1 is a constant and E_g is the average band gap energy (eV). From Figure 3.11(a) it can be observed that optical band gap of ITO thin films on FEP marginally depend on the film thickness. This can be described by well-known Burstien-Moss phenomenon (Han et al., 2006; Tuna et al., 2010). Due to the increased charge carrier developed with increasing thickness, as discussed above, the lower energy level of conduction band will get filled; subsequently the band gap will increase (Tuna et al., 2010). The decrease in the sheet resistance and the transmittance at NIR region also gives the evidence of increased charge carrier density. Figure 3.11(a) shows a typical plot between $(\acute{\alpha}E_p)^2$ and E_p of 10 nm ITO film.
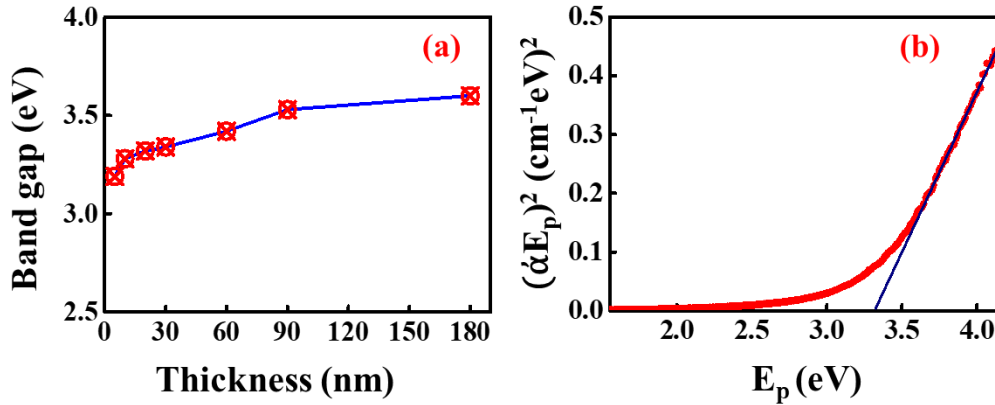
Figure 3.11: (a) Variation of optical band gap energy (E_g) with thickness of ITO thin films. (b) Shows the relation between $(\acute{\alpha}E_p)^2$ and E_p of 10 nm thick ITO film on FEP substrate.

3.3.7 Work function measurement

Work function measurements of the ITO coatings were carried out to understand the effect of film thickness on the electrical property. It may be noted that these measurements could not be carried out on 10 and 30 nm thick ITO coating on glass substrate because of instrument limitation (very low signal). Figure 3.12 shows the work function contour plot for a typical 60 nm thick ITO film measured using a Kelvin probe technique of area 3 mm × 3 mm. These measurements indicated that an average work function of 5.2 eV was observed for 60, 90 and 180 nm thick ITO films, which is consistent with the reported literature (Sharma et al., 2009).
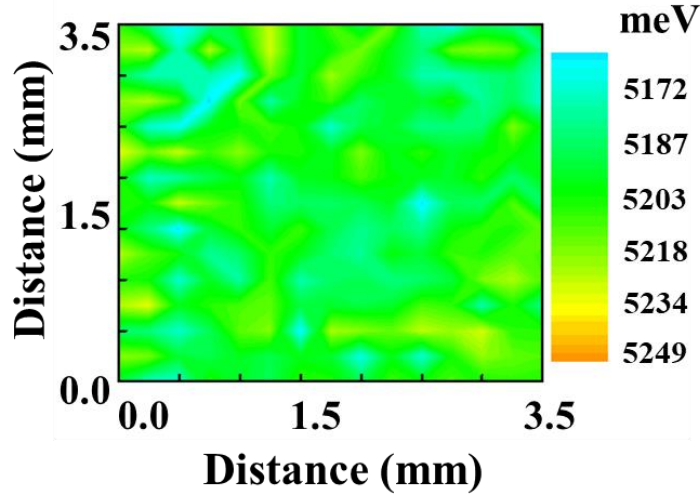
Figure 3.12: Work function plot for a 60 nm ITO thin film deposited on glass.

3.3.8 Angular reflectance of ITO coating on FEP substrate

Generally, the optical properties of ITO coatings are characterized using an unpolarized light at near normal incidence. In applications like solar energy harvesting and satellites the angle between the FOSR device and the sun changes from time to time, so the angle of incidence and the polarization state of the light substantially affect the optical properties of the films. Therefore, the study of dependence of angle of incidence to the reflection of ITO is useful (Chang et al., 2011; Selvakumar et al., 2015). Using the universal reflectance accessory of the Lambda 950 spectrophotometer, the angular dependent absolute transverse electric (*s*-polarization) and transverse magnetic (*p*-polarization) reflectance measurements were taken and the data are shown in Figures 3.13(a)-(c). The reflectance measurements were taken at varying angles (8 to 68°) of the incident beam, in the 300-2500 nm wavelength range.

For TE-polarization (*s*-polarization) (Figure 3.13(a)), the reflectance was found to increase with increasing angle of incidence. On the other hand, for TM polarization (*p*-polarization) (Figure 3.13(b)), the reflectance of ITO thin films was found to decrease with an increase in the angle of incidence, but beyond 58° the reflectance was found to increase. This phenomenon can be explained by well-known Brewster angle effect (Adamson, 2014; Heavens, 1955). That is, at Brewster angle, the incident light's electric field will align parallel to the incident plane, at that point the reflection will

vanish. Above 58°, i.e., at 68° incident angle, the reflection of ITO was found to increase. The average reflectance values of *s-* and *p-* polarized light were calculated [$R_{av.}= (R_{p-pol.}+R_{s-pol.})/2$] and are shown in Figure 3.13(c). This result shows that average angular reflectance of ITO film was less and did not change significantly for an incident angle up to 58°.
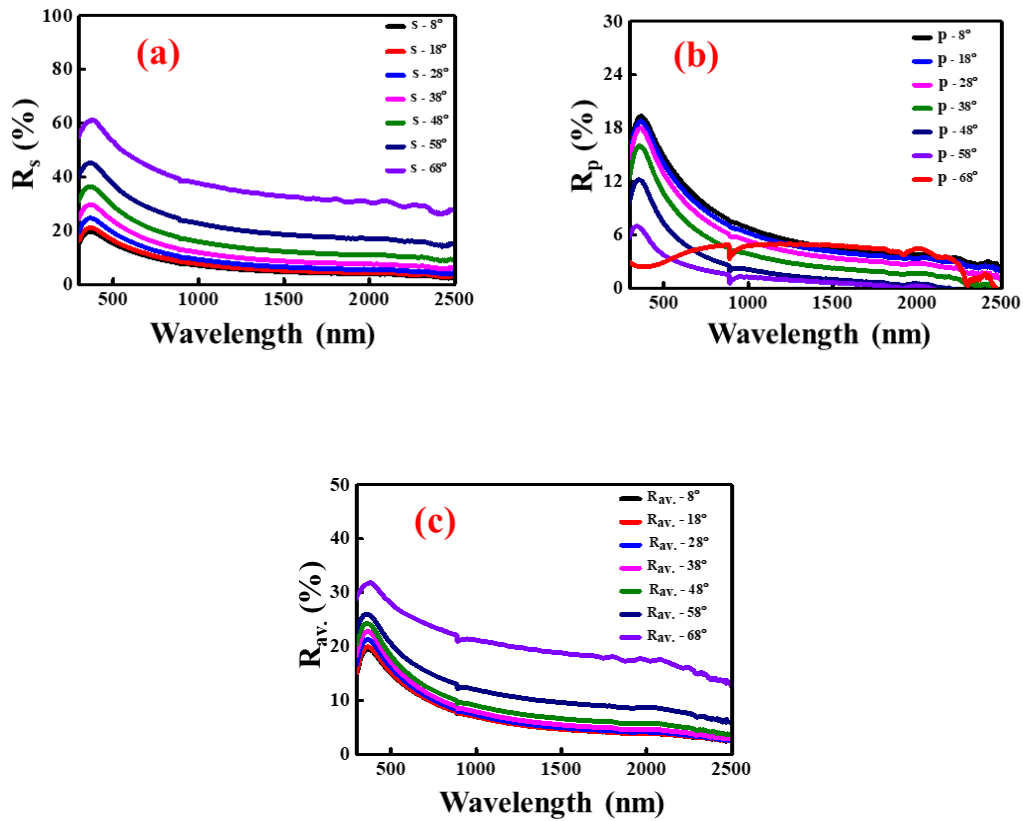
Figure 3.13: Angular reflection spectra of ITO thin films on FEP substrate: (a) s-polarization (b) p- polarization and (c) average reflectance $R_{av.} = (R_p+R_s)/2$.

3.3.9   Figure of merit

One of the indicators of the performance of the transparent conductors is the figure of merit. Accordingly, from the transmittance and sheet resistance data the figure of merit of ITO coatings was calculated as described by Haacke (Haacke, 1976):

$$\phi = \frac{T^{10}}{R_s} \qquad (3.3)$$

54

where, T is the optical transmittance at 550 nm which is represented in 0-1 scale and R_s is the sheet resistance of ITO coating. Figure of merit values of 5, 8, 10, 20 and 30 nm thick ITO thin films were found to be 3.82×10^{-6}, 4.24×10^{-5}, 1.46×10^{-4}, 6.49×10^{-4} and 2.14×10^{-4} Ω^{-1}, respectively. The figure of merit values of ITO thin films reported in this work are low compared to the recent reported values (Álvarez-Fraga et al., 2015; Pammi et al., 2011). That is because of the relatively high resistance of very thin (<30 nm) ITO films, which are required for the FOSR applications. It may be noted that for applications like transparent and conducting electrodes and display devices, the ITO thin films with very low resistance and high transmittance in the visible region are required (Álvarez-Fraga et al., 2015). On the other hand, for FOSR applications, ITO thin films with a resistance in the range of 2-10 kΩ/square and high transmittance over the entire solar spectrum are required.

3.3.10 Haze measurements

Previous studies have demonstrated that the haze measurement of transparent conducting coating is one of the important factors to be included in the figure of merit (Liu et al., 2011; Mahadik et al., 2015; Preston et al., 2013). The required haze factor is different for different applications. Low haze values are required for the application related to optical coatings where less absorption of light is required (Mahadik et al., 2015). But high haze value is favored for the solar coatings where more absorption of light is needed (Liu et al., 2011). High haze factor of the protecting layer will scatter the light and improve the light absorption of the solar active layer lying beneath the protecting layer (Liu et al., 2011). Low haze material will pass the light without any scattering and chances of absorption of light will be less (Mahadik et al., 2015). For the FOSR applications the absorption should be minimum; so that light should transmit through the FEP without any absorption (French et al., 2011). Accordingly, minimum haze value is required for better performance. The haze factor of the ITO coated FEP films was measured and calculated using the equation (2.2).

Figure 3.14 shows the corresponding spectra of haze factor with varying film thickness along with haze factor of uncoated FEP substrate. From the figure it can be seen that the average haze value of FEP (4.6%) increased with increasing ITO coating

thickness. The ultrathin ITO films (i.e., 5, 8, and 10 nm) did not show much increase in the optical haze value (5.8, 6.3 and 8.3%), but when thickness increased further, a considerable increase in the haze factor was found (e.g., 31.6% for 60 nm). This shows that increase in thickness will scatter the light and it will enhance the absorption of the solar reflector.
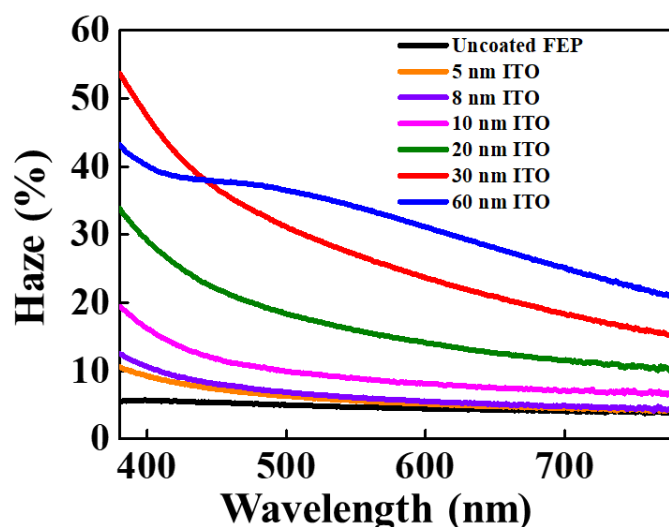
Figure 3.14: The optical haze data of ITO thin films having different thicknesses on FEP substrate.

3.3.11 Emittance of ITO coating on FEP substrate

The IR emittance of ITO coated FEP was measured using an emissometer. The 5 nm ITO coated FEP shows emittance of 80% and with increasing the thickness of ITO film a continuous decrease in the emittance of FEP was observed. 15 nm thick ITO coated FEP substrate showed an emittance of 79%. Decrease in the emittance with thickness is shown in Figure 3.15. The FTIR reflectance spectra of different thicknesses of ITO thin films on FEP substrates were taken and the data is shown in the inset of Figure 3.15. The IR reflectance of FEP was found to increase with increase of ITO film thickness in the mid IR region. The FTIR reflectance data of ITO films indicates that increasing thickness increases the reflectance of ITO film which affects the emittance of ITO coated FEP. From this result it can be understood that increasing thickness increases the absorption of light and it adversely affects the function of the FOSR.
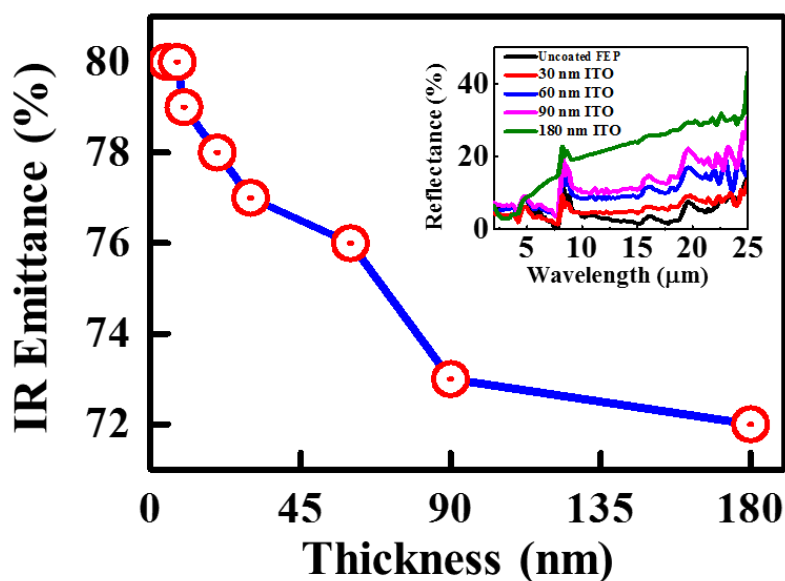
Figure 3.15: IR emittance of FEP substrate with varying thicknesses of ITO thin films. The inset shows the FTIR reflectance data of ITO thin films with different thicknesses on FEP substrate.

3.3.12 Coating adhesion

To find out the adhesion of ITO coatings on the FEP substrate tape peel off test as per the ASTM D3359 standard was carried out as discussed in section 2.5.10 of Chapter 2. 10 nm and 30 nm thicknesses ITO coated FEP substrates were used for the test. The test showed that there was no peeling off of ITO coating. Figure 3.16 shows the transmittance spectra of the coatings measured before and after the adhesion test for 10 and 30 nm thicknesses. From the plot shown in Figure 3.16 it can be observed that transmittance of the coating did not change. Additionally, the sheet resistance also did not change significantly after the adhesion test (Δsheet resistance <100 Ω/sq.), indicating better adhesive properties of the ITO thin films on FEP substrates in normal condition.
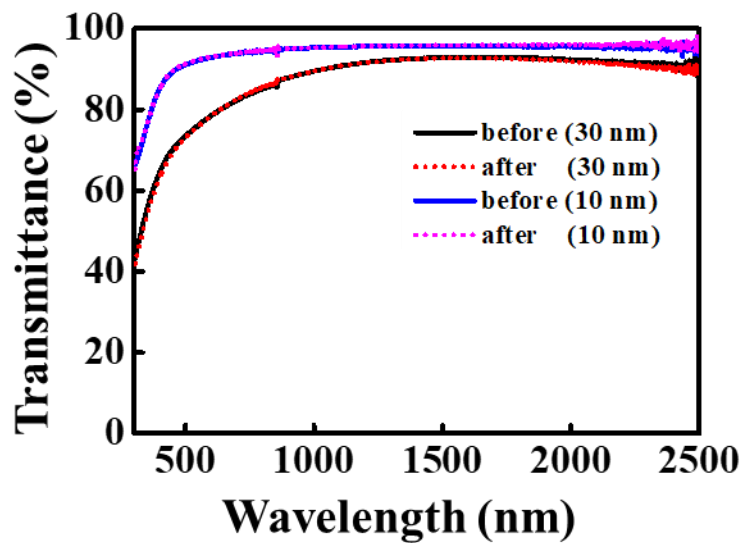
Figure 3.16: UV-Vis-NIR transmittance spectra of ITO thin films before and after adhesion test.

3.3.13 FOSR preparation

In an attempt to make an actual FOSR for space applications, ~150 nm highly adherent Ag layer was deposited on the other side of ITO coated FEP substrate (refer Figure 3.1, reflective layer). The thickness of the ITO thin film was kept 10, 20 and 30 nm for these experiments. Figure 3.17 shows the UV-Vis-NIR reflection spectra of a 10 nm ITO coated FOSR along with an ITO free FOSR. The IR emittance values of these FOSRs were 79, 77 and 76%, respectively for 10, 20 and 30 nm thick ITO thin films. These data show that additional ITO coating on FOSR did not significantly change its optical properties.
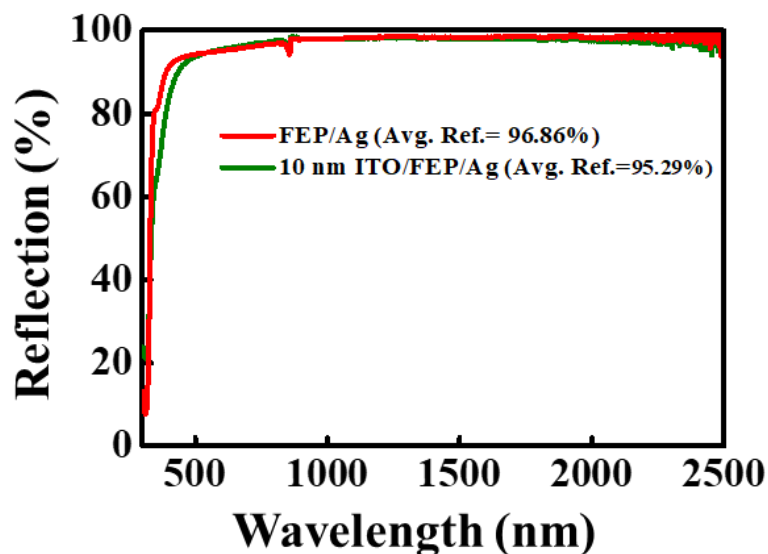
Figure 3.17: Reflectance spectra of FOSR with and without 10 nm ITO thin film coating.

3.4 Summary

Highly transparent and conducting ITO thin films were sputter deposited on flexible FEP substrate for space application using pulsed DC power supply at a substrate temperature of 140°C. The flow rate of oxygen critically affected the sheet resistance and the transmittance. At high oxygen flow rates the films were transparent, whereas, at low oxygen flow rates, the films were opaque but metallic in nature. The XRD data of different ITO thicknesses showed that at lower thickness the films were amorphous and with increase in thickness the thin films exhibited (222) reflection of crystalline ITO. The FESEM and AFM studies revealed the grain growth and an increase in the roughness of ITO film with increasing thickness. The emittance of FEP was found to be decrease with increasing ITO thickness. With increasing thickness, both average solar transmittance and sheet resistance were found to decrease, whereas at very low thickness (i.e., 5 nm) the ITO coating exhibited extremely high sheet resistance. Low haze value was achieved for low thickness ITO coating, which reduced scattering of light and subsequent absorption of light. When the ITO film thicknesses were in the range of 10 to 15 nm average solar transmittance was achieved > 90 % with sheet resistance of 2-10 kΩ/square and IR emittance of >75% for ITO coated FEP

substrate; these results are suitable for spacecraft applications. Angular reflectance data showed that reflection of ITO coating with TM polarization of light increased with incident angle but for TE polarized light reflection decreased with angle of incidence and after 58° reflection increased. No peel off of the ITO coating was noticed during the tape test, which concluded that deposited ITO films are good enough to use in applications like flexible optical solar reflector.

CHAPTER 4

SPACE ENVIRONMENTAL STABILITY OF ITO THIN FILMS COATED ON FEP AND KAPTON® SUBSTRATES

In this Chapter, stability of ITO coatings on different flexible substrates such as FEP, Kapton® and aluminized Kapton® substrates in simulated space environmental is discussed. The importance of surface modification of FEP substrate before ITO deposition in order to withstand the harsh environmental conditions in space is also discussed in this Chapter.

4.1 Introduction

Stability of ITO coating on flexible substrates in space environments is a major concern (Czeremuszkin et al., 2001; Gilmore, 2002). It has been reported that, achieving good adhesion of ITO thin film on flexible substrates is a difficult task; the sheet resistance of ITO coating on these substrate is likely to increase in space environment due to the delamination of ITO film from the substrate (Fahlteich et al., 2017; Goldstein et al., 1982). Delamination of ITO coating on these polymers can seriously damage the spacecraft. Therefore, it is important to examine the stability of ITO coated FEP and Kapton® substrates in simulated space environments and at the prelaunch conditions. In this Chapter evaluation of sheet resistance and thermo-optical properties of ITO coated FEP, Kapton® and aluminized Kapton® substrates before and after environmental tests has been discussed. Environmental tests such as relative humidity (RH), thermo-cycling (TC) and thermo-vacuum (TVAC) were performed in simulated space environments. Moreover, a simple RF plasma etching process has been done to improve the adhesion of ITO coating on FEP substrate. Plasma etching of FEP was carried out in argon plasma prior to the ITO deposition. The morphological and interfacial changes of plasma etched FEP substrates have been investigated, which showed that RF plasma etching is more suitable to increase the roughness and adhesion

of FEP substrates without altering its thermo-optical properties. The stability and adhesion of ITO coatings on the plasma etched FEP substrate in simulated space conditions are also studied in detail.

4.2. Experimental procedure

ITO thin films are deposited on flexible FEP, Kapton® and aluminized Kapton® substrates using the optimized deposition parameters as discussed in Chapter 2. Table 4.1 summarizes the optimized experimental parameters for the ITO film that satisfies the thermo-optical and sheet resistance values for the spacecraft applications. Dupont^{TM} Teflon® FEP (type A, ~125 µm thickness), plain Kapton® and aluminized Kapton® (thickness ~50 µm) of size 4 cm X 4 cm were used as the substrates. FEP and plain Kapton® substrates were ultrasonically cleaned in isopropyl alcohol for 2 min and dried with high purity nitrogen flush before placing into the vacuum chamber. The aluminized Kapton® substrates were not cleaned in any chemicals and they were loaded into the vacuum chamber as it is after nitrogen flushing. ITO was deposited on the opposite side of aluminium coated side of Kapton® substrate. Some ITO depositions were done on the plasma etched FEP substrate. Plasma etching process of FEP substrate was described in section 2.3 of the Chapter 2. FEP substrate was cleaned before the etching process, samples were loaded into the deposition chamber immediately after the etching process without any further cleaning.

Table 4.1: Optimized experimental parameters for ITO coating on flexible substrates.

Target material	In : Sn (90 % :10 % wt.)
Target size	75 mm diameter × 6 mm thickness
Distance between substrate and target	0.052 m
Ultimate vacuum	$<7.0 \times 10^{-6}$ mbar
Operational pressure	$\sim 5.8 \times 10^{-2}$ mbar
Argon flow rate	11.5 sccm
Oxygen flow rate	2.0 sccm
Substrate temperature	140°C
Target power	60 W pulsed DC
Target cleaning	1 min
Thickness of ITO film	~15 nm

The environmental stability of ITO coating on FEP and Kapton® substrates was studied in simulated space environment conditions as described in section 2.5.11 of Chapter 2. Relative humidity test was conducted on ITO coated FEP, Kapton® and aluminized Kapton® substrates to study the stability of ITO coating in high humidity and temperature at prelaunch conditions. Thermal-cycling (TC) test was performed to study the effect of cycling temperature on the ITO coated FEP, Kapton® and aluminized Kapton® substrates. To study the performance of ITO coated FEP, Kapton® and aluminized Kapton® substrates in space environments thermo-vacuum (TVAC) test was performed in a vacuum chamber which is in space environment condition such as high vacuum and extreme temperatures.

4.3 Results and discussion

From Chapter 3 it is found that, ITO deposition parameters such as oxygen flow rate, substrate temperature, target power and thicknesses of coating, etc. have to be optimized properly to acquire desired thermo-optical, sheet resistance values needed for spacecraft applications. 10-15 nm thick ITO films gives desired thermo-optical and sheet resistance values for the spacecraft applications. Therefore, 15 nm ITO coating was deposited on flexible FEP, Kapton® and aluminized Kapton® substrates for the environmental studies.

4.3.1 Optimized ITO thin films on FEP, Kapton® and aluminized Kapton® substrates

After optimizing the ITO thin films for the FOSR applications, ~15 nm thick of ITO thin film were deposited on FEP, Kapton® and aluminized Kapton® substrates and measured the transmittance, sheet resistance and IR emittance properties. ITO coated FEP and Kapton® substrates showed moderate sheet resistance, which is required for the space applications. Apart from achieving required sheet resistance, 15 nm thick ITO thin films on these substrates do not affect any of the other intrinsic properties, such as solar transmittance, IR emittance and solar reflectance of the substrates.
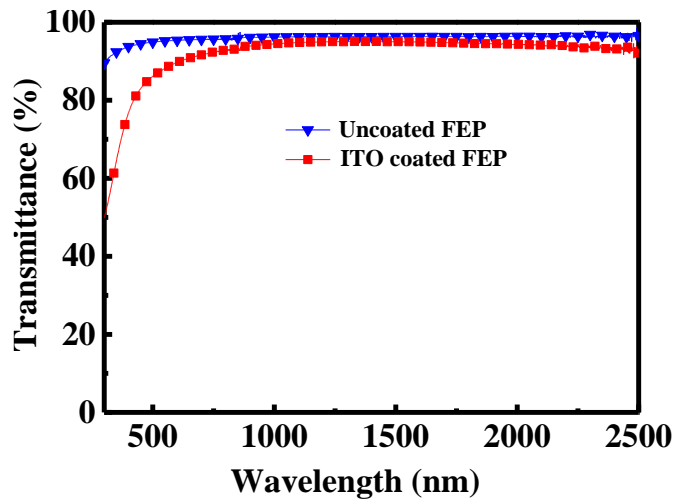
Figure 4.1: Solar transmittance spectra of uncoated and ITO coated FEP substrates.

The FEP substrate deposited with ITO coating (15 nm thick) showed sheet resistance in the range of 2-4 kΩ/sq. with an average solar transmittance of ~92%. Figure 4.1 shows the solar transmittance spectra of an uncoated and ITO coated FEP substrates. Only a small decrease in the visible region transmittance of the solar spectrum was noticed for ITO coated FEP substrate from the transmittance of uncoated FEP substrate. IR emittance was found to be 79% for ITO coated FEP substrate, which is also near to that of uncoated FEP substrate (ε = 80%). Figure 4.2 shows the transmittance spectra of uncoated and ITO coated Kapton® substrates. From the figure it can be seen that there was no change in the transmittance spectra of the uncoated and ITO coated Kapton® samples. The average transmittance values of uncoated Kapton® and ITO coated Kapton® were ~75% and ~73%, respectively. The sheet resistance was in the range of 2-4 kΩ for ITO coated Kapton® substrate. IR emittance was found to be 71% for the ITO coated Kapton® substrate, whereas, for uncoated Kapton® it was 72%. Aluminized Kapton® also showed no difference in its optical properties after ITO coating. The average reflection values of uncoated and ITO coated aluminized Kapton® were ~73% and ~72%, respectively. Figure 4.3 shows the reflection spectra of uncoated and ITO coated aluminized Kapton® substrates. Moderate sheet resistance in the range of 2-4 kΩ/sq. was achieved for ITO coated aluminized Kapton® substrates. The IR emittance of uncoated aluminized Kapton® did not change upon the deposition of ITO

film on that. Table 4.2 summarizes the electrical and optical properties of the uncoated and ITO coated FEP, Kapton® and aluminized Kapton® substrates.
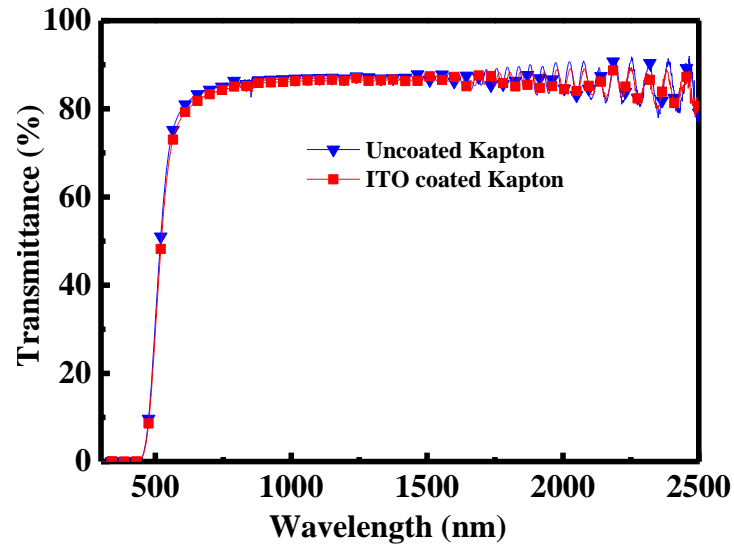
Figure 4.2: Solar transmittance spectra of uncoated and ITO coated Kapton® substrates.
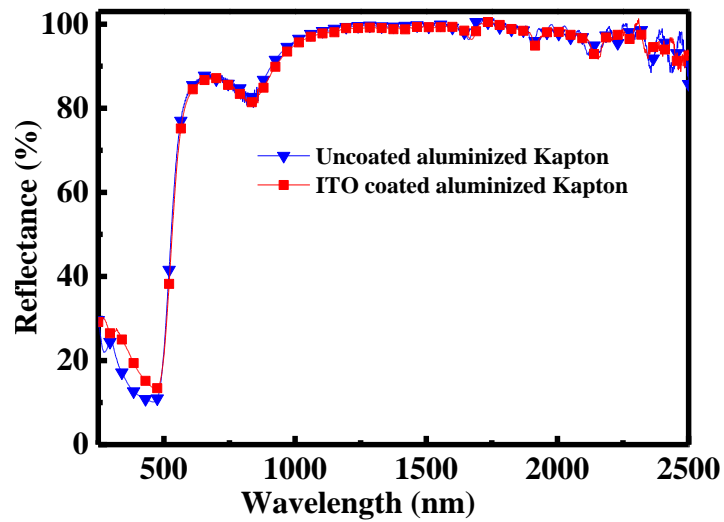
Figure 4.3: Solar reflectance spectra of uncoated and ITO coated aluminized Kapton® substrates.
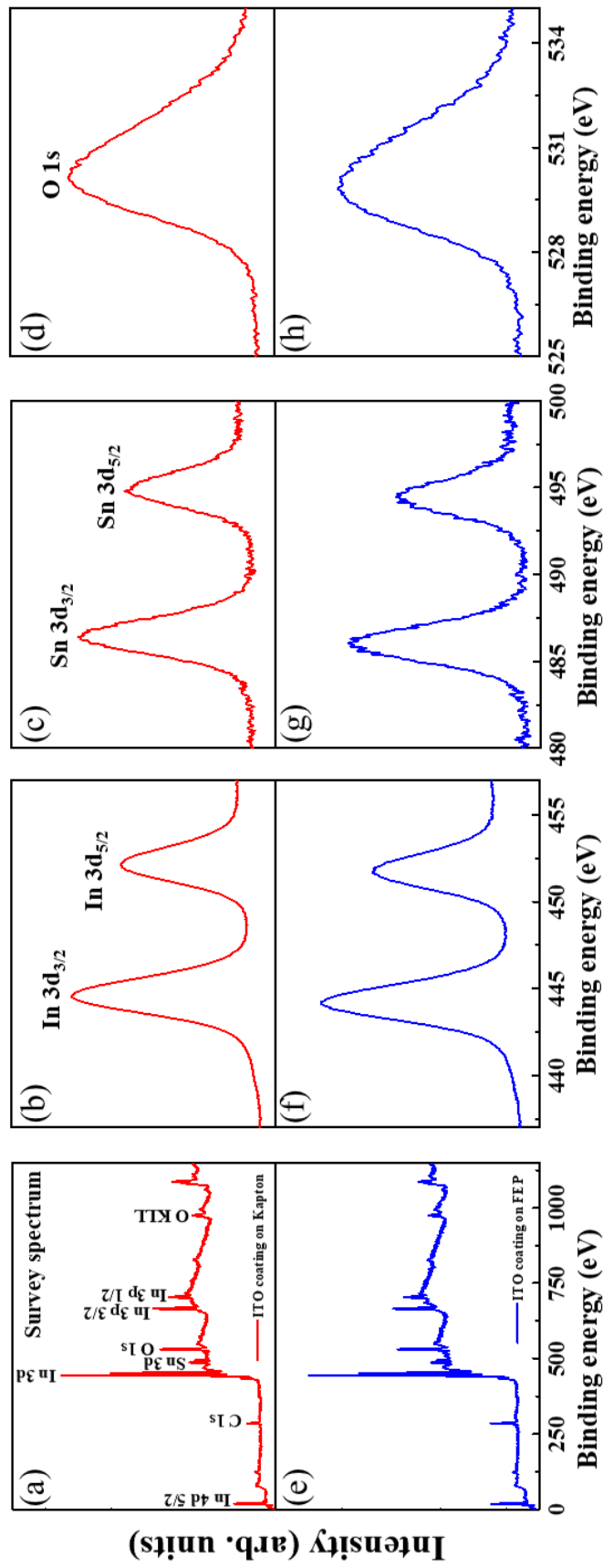
Figures 4.4: (a-d) and (e-g) show the XPS survey spectra, and core level spectra of In 3d, Sn 3d and O 1s of ITO coating on Kapton® and FEP substrates.

Table 4.2: Optical and electrical properties of uncoated and ITO coated FEP, Kapton® and aluminized Kapton® substrates.

Measurements	FEP		Kapton®		Al. Kapton®	
	Uncoated	ITO coated	Uncoated	ITO coated	Uncoated	ITO coated
Sheet resistance	$>10^6$ Ω/sq.	2-4 kΩ/sq.	$>10^6$ Ω/sq.	2-4 kΩ/sq.	$>10^6$ Ω/sq.	2-4 kΩ/sq.
T$_{av.}$	~96%	~92%	~75%	~73%	--	--
R$_{av.}$	--	--	--	--	~73%	~72%
IR emittance	~80%	~79%	~72%	~71%	~68%	~68%

No warpage or deformation of FEP and Kapton® substrates occurred during the ITO deposition. They were identical in appearance except having low sheet resistance for the ITO coated substrates. XPS survey scan was taken to study the chemical structure of ITO coating on FEP and Kapton® substrates which showed similar In, Sn, and O peaks for both ITO coated FEP and Kapton® substrates. Figures 4.4 (a-d) show the survey spectrum, and indium, tin and oxygen core level XPS spectra of ITO coated Kapton® substrate. Figures 4.4 (e-h) show the survey spectrum, and indium, tin and oxygen core level spectra of ITO coated FEP substrate.

4.3.2 ITO film adhesion test

Tape peel off test was performed to find out the adhesion of ITO films on the FEP, Kapton® and aluminized Kapton® substrates as per the ASTM D3359 standard (ASTM-D3359-97, 2007). There was no peeling off of the ITO coating from FEP and Kapton® substrates during the test. Table 4.3 shows the optical and electrical properties of ITO coated FEP and Kapton® substrates before and after adhesion test. From the table it can be observed that optical and electrical properties of ITO coating on FEP, Kapton® and aluminized Kapton® did not change significantly even after the adhesion test. The change in sheet resistance, ΔR_s was <100 Ω/sq. after the adhesion test for all

the coated samples. Moreover, all the optical and electrical properties were found to be in the required range for spacecraft applications.

Table 4.3: Optical and electrical properties of ITO coated FEP, Kapton® and aluminized Kapton® before and after adhesion test. Values indicated in brackets are before adhesion test.

Measurements	FEP	Kapton®	Aluminized Kapton®
Sheet resistance (kΩ/sq.)	2.7 (2.8)	2.6 (2.7)	2.6 (2.7)
$T_{av.}$ (%)	92 (92)	73 (73)	--
$R_{av.}$ (%)	--	--	73 (73)
IR emittance (%)	79 (80)	72 (72)	68 (68)

4.3.3 Environmental tests

Further, the space worthiness of ITO coated FEP, Kapton® and aluminized Kapton® samples were tested by relative humidity, thermal cycling and thermo-vacuum tests. After the environmental tests transmittance, sheet resistance and IR emittance properties were re-tested to confirm the stability of ITO coating on these substrates (results shown in Table 4.4). It is clear from Table 4.4 that even after environmental tests the sheet resistance, IR emittance and transmittance of uncoated and ITO coated aluminized Kapton® substrates did not change significantly. These results show that sputtered ITO films on Kapton® and aluminized Kapton® substrates are stable even in extreme environmental conditions encountered in space. Even though, the solar transmittance and the IR emittance of ITO coated FEP substrate did not change after the environmental tests, the sheet resistance increased to $>10^6$ kΩ/square after the TC and TVAC tests.

Table 4.4: Optical and electrical properties of ITO coated FEP, Kapton® and aluminized Kapton® substrates after environmental tests. The values in brackets represent properties before test.

Environmental tests	Sheet resistance (kΩ/sq.)			IR emittance (%)			T$_{av.}$ (%)		R$_{av.}$ (%)
	Kapton®	Aluminized Kapton®	FEP	Kapton®	Aluminized Kapton®	FEP	Kapton®	FEP	Aluminized Kapton®
RH	3.5 (2.7)	2.8 (2.3)	12 (2.0)	70 (70)	69 (69)	79 (79)	73 (73)	92 (92)	72 (72)
TC	3.4 (3.1)	2.5 (2.7)	>10^6 (2.0)	71 (71)	69 (69)	79 (79)	73 (73)	91 (92)	72 (73)
TVAC	3.4 (3.6)	2.4 (2.0)	>10^6 (2.6)	70 (70)	69 (69)	79 (79)	73 (73)	92 (92)	72 (72)

4.3.4 Failure analysis of ITO on FEP substrate

To understand the cause of increase in the sheet resistance of ITO coated FEP substrate after the environmental tests, the FESEM images of the samples after the tests have been taken. Figures 4.5 (a-c) show FESEM micrographs of as-deposited, TC treated and TVAC treated ITO coated FEP substrates, respectively. From the figure it can be observed that after the TC and TVAC tests some delamination happened to the ITO coating on the FEP substrate. This may be the reason for increasing the sheet resistance of ITO coating after the environmental tests. It indicated that adhesion of ITO thin film on the FEP substrates is needed to improve to withstand in the extreme environmental conditions in space.
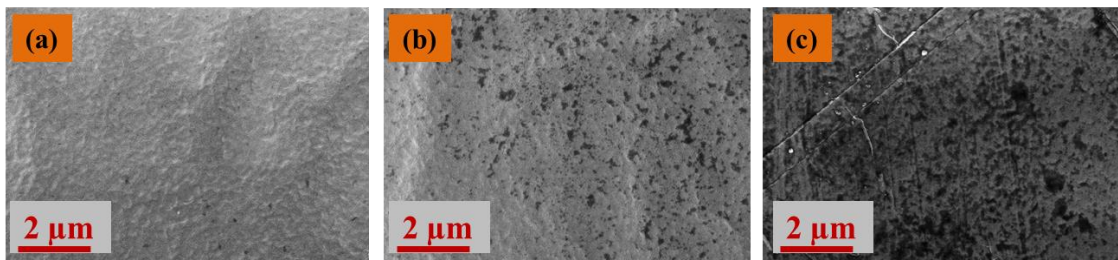
Figure 4.5: FESEM images of ITO coated FEP substrate: (a) as-deposited (b) after relative humidity test (c) after thermal cycling test.

4.3.5 Plasma etching of FEP substrate

In the literature it has been reported that the adhesion of thin films on fluoropolymer substrates can be improved by defluorination and making roughness on the surface by plasma treatments (Dasilva et al., 2012; Parekh et al., 2007; Wheeler and Pepper, 1983). Parekh et al. have reported that vacuum DC arc plasma treatment of FEP substrate showed defluorination and oxidation of FEP surface, which improved the adhesion of sputter coated Cu thin films on the FEP substrate (Parekh et al., 2007). Therefore, FEP substrate was plasma etched in Ar plasma prior to the ITO deposition. Only one side of the FEP substrate was treated with the plasma (see Figure 2.2 (b)). The plasma treatment time was varied to obtain optimum etching time, and it is found to be 6 min (see Figure 4.6(a)). Therefore, 6 min etched FEP substrates were used for further studies. Figures 4.6(b) and (c) show the FESEM images of untreated and etched FEP substrates, respectively. It can be observed from the FESEM images that the untreated FEP exhibited a smooth surface morphology but etched FEP substrate exhibited a rougher and a porous microstructure. The surface roughness values of the untreated and etched FEP substrates were obtained from AFM images which are shown in Figures 4.6(d) and (e), respectively. The average roughness (R_a) increased to 40 nm for the plasma etched FEP substrate from R_a ~ 5.3 nm of the untreated FEP substrate.

Untreated and etched FEP substrates were analysed by XPS to study the chemical changes after the etching process. XPS survey scan was carried out in the range of 0 to 1150 eV. XPS analysis showed prominent carbon, fluorine and oxygen elemental peaks in the survey spectra (see Figures 4.7 (a) and (b)). It may be noted that in the chemical structure of FEP substrate no oxygen is present but the XPS revealed presence of a small percentage of oxygen on the FEP surface. Similar kind of oxygen presence in the FEP substrate is also reported in the literature (Dasilva et al., 2006; Parekh et al., 2007). From the XPS spectra, peak intensity ratios of fluorine to carbon and oxygen to carbon were calculated for the untreated and etched FEP substrates and the same is given in Table 4.5. It can be seen from Table 4.5 that fluorine to carbon ratio of FEP substrate reduced after the plasma etching, which shows defluorination of the etched sample after the etching.
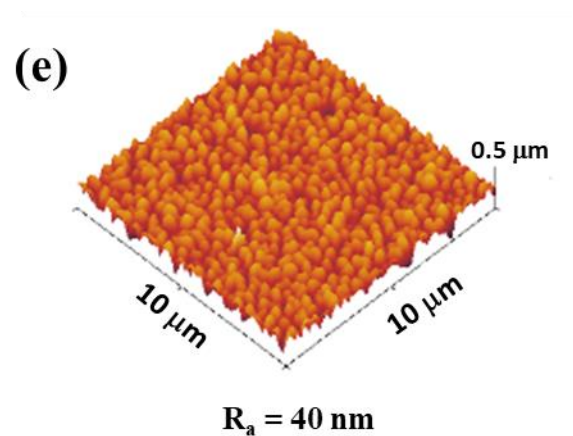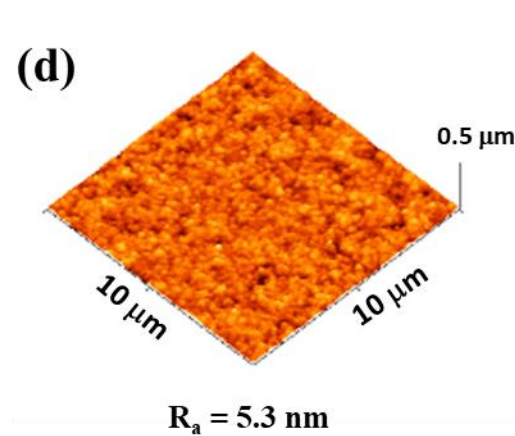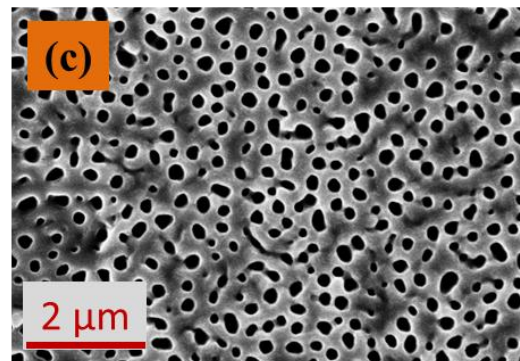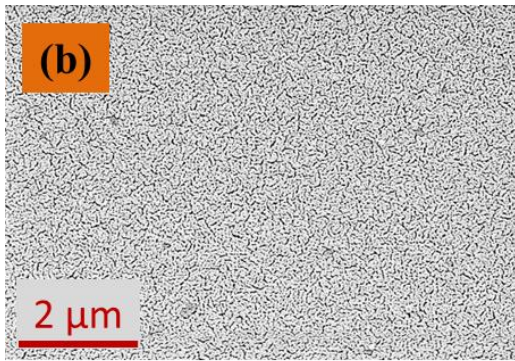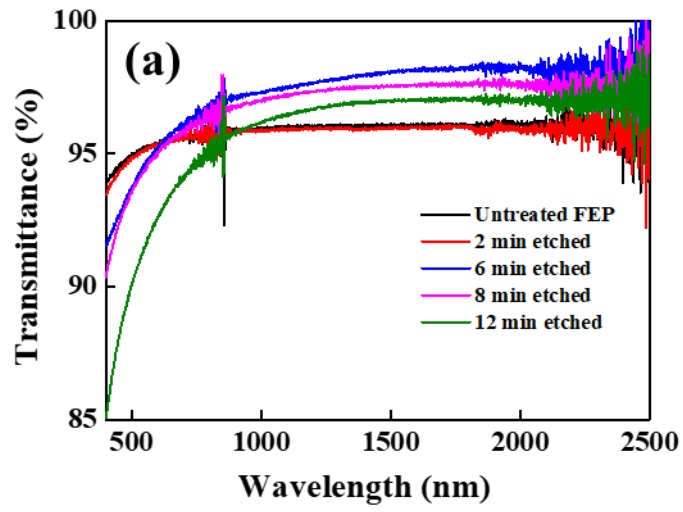
Figure 4.6: (a) Transmittance spectra of plasma etched FEP substrate for different durations. (b) and (c) show FESEM images, (d) and (e) show AFM images of the untreated and 6 min plasma etched FEP substrates, respectively.
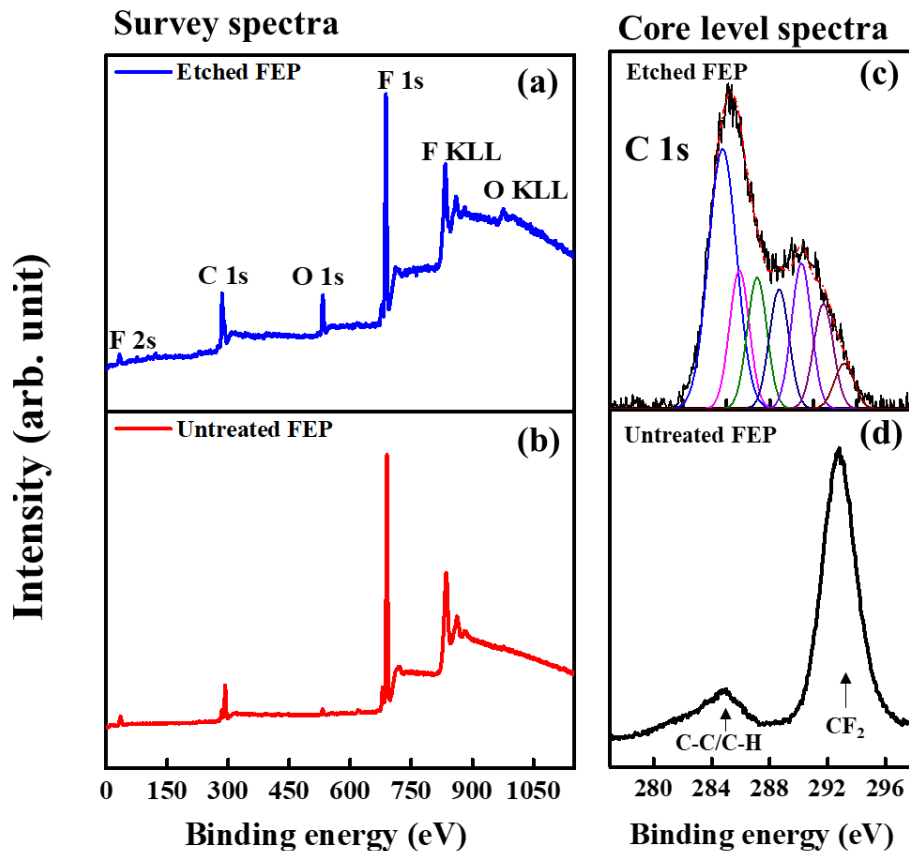
Figure 4.7: (a) and (b) XPS survey spectra and (c) and (d) C1s core level spectra of plasma etched and untreated FEP substrates.

The decreased fluorine to carbon ratio also demonstrates higher cross-linking on FEP surface (Agraharam et al., 1999). It has been reported that cross-linking can occur on a polymer surface that is treated with Ar or He noble gases plasmas (Mittal and Pizzi, 1999). The fluorine atoms escape during the plasma treatment, resulting in active sites in the polymer chain, and these active sites themselves make cross-linked bonds (Wheeler and Pepper, 1983). Cross-linked surface of the polymer substrate can increase the adhesion of coating by forming an effective covalent bond in interface between modified polymer surface and the over layer coating, as shown below Figure 4.8 (Mittal and Pizzi, 1999).
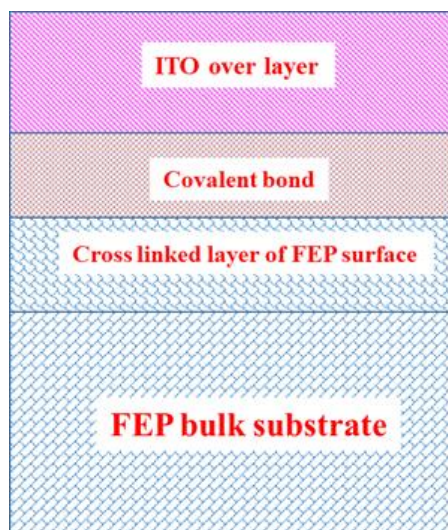
Figure 4.8: Schematic representation of interface structure between ITO film and the plasma etched FEP substrate (Mittal and Pizzi, 1999).

Table 4.5: Fluorine and oxygen intensities of untreated and etched FEP substrates.

	F/C	O/C
Untreated FEP	6.03	0.62
Etched FEP	3.20	0.91

Analysis of C1s peaks of the untreated and etched FEP substrates also gives the evidence of defluorination from the FEP surface. Figures 4.7 (c) and (d) show the C1s peaks of etched and untreated FEP substrates. The untreated FEP shows a major peak which corresponds to CF_2 bond near ~292.0 eV binding energy, implying that the most carbon atoms are bonded with two fluorine atoms (Busscher et al., 1992). But after etching, the major CF_2 peak disappeared and many lower binding energy peaks started appearing. The low biding energy peaks are reported to be associated with carbon atom bonded with less than two fluorine atoms and also from other diverse chemical bonds such as C-C, C-O, C-H and carbon atoms at cross-link sites (Busscher et al., 1992; Dasilva et al., 2012; Parekh et al., 2007). Therefore, it can be concluded that fluorine atoms have been removed from the FEP surface and cross-linked interface has been formed after plasma etching. Furthermore, the increased oxygen to carbon ratio for the etched FEP substrate shows improved surface energy of FEP surface (Busscher et al., 1992; Gupta et al., 2013). It has been reported in the literature that the higher surface

energy of FEP substrate is responsible for the good wettability and adhesion of coatings on the FEP substrate (Gupta et al., 2013; Parekh et al., 2007; Wheeler and Pepper, 1983).

From the solar spectrum transmittance graphs of the etched FEP substrates it can be observed that the transmittance in NIR region of the FEP substrate increased for the etched FEP substrate; at the same time the transmittance in the visible region (i.e., $\lambda < 750$ nm) reduced slightly (see Figure 4.9). However, the average transmittance of the etched FEP for the whole solar spectrum is almost same as the average transmittance of untreated FEP substrate (i.e, $T_{av} \sim 96\%$).
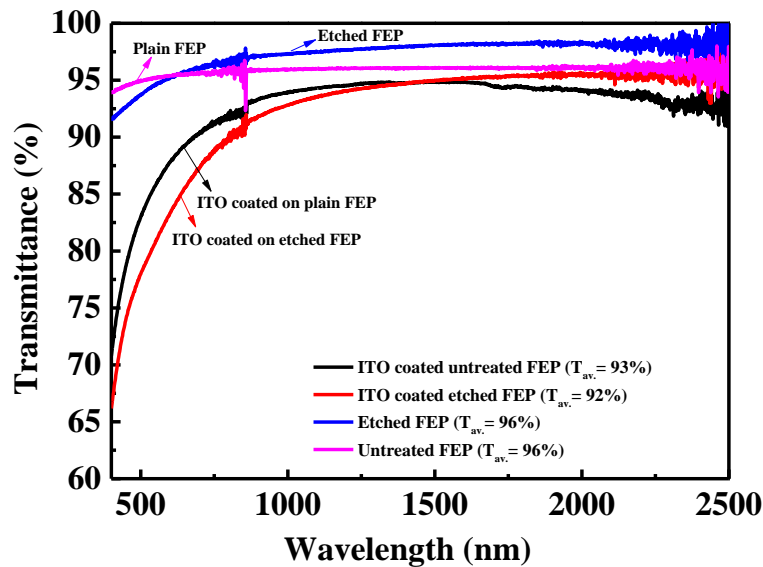
Figure 4.9: Solar transmittance spectra of uncoated and ITO coated untreated and etched FEP substrates.

4.3.6 ITO thin film on plasma etched FEP substrate

ITO thin films were deposited on the etched surface of FEP substrate, which showed $T_{av} > 90\%$. From Figure 4.9 it can be observed that as compared to the transmittance of ITO film deposited on untreated FEP substrate, ITO thin film coated on etched FEP substrate exhibited improved transmittance in the NIR region, but the visible region transmittance decreased slightly. However, the average transmittance values for ITO coatings on both the untreated and etched FEP substrates were almost

74

similar. Interestingly, the sheet resistance of ITO coating on etched FEP substrate was also in the range of 2-4 kΩ/sq. The ITO coating on etched FEP substrate showed IR emittance of 80%. Therefore, it can be concluded that the substrate etching did not affect any of the optical, electrical and thermal properties of ITO coating, and all were in the required range needed for the space application.

4.3.7 Adhesion test of ITO coated etched FEP substrate

Tape peel off test was carried out to find out the adhesion of ITO coating on etched FEP substrate. No significant changes in the optical, electrical and thermal properties were observed after the adhesion test. Table 4.6 shows the optical, electrical and IR emittance properties of ITO coated on etched FEP substrate before and after adhesion test.

Table 4.6: Optical and electrical properties of ITO coated etched FEP substrate before and after adhesion test.

	ITO coated etched FEP substrate	
	Before test	After test
Sheet resistance (kΩ/sq.)	3.1	3.2
$T_{av.}$ (%)	92	92
IR emittance (%)	80	80

4.3.8 Environmental test results of ITO coated etched FEP substrate

ITO coated etched FEP substrates were subjected to RH, TC and TVAC environmental tests. Table 4.7 shows the sheet resistance, transmittance and IR emittance of ITO coated on etched FEP substrates before and after environmental tests. The results proved that ITO coated on etched FEP substrate is more stable in the extreme space conditions than the ITO coating on untreated FEP substrate. The sheet resistance after RH, TC and TVAC tests increased a little bit but it was in the range needed for the spacecraft applications (Reddy et al., 2013). Compared to the sheet resistance ($>10^6$ Ω) of TC and TVAC tested ITO coated on untreated FEP substrate, sheet resistance of ITO coated etched FEP substrates remained in the required range, i.e., 6.2 and 6.0 kΩ/sq. after TC and TVAC tests, respectively. Thermo-optical

properties of ITO coated etched FEP substrate also did not change after the environmental tests. Figure 4.10 shows the FESEM images of ITO thin films on etched FEP substrates, which proves no delamination or cracking of ITO thin film deposited on etched FEP substrate even after TC and TVAC tests. From these studies it can be concluded that the ITO thin films on etched FEP substrates have better adhesion and stability for the space environments; therefore these coatings can be used in real spacecraft.

Table 4.7: Optical and electrical properties of ITO coated etched FEP substrates before and after environmental tests. The values in brackets represent properties before tests.

Environmental tests	R_s (kΩ/sq.)	IR emittance (%)	$T_{av.}$ (%)
RH	5.8 (3.2)	79 (80)	91 (91)
TC	6.2 (3.1)	81 (80)	91 (90)
TVAC	6.0 (3.1)	80 (80)	88 (90)
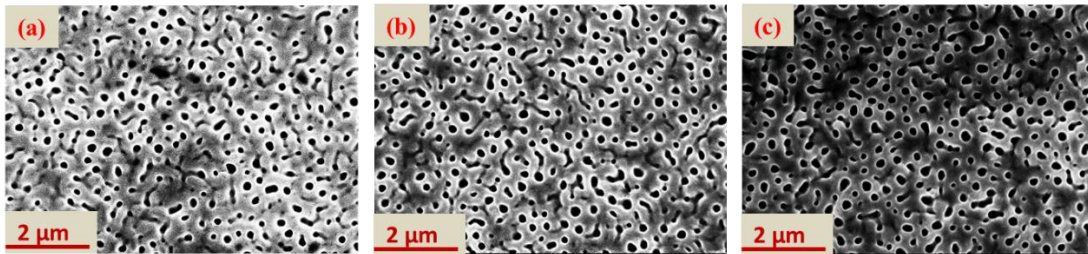
Figure 4.10: FESEM images of ITO coating on plasma etched FEP substrates: (a) as-deposited (b) after thermal cycling and (c) after thermo-vacuum tests.

4.4 Summary

ITO films of ~15 nm thicknesses were deposited on FEP, Kapton® and aluminized Kapton® substrates. ITO deposited FEP substrate showed $T_{av.}$ ~ 92% and IR emittance ~ 79% with sheet resistance of 2-4 kΩ/sq. ITO deposited Kapton® substrates showed average transmittance of ~ 74% and IR emittance of ~ 75% with sheet resistance of 2-4 kΩ/sq. ITO coated aluminized Kapton® exhibited IR emittance of ~ 68%, average reflectance of ~ 72% with sheet resistance of 2-4 kΩ/sq. RH, TC and TVAC tests of ITO coated FEP and Kapton® substrates showed that ITO coating on

Kapton® and aluminized Kapton® substrates were stable in these environments. Thermo-optical and sheet resistance of ITO coated plain and aluminized Kapton® substrates did not change even after these tests. However, the sheet resistance of ITO coating on untreated FEP substrate increased to $>10^6$ kΩ/sq. after TC and TVAC tests. The FEP substrate was etched in argon plasma to improve the ITO adhesion. XPS studies of FEP showed that after plasma treatment fluorine to carbon ratio decreased and oxygen to carbon ratio increased on the etched surface of FEP. Moreover, major carbon peaks shifted towards lower binding energy, which indicated defluorination and oxidation of the FEP surface after etching. FESEM and AFM images showed rough FEP surface after etching. It was found that ITO film on plasma etched FEP substrate exhibited very good stability in the space environment.

CHAPTER 5

DESIGN AND DEVELOPMENT OF ITO/Ag/ITO SPECTRAL BEAM SPLITTER COATING FOR PHOTOVOLTAIC-THERMOELECTRIC HYBRID SYSTEM

In this Chapter, deposition of a spectral beam splitter (i.e., ITO/Ag/ITO) which exhibits high transmittance and high reflectance in the visible and NIR/IR regions, respectively, is reported. In addition, the effects of ITO and Ag layer thicknesses on the visible transmittance, NIR/IR reflectance and also on the cut-off wavelength have been studied in detail. Further, a novel approach (i.e., chemical etching of glass substrate) is used to enhance the peak transmittance of ITO/Ag/ITO multilayer system.

5.1   Introduction

Transparent heat mirrors or solar spectrum beam splitters are widely used in numerous applications including hybrid photovoltaic-thermoelectric (PV-TEG) solar energy convertor, energy efficient windows, etc. High transmittance in the visible region and high reflectance in the NIR and IR region of the solar spectrum with optimum cut-off wavelength (~900 nm) are the critical parameters to be obtained for an efficient spectrum splitter coating. In this work ITO/Ag/ITO (IAI) based solar spectrum splitter has studied for hybrid PV-TEG solar energy convertor application. Figure 5.1 shows the schematic diagram of the IAI multilayer spectral beam splitter system which splits the visible and NIR regions separately for hybrid solar conversion. The sunlight coming through the concentrator falls on the multilayer filter coated on a glass substrate. The different components of hybrid solar conversion system are placed in such a way that the reflected rays of higher wavelength fall on the thermoelectric generator, and the transmitted visible light falls on the solar cell. The efficiency of the hybrid system will be the sum of the efficiency of thermoelectric generator and the solar cell. Therefore, high transmittance in the visible region and high reflectance in the NIR

and IR regions with an optimum cut-off wavelength is necessary to increase the total efficiency of the hybrid system. These peculiar optical properties are produced due to the antireflection from the interface of the films of high and low refractive index materials stacked alternatively (Al-Kuhaili et al., 2009; Granqvist, 1981; Lee et al., 1996).
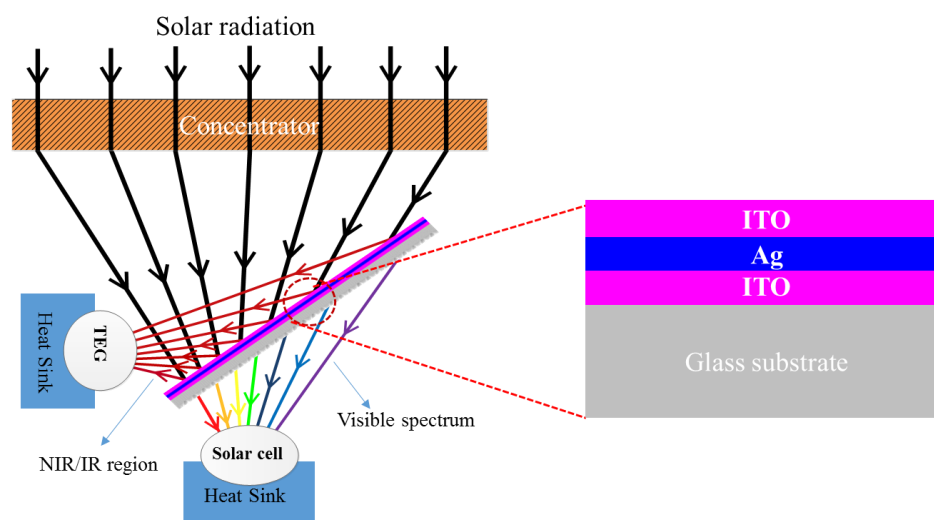
Figure 5.1. Schematic diagram of ITO/Ag/ITO spectral beam splitter coating.

5.2   Experimental details

IAI multilayer coatings were deposited by a DC balanced magnetron sputtering system as described in section 2.1.2 of Chapter 2. The top and bottom ITO layers were deposited on glass substrate using an In:Sn alloy target in argon flow rate of 11.5 sccm and oxygen flow rate of 2.0 sccm. All the ITO depositions were done at 60 W pulsed DC power. The middle Ag layer was deposited Ag target in argon flow rate of 20 sccm at a 5 W DC target power. Borosilicate glass slides (from Borosil) of dimension: 17 mm × 25 mm × 1.25 mm were used as the substrates. The glass substrates were cleaned by ultrasonication in isopropyl alcohol and acetone for 10 min each. Some of the glasses were one side etched to enhance the visible transmittance, the details of which are explained in section 2.4 of Chapter 2. Prior to the deposition, the chamber was evacuated down to a base pressure 7.0×10^{-6} mbar using a turbo molecular pump backed with a rotary pump. The growth rates of ITO and Ag films were 1 and 0.5 nm/s, respectively, which were calculated from the cross-sectional field emission scanning

electron microscopy images and profilometer studies. Hereafter, films with required thicknesses were deposited by varying the deposition time. All the three layers were deposited without breaking the vacuum in the chamber. No substrate heating was used while sputtering.

UV-Vis-NIR spectrophotometer was used for the solar spectrum transmittance, reflectance, angular reflection and optical haze measurements of the coatings. Transmittance and reflectance of single and multilayers were measured in the wavelength range of 250 to 2500 nm. Angular reflection was measured using the universal reflectance accessory at varying angles. Haze measurements were done as per the ASTM 1003 standard in the wavelength range 380 nm to 780 nm. FTIR transmittance was measured using PerkinElmer Frontier FTIR spectrometer. Atomic force microscopy was used to find out the roughness of plain and etched glass substrate.

5.3   Results and discussion

5.3.1   Design of ITO/Ag/ITO multilayer spectral beam splitter coating

The genesis of selecting IAI as the spectral beam splitter has been corroborated by the reported admittance data of Ag and ITO (Hong et al., 2011; Kostlin et al., 1982; Kusano et al., 1986; Lee et al., 1996). From the admittance diagram technique, it is known that a highly reflecting metal film sandwiched between two high refractive index materials like ITO ($n_{ITO} \sim 2$) will show a high antireflection effect in the visible range with very high visible transmittance (Kostlin and Frank, 1982).

Figures 5.2(a) and (b) show the transmittance and reflectance spectra, respectively of single and multilayer structure of Ag and ITO on a glass substrate. From the figure, it can be seen that thin Ag layer (thickness ~ 21 nm) has a very narrow transmission band with a maximum transmittance of 70% at 364 nm. At higher wavelengths, the transmittance falls and reaches a minimum value, while the reflection reaches to a maximum value. The transmittance and reflectance spectra of a 40 nm thick ITO coating on glass slide are also shown in Figures 5.2(a) and (b). ITO layer shows high transmittance and low reflection in the solar spectrum. For a double layer structure of ITO/Ag (Ag on the top of ITO) on the glass substrate, the transmittance and reflectance spectra are more identical to the spectral behavior of thin Ag layer. The

transmittance has narrowed in the visible region, and the NIR reflection increases. According to admittance diagram technique, the zero-reflection condition can be achieved only when there is no discontinuity in the admittance path from substrate to air (Kostlin and Frank, 1982). However, by completing the admittance path by depositing the final ITO layer on the Ag film, it can be clearly seen the antireflection effect in the visible region. The reflectance in the visible region of ITO/Ag/ITO coated on glass substrate reached to almost zero-reflection condition, this enhanced the transmittance of Ag while maintaining high reflection in the NIR region.
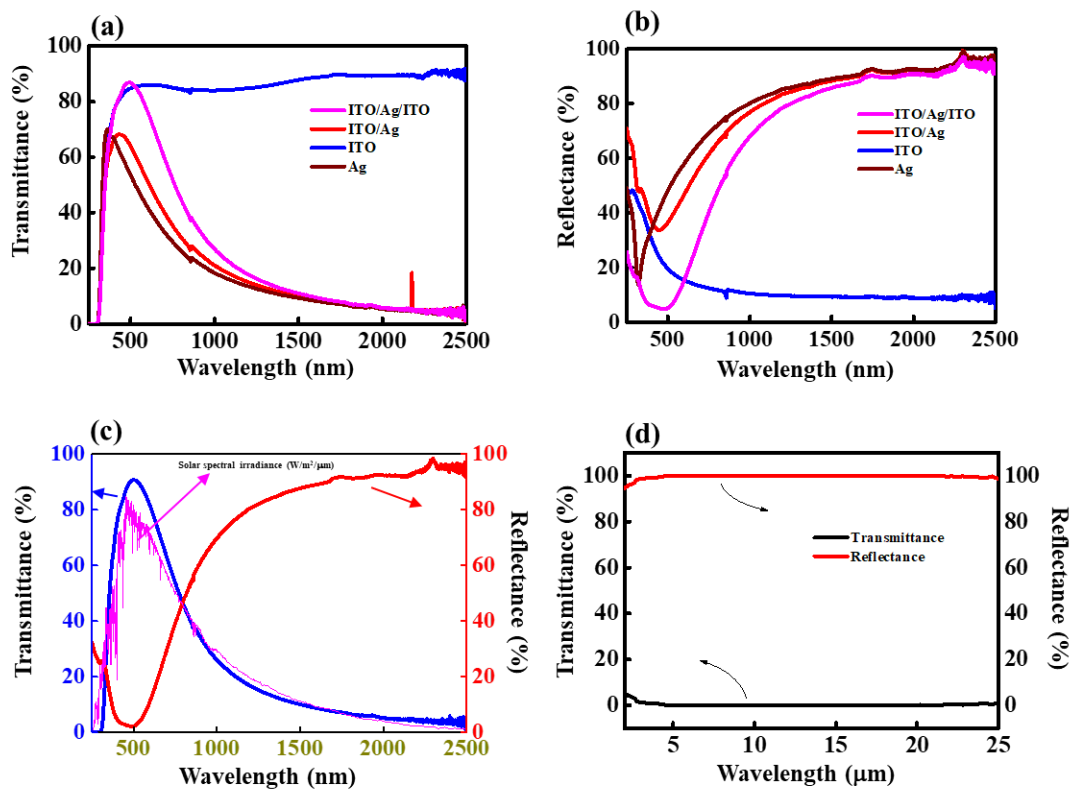
Figure 5.2: (a) Transmittance (b) reflectance spectra of single and multilayers of Ag and ITO on glass substrate. (c) Solar transmittance and reflectance spectra of IAI multilayer along with solar spectrum irradiance spectrum. (d) FTIR reflection and transmittance spectra of multilayer system.

The applications of band pass filter demand the region of the solar spectrum that to be transmitted should cover only the visible part, and NIR and IR regions should be reflected back completely. Figure 5.2(c) shows the transmittance and reflectance spectra of the optimized IAI multilayer. From the figure, it can be seen that sputter deposited IAI multilayer on glass substrate effectively filtered the visible region of the solar spectrum with a peak transmittance of 91% and NIR region reflectance was more than 90%. FTIR reflectance and transmittance spectra were taken and the data is presented in Figure 5.2(d), which show that IAI system completely reflects the IR radiation with very low transmittance. The ITO and Ag layer thicknesses play a major role in achieving the spectral beam splitting and also to attain the optimum cut-off wavelength, which is explained in detail below.

5.3.2 Effects of Ag and ITO layer thicknesses

Nanometer range difference in the thicknesses of ITO and Ag layers makes a significant change in the transmittance and reflectance spectra. In IAI multilayer system, thin Ag layer between ITO layers is mainly responsible for the reflectance of the IAI system (Lampert, 1981; Lee et al., 1996; Wang et al., 2006). By nature, Ag possesses very high reflectance in the NIR and IR regions due to the high free electron density (Lee et al., 1996; Wang et al., 2006). At the same time, Ag has the minimum absorption in the visible region of the solar spectrum (Lee et al., 1996). However, the absorption depends on the thickness of the Ag layer. For this reason, the thickness of Ag layer has to be minimum to enhance the transmission in the visible region. Figure 5.3 shows the effect of Ag thickness on the solar reflectance and transmittance spectra of IAI multilayer system. It is well known that at lower thicknesses, noble metals such as Au and Ag follow Volmer-Weber growth mode (i.e., island type morphology) (Wang et al., 2006). The island growth is not suitable for solar spectrum splitting applications (Al-Kuhaili et al., 2009; Lee et al., 2015). A continuous Ag film is required to get good selectivity and stability in the multilayer system (Lee et al., 1996; Wang et al., 2006). Lee et al. have reported that Ag thickness should be more than 15 nm to get required properties in an oxide/Ag/oxide multilayer system (Lee et al., 1996). So, in our

experiments, Ag layer thickness was varied from 15 to 27 nm while keeping the top and bottom ITO layers at a thickness of 40 nm.

From Figure 5.3(a), it can be seen that when the Ag layer thickness is lowest (i.e., 15 nm), the transmittance was high, and it covered a broad region of the solar spectrum, but the reflection was low for these coatings. While increasing the thickness of Ag layer, reflection increased, but it lowers the visible transmittance significantly, and the region of transmitted spectrum narrows down. Figure 5.3(b) gives a clear picture of the variation of maximum transmittance and shifting of peak wavelength with increasing Ag layer thickness. Theoretically, it is possible to increase the Ag layer thickness by maintaining the high transmittance till the tangents of ITO admittance curve and phase thickness of Ag film are orthogonal to each other in admittance diagram (Kostlin and Frank, 1982; Lee et al., 1996). From this study, it has been observed that increasing the thickness of Ag layer till 21 nm shows no significant change in the maximum transmittance (T_{max}). However, further increase in the thickness results in a considerable decrease in the maximum transmittance of IAI system. Also, when the Ag thickness increases the wavelength of maximum transmittance as well as cut-off wavelength shifted toward lower wavelength due to the effect of more Ag component. Figure 5.3(c) shows the change in the λ_c and the reflectance at 2000 nm wavelength with a variation of Ag layer thickness. As discussed earlier, the Ag film is mainly responsible for the high reflection in the NIR region. Therefore, when the Ag thickness increases in IAI multilayer system from 15 to 27 nm the NIR reflectance substantially increased from 82 to 94% at 2000 nm.
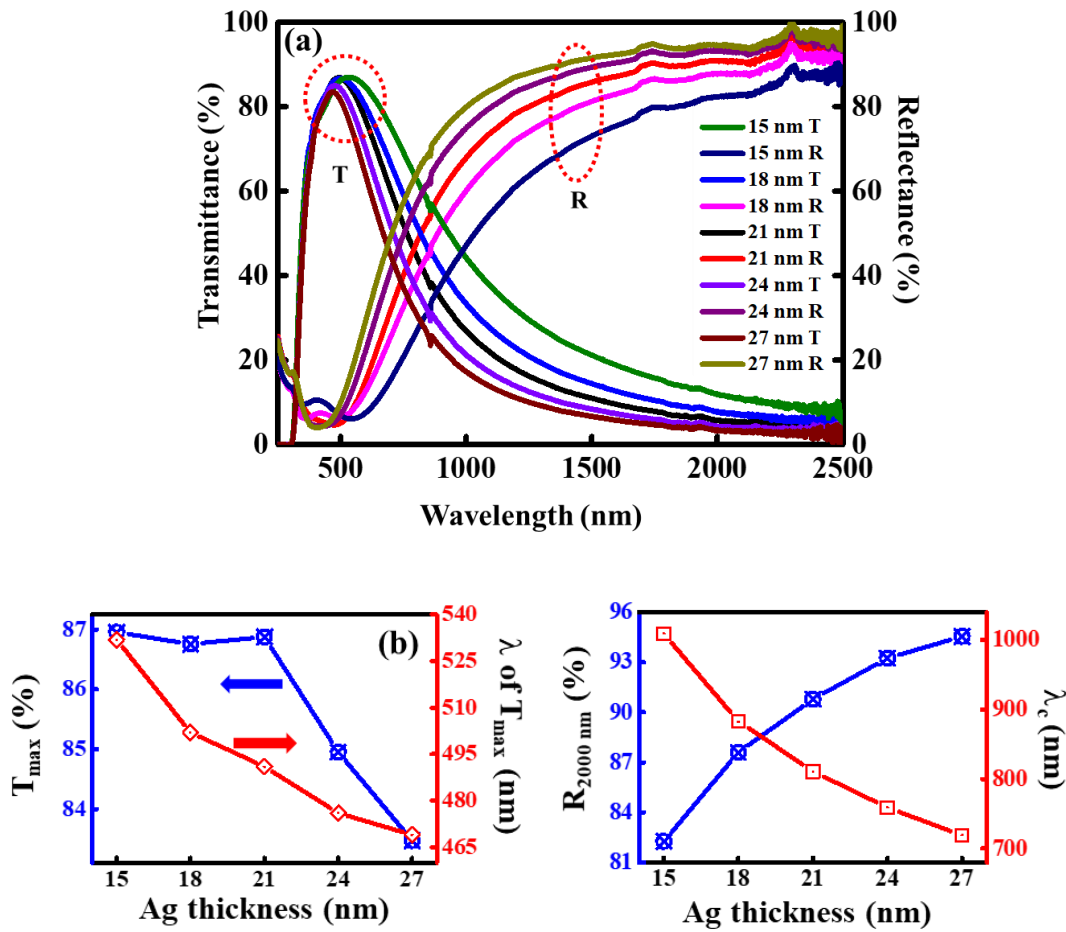
Figure 5.3 (a) Solar transmittance and reflectance (b) maximum transmittance (T_{max}) and wavelength of peak transmittance and (c) Reflectance at 2000 nm and cut off wavelength of IAI multilayer coating with different Ag layer thicknesses.

To study the effect of ITO thickness on the spectral selectivity of IAI multilayer, IAI multilayers on glass substrates with different thicknesses of ITO layer have been prepared, while keeping Ag thickness at 21 nm for all the samples. It has been reported that the top and bottom oxide layers should be of the same thicknesses to get the maximum transmittance in an oxide/metal/oxide spectrum beam splitter (Al-Kuhaili et al., 2009; Lee et al., 1996). Therefore, in the present work, the bottom and top ITO layers were kept at the same thickness. It has been reported that the maximum transmittance occurs when the phase thickness is $\delta = m\pi$, (where, m = 0,1,2,… and π -phase angle) (K. Hong et al., 2011). It is well known that the optical thickness and the

phase thicknesse of the film increase with an increase in the physical thickness of film. Therefore, while adjusting the thicknesses of ITO films, the maximum transmittance will be obtained at a particular thickness vlaue where the above condition is satisfied. The ITO layer thicknesses were varied from 30 to 70 nm. Figures 5.4(a) shows the reflectance and transmittance spectra of IAI multilayers for different thicknesses of ITO layers. From the figure it can be seen that ITO layer also plays a significant role in the spectrum selectivity, but it shows a reverse effect compared to Ag layer thickness. From Figure 5.4(b) it can be observed that T_{max} of IAI multilayer system increased with an increase of ITO layer thickness. The transmittance reached maximum to 88% at 523 nm for 60 nm thick ITO films.

Figure 5.4(c) shows the variations of reflectance and λ_c with ITO layer thickness. Reflectance was found to decrease with increasing ITO thickness. It has been observed that in the case of reflectance of IAI multilayer system, ITO has less significance compared to Ag layer thickness. Only ~1.4% decrease in the reflectance at wavelength 2000 nm was observed when the ITO layer thickness was changed from 30 to 70 nm as compared to ~12% difference when the Ag thickness was varied from 15 to 27 nm. This proves that the NIR and IR reflections of IAI multilayer mainly depend up on the Ag layer thickness. It has been observed that increasing the ITO thickness from 30 to 60 nm resulted in shifting the λ_c towards higher wavelength (772 to 896 nm). Beyond 60 nm a slight decrease in the λ_c was found. From these results it can be concluded that varying the thicknesses of Ag and ITO layers helps to get good selectivity of transmitted and reflected spectra and to confine the transmitted region exactly into the visible spectrum as shown in Figure 5.2(c). Moreover, λ_c can be achieved for the optimum power production (λ_c ~900 nm) of the hybrid PV/TEG conversion system.
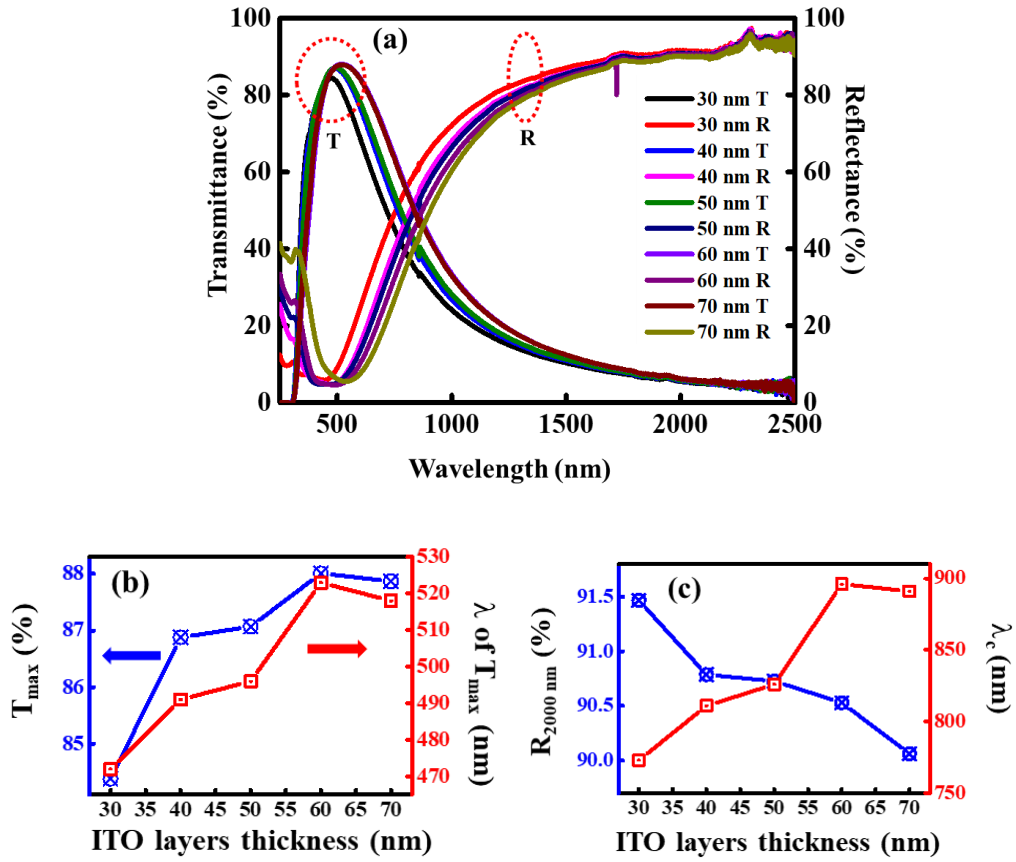
Figure 5.4. (a) Solar transmittance and reflectance (b) maximum transmittance (T_{max}) and wavelength of peak transmittance and (c) reflectance at 2000 nm and cut off wavelength of IAI multilayer coating with different ITO layers thicknesses.

The figure of merit of beam splitter is an important property for achieving high efficiency of the hybrid PV/TEG system. Durrani et al. have reported that the performance of a multilayer system can be evaluated by a figure of merit, Z-factor (Durrani et al., 2004);

$$Z = [\left(\frac{\int T_{Vis} d\lambda}{\int d\lambda}\right)_{VIS}][\left(\frac{\int R_{IR} d\lambda}{\int d\lambda}\right)_{IR}] \qquad (5.1)$$

where $\left(\frac{\int T_{Vis} d\lambda}{\int d\lambda}\right)_{VIS}$ is the integrated visible transmittance ($T_{av.}$) and it is calculated for a wavelength range of 400 to 700 nm. $\left(\frac{\int R_{NIR} d\lambda}{\int d\lambda}\right)_{NIR}$ is the integrated NIR reflectance ($R_{av.}$) which is measured over a wavelength range of 700 to 2500 nm.

An ideal spectrum beam splitter should possess highest Z-factor. But in practice, it is not possible to achieve, $T_{av.} = 1$ in visible region and $R_{av.} = 1$ in the infrared region at the same time. Hence, the Z-factor always will be less than 1. Figure 5.5(a) shows the $T_{av.}$ and $R_{av.}$ of IAI multilayers as a function of Ag layer thickness, while keeping the top and bottom ITO layers thicknesses at 40 nm. It can be seen from the figure that, at lower thicknesses of Ag layer, $T_{av.}$ was high and it decreased with increasing Ag thickness. Meanwhile, $R_{av.}$ increased with increasing Ag layer thickness. The Z-factor has been calculated for different thicknesses of Ag and the data is shown in the inset of Figure 5.5(a). From the figure, it is found that, when the Ag thickness is just around the critical thickness needed for a continuous Ag film, i.e., 15 nm, Z-factor is lowest. And with increasing Ag layer thicknes the Z-factor increases. The maximum Z-factor is achieved when the Ag layer thickness is around 21 nm. On further increasing the Ag layer thickness, the Z-factor decreased due to the low transmittance. Therefore, it can be concluded that best spectral selectivity for an IAI multilayer can be achieved when the Ag thickness is close to 21 nm.
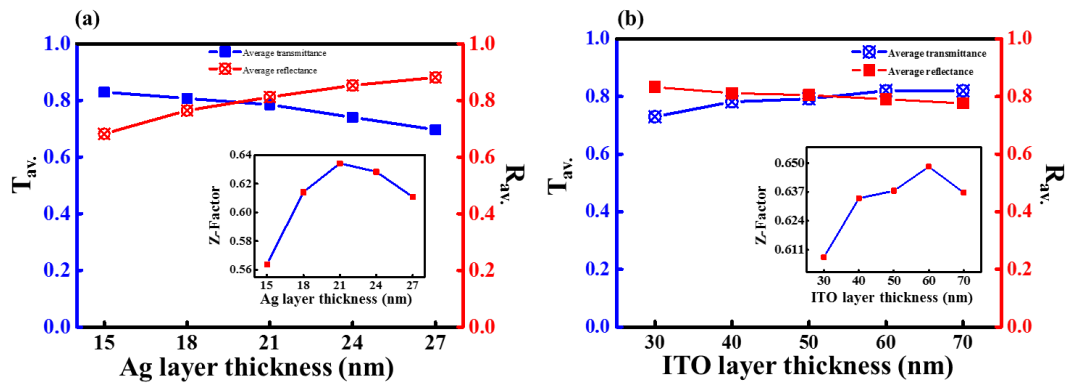
Figure 5.5: (a) Average solar transmittance and average NIR reflectance of IAI multilayer coating with different Ag layer thicknesses and (b) Average solar transmittance and average NIR reflectance of IAI multilayer coating with different ITO layer thicknesses. Z-factor of IAI multilayer coating for different Ag and ITO layer thicknesses are shown in the inset of figure (a) and (b), respectively.

Figure 5.5(b) shows the $T_{av.}$ and $R_{av.}$ of IAI multilayers as a function of ITO layer thickness while keeping Ag layer thickness at 21 nm. From the figure, it can be seen that when ITO layer thickness increases, the average visible transmittance

increases marginally as compared to Ag layer thickness. Meanwhile, average NIR reflectance decreases marginally with increasing the ITO layer thickness. The calculated Z-factor for varying ITO layer thickness is shown in the inset of Figure 5.5(b). The Z-factor increases with ITO thickness and reaches a maximum when the thickness is 60 nm, after that it starts decreasing. These results clearly show that the optimized thicknesses of Ag and ITO layers are 21 and 60 nm, respectively in order to get high visible transmittance and NIR reflectance.

5.3.3 Optical properties of IAI multilayers on one side etched glass substrate

Using the optimized Ag and ITO thicknesses, a maximum visible transmittance of 88% and a maximum NIR reflectance of 90% for $\lambda \geq 2000$ nm were achieved. In general, the transmittance of the glass substrate can be improved by using conventionally antireflection coatings (such as SiO_2, TiO_2), which increase the cost of multilayer coating (Camurlu et al., 2012; Deubener et al., 2009; Jin et al., 2003). In the present work, in order to improve the visible transmittance, a novel cost effective chemical etching method was used to etch the single side of the glass substrate. The FESEM image of one side etched glass substrate is displayed in Figure 5.6(a). It can be seen a nanoporous surface is formed on the glass substrate after etching which acts as an antireflecting layer due to the presence of air in the interstitial spaces. These nanopores, having tapering profile, provide a gradual change in refractive index, which results in antireflection effect (Kumar et al., 2016). Subsequently, the optimized IAI (60/21/60 nm) multilayer coating was deposited on single side etched glass substrate, which exhibits an average visible transmittance 93.7% (Figure 5.6(b)). Schematic representation of IAI multilayer coating on etched glass substrate is shown in Figure 5.6(c). Figure 5.6(d) shows the transmittance and reflection spectra of multilayer coating on a plain glass and one side etched glass. From the figure, it can be seen that the visible reflectance of the IAI multilayer has reached the minimum value for the etched glass when compared to the coating on the plain glass. So the decrease in the reflectance increased the transmittance. The T_{max} in visible region of the IAI multilayer coating increased to ~91% for the etched glass. It is to be noted that the results (i.e., high visible transmittance and high NIR-IR reflectance) obtained in the present study

are at par with the previously reported spectrally beam splitter coatings and a comparison is shown in Table 5.1. It is clearly evident from Table 5.1 that the highest visible transmittance obtained in the present study is slightly higher than the previously reported literature values. This was achieved by fabricating a nano-porous microstructure on one side and multilayer coating on other side of the plain glass.
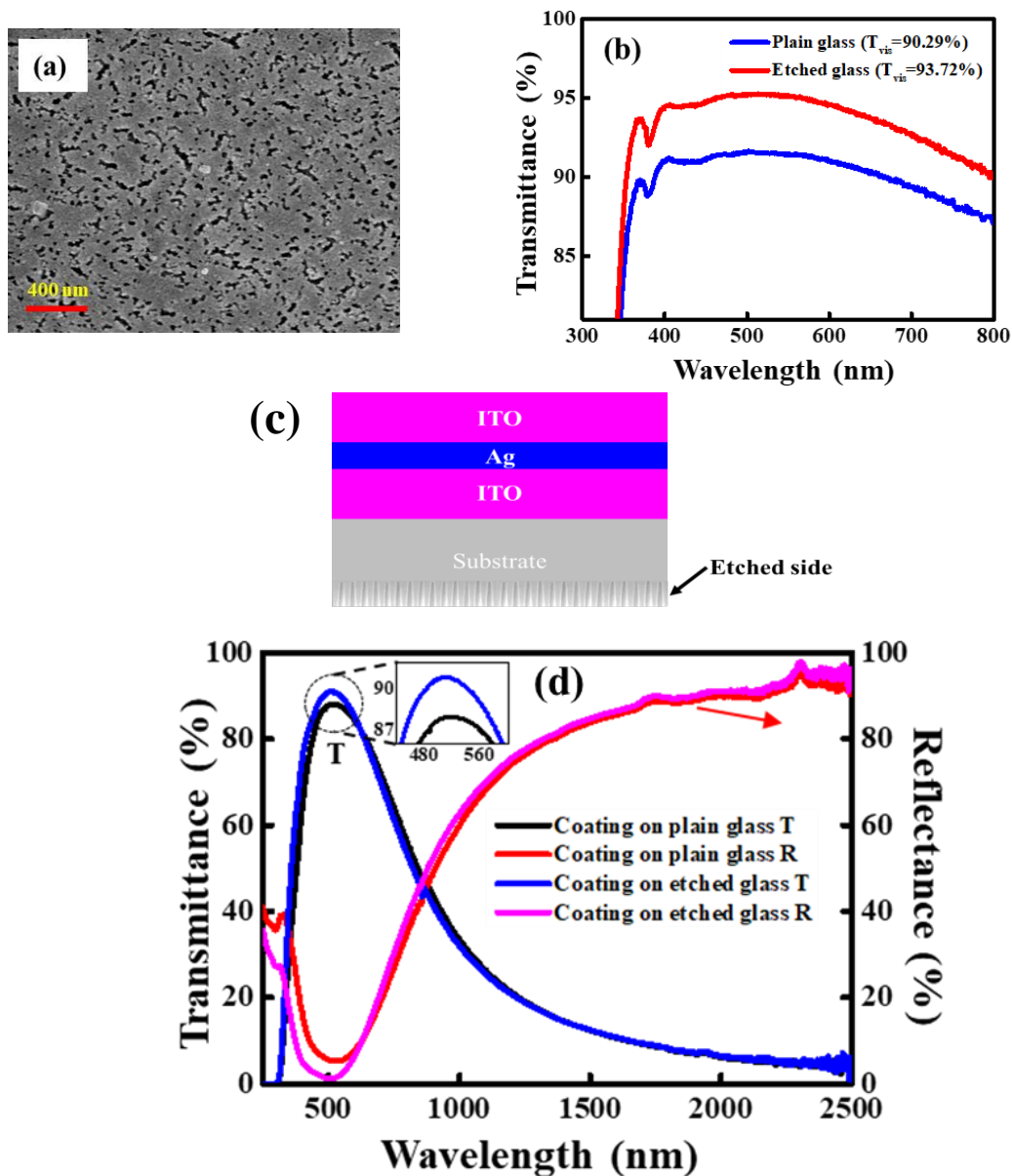
Figure 5.6: (a) FESEM micrograph of single side etched glass. (b) Visible transmittance of etched glass and plain glass substrates. (c) Schematic representation of IAI multilayer coating on etched glass substrate. (d) Solar transmittance and reflectance of IAI (60/21/60 nm) multilayer on plain glass and a single side etched glass substrate.

Table 5.1: Maximum transmittance and reflectance of different multilayer stacks reported in the literature.

S. No.	Multilayer stack	T_{max} in visible range (%)	Reflecion in NIR and IR regions (%)	Method of preparation	References
1	ITO/Ag/ITO	85	95 at 10 μm	Sputtering	Kusano et al., 1986
2	ITO/Ag/ITO	83	--	Sputtering	Bender et al., 1998
3	TiO$_2$/Ag/TiO$_2$	80	90 in NIR	Thermal evaporation	Wang et al., 2006
4	WO$_3$/Ag/WO$_3$	88.3	--	Thermal evaporation	Al-Kuhaili et al., 2009
5	ITO/Ag/ITO	86	--	Linear facing target sputtering (LFTS)	Jeong and Kim, 2009
6	ITO/TiO$_2$	85	75 in IR	Sputtering	Dobrikov et al., 2009
7	ITO/Ag/ITO	90[#]	--	Sputtering	Guillén and Herrero, 2009
8	WO$_3$/Au/WO$_3$	84	--	Thermal evaporation	Al-Kuhaili et al., 2012
9	ITO/Ag/ITO	85.3	--	Sputtering	Kim et al., 2015
10	TiO$_2$/Cu/TiO$_2$	90	85 at 1.2 μm	Sputtering	Dalapati et al., 2016
11	ITO/Ag/ITO	91	96 at 2.4 μm	Sputtering	Present work

[#] discounting the substrate transmittance

5.3.4 Haze measurements

From the literature, it is noted that haze measurement is one of the required properties for the optical coatings (Heo et al., 2014; Liu et al., 2011; Preston et al., 2013). However, there are no reported data available for the haze measurements of IAI multilayer spectrum splitting coatings. The required value of haze is dependent on the

nature of applications. For the application related to heat reflecting through the windows, the low haze value is preferable for the clear vision. However, for the hybrid solar power system and photovoltaic applications, high haze factor is required for the effective trapping of incident light by scattering and increasing the area of absorption (Heo et al., 2014; Preston et al., 2013). Optical haze factor of IAI multilayer coating on plain and one side etched glass were calculated in the wavelength range from 380 to 780 nm using the equation (2.2). The measurements showed that the multilayer coating on the plain glass has the haze value 0.45%, but haze for the IAI multilayer on one side etched glass increased to 1.30% (shown in Figure 5.7).

The increase in the haze value of the one side etched glass is due to the nano porous microstructure developed on the etched surface of the glass; this nanoporous microstructure scatters the light and increases the haze of the substrate.
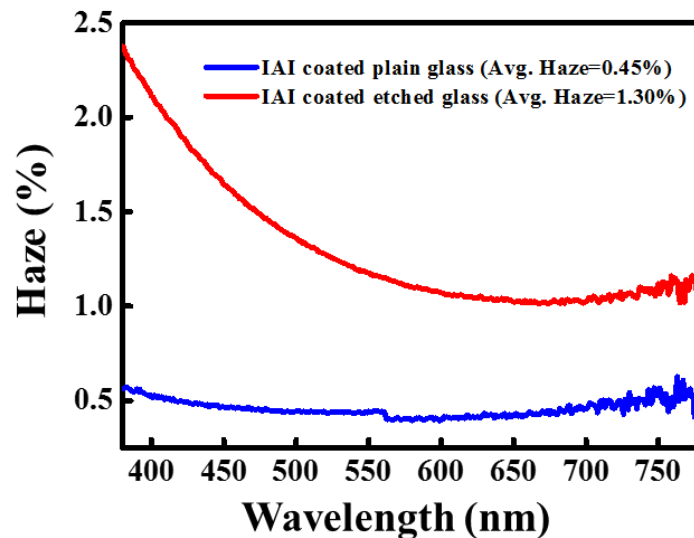
Figure 5.7: Measured haze factor of IAI (60/21/60 nm) multilayer on plain and single side etched glass substrate.

5.3.5 Angular reflection

Most of the time, optical properties of IAI multilayer coatings are characterized only by using the normal incident light. However, due to the changing position of the sun during the day, the angular dependent optical studies of these coatings are also

important for hybrid solar energy conversion. Therefore, the influence of angular and polarization dependence of IAI multilayer coatings have been investigated. Figure 5.8(a-f) shows the angular reflection properties of IAI (60/21/60 nm) multilayer coating on a plain glass, with varying angle of incidence (8 to 68°), in the wavelength range 250-2500 nm.
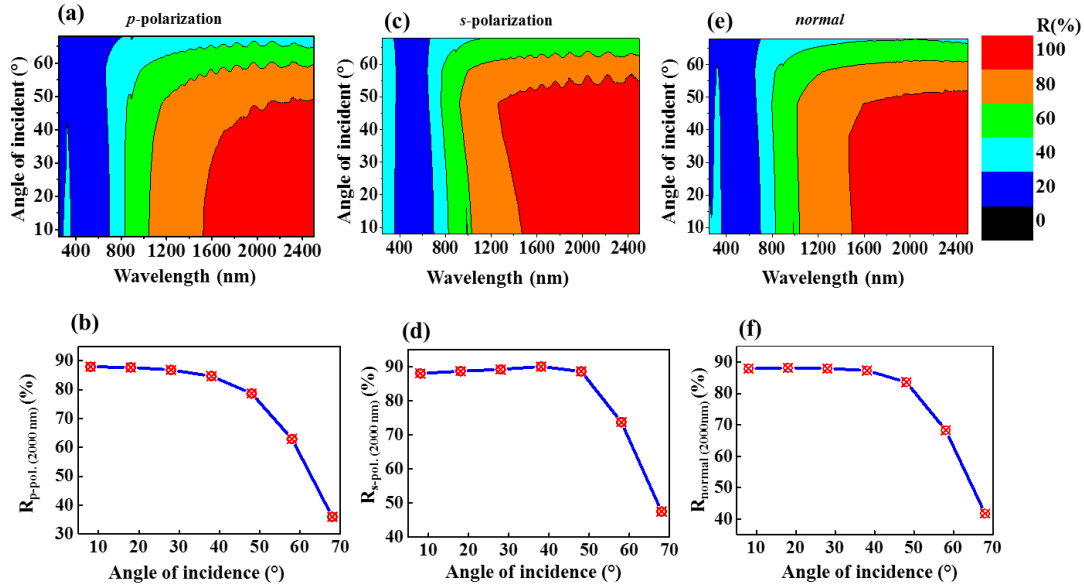
Figure 5.8: Angular absolute reflectance studies of IAI (60/21/60 nm) multilayer system: (a) and (b) contour plot and reflectance at 2000 nm for various angles of incidence, respectively for p-polarization; (c) and (d) contour plot and reflectance at 2000 nm for various angles of incidence, respectively for s-polarization. (e) and (f) Contour plot and reflectance at 2000 nm for various angles of incidence, respectively for normal angle of incidence.

From Figure 5.8(a) one can see that for *p*-polarized (transverse magnetic, TM) light, the reflectance ($R_{p\text{-pol.}}$) of IAI multilayer at the lower angle of incidence ($\leq 48°$) did not change much, but at a higher angle of incidence ($\geq 58°$) the NIR $R_{p\text{-pol.}}$ dropped significantly. For more clarity, $R_{p\text{-pol.}}$ at 2000 nm wavelength with varying angle of incidence is shown in Figure 5.8(b). For the *s*-polarized (transverse electric, TE) light, the reflectance ($R_{s\text{-pol.}}$) of IAI multilayer (shown in Figure 5.8(c)) at higher wavelength remains almost constant till 48° angle of incidence, but beyond 48° a sharp decrease in $R_{s\text{-pol.}}$ is noticed. Figure 5.8(d) shows the $R_{s\text{-pol.}}$ at 2000 nm wavelength with varying

angle of incidence. The average reflectance $[R_{av.} = (R_{s-pol.} + R_{p-pol.})/2]$ values of s- and p-polarized light are also calculated and the data is shown in Figure 5.8(e). Total reflectance (R) at 2000 nm with varying angle of incidence is shown in Figure 5.8(f). From these studies, it can be conclude that the angular reflectance of IAI multilayer did not change much for incident angles up to 48°; after that reflection of multilayer decreased significantly.

5.4   Summary

ITO/Ag/ITO multilayer spectral beam splitter coatings were designed and developed for photovoltaic-thermoelectric hybrid system. The Ag and ITO layer thicknesses were varied in order to achieve high visible transmittance, high NIR/IR reflectance and optimum cut-off wavelength. The figure-of-merit results showed that the optimized thicknesses of Ag and ITO layers were 21 and 60 nm, respectively. The optimized IAI multilayer coatings exhibit high visible transmittance (~88%) and high NIR/IR reflectance. In order to improve the transmittance, a novel chemical etching method was used. The chemical etching on single side glass substrate resulted in nano-porous surface morphology, which acts as an antireflection coating. This nano-porous morphology combined with IAI multilayer system resulted in an increase in transmittance from 88% to 91%. The optical haze value of IAI multilayer on plain and single side etched glass was found to be 0.45% and 1.30%, respectively. The angular and polarization dependence studies showed that the IAI multilayer coatings are angular insensitive up to 48° of angle of incidence of light.

CHAPTER 6

CHARACTERIZATION OF ITO/Ag/ITO MULTILAYER THIN FILMS ON FLEXIBLE SUBSTRATES FOR TRANSPARENT CONDUCTOR APPLICATIONS

In this Chapter, optimization of ITO/Ag/ITO multilayers for the transparent conductor application is described. Estimation of the optimum ITO and Ag layer thicknesses is obtained through the calculation of the figure of merit deduced from the transmittance and the sheet resistance of the IAI multilayers. The optimized IAI multilayer coating is also deposited on flexible FEP and Kapton® substrates. The electrical, optical, structural and morphological properties of IAI deposited on glass and FEP substrates are compared.

6.1   Introduction

As the importance of flexible transparent electrodes is increasing in recent years, new combination of transparent electrodes and flexible substrates are being studied extensively. FEP is a commercially available flexible transparent film. FEP shows high solar transmittance, very good mechanical and thermal insulating properties. It has been reported that FEP substrates show no much change in the optical properties even after the exposure of 1 sun solar radiation for 27 years (French et al., 2011; Jorgensen et al., 2000). However, there are no data available for the IAI transparent electrode coated FEP substrate in the literature. Similarly, commercially available flexible polyamide Kapton® is also a good substrate for flexible electronic applications (Muneshwar et al., 2010). Kapton® shows very good thermal resistant and good chemical stability and is also used in different areas of applications such as semiconductor, solar, space, etc. (Guillen and Herrero, 2003; Muneshwar et al., 2010; Teissier et al., 2012). But, there is not much data available in the literature on sputter-deposited transparent and conducting IAI coatings on Kapton® substrate. Therefore, the

study of highly transparent and conducting IAI coated flexible FEP and Kapton® substrates with good mechanical properties can be useful in many flexible electronic applications in future.

The optical properties of IAI multilayer coatings and optimization of ITO and Ag layer thicknesses on glass substrate for getting maximum efficiency for hybrid solar cell application were described in previous Chapter 5. In this Chapter, the electrical and optical properties of reactive sputtered IAI multilayer on rigid glass and flexible fluorinated ethylene propylene (FEP) and Kapton® substrates for optoelectronic applications are reported. It has been found from the Chapter 5 that, the maximum figure of merit that deduced from average solar transmittance and average NIR reflection was achieved when the Ag and ITO layers thicknesses were 21 and 60, respectively. But, for transparent conductors, maximum transmittance in the visible region of the solar spectrum especially at $\lambda = 550$ nm and lowest sheet resistance are the main concern, the high NIR reflection is not mandatory. Therefore, in this study, Ag layer thickness has been optimized to achieve maximum transmittance in visible region and lowest sheet resistance.

6.2   Experimental details

Transparent and conducting IAI multilayer was deposited on glass, FEP and Kapton® substrates by a multi-target balanced DC magnetron sputtering system. Borosilicate glass of thickness 1 mm and FEP film of thickness 127 µm and Kapton® film thickness 25 µm were used as the substrates. Prior to the deposition, the glass substrate was cleaned with acetone and iso-propylene alcohol (IPA) in ultrasonic agitator and blown dried with nitrogen gas. FEP and Kapton® substrates were cleaned in IPA and dried with nitrogen gas. Bottom and top ITO layer thicknesses were kept constant at 60 nm for all the depositions. Ag layer thicknesses was optimized on glass substrate for optimum optical transmittance and sheet resistance to achieve maximum figure of merit. Hereafter, the optimized ITO and Ag layers were deposited on FEP and Kapton® substrates. All the depositions, even on the glass substrates, were carried out at room temperature. To enhance the optical transmittance of IAI multilayer, the transmittance was enhanced by etching one side of the glass substrate. IAI multilayer was deposited on non-etched side of the glass substrate. Etching of the glass substrate

was done using hydrogen fluoride (HF) vapours. IAI multilayer was also deposited on one side plasma etched FEP substrate to study the effect of etching on the optical and haze properties of multilayer system. FEP etching was carried out using a plasma etching instrument, Plasma Matrix (BDISCOM) at RF power 100 W in argon atmosphere at room temperature. Etching was done for different durations to increase the roughness of FEP substrate.

Total, specular and diffuse optical transmittance, and haze of the IAI multilayer on glass and FEP substrates were measured using UV/Vis/NIR spectrophotometer. Haze measurement was carried out as per the ASTM 1003 standard, using an integrating sphere attached with the spectrophotometer. Sheet resistance of IAI multilayer on both glass and FEP substrate was measured using four point probe setup. The crystal structure of IAI multilayer was investigated by X-ray diffractometer. The surface morphology of IAI multilayer was investigated using field emission electron microscopy (FESEM) and atomic force microscopy (AFM). Roughness of IAI coatings and substrates was obtained from AFM.

6.3   Results and discussion

6.3.1   Optimization of figure of merit of ITO/Ag/ITO on glass substrate (IAI/Glass)

Figure 6.1(a) shows the total transmittance of IAI/Glass of different Ag layer thicknesses and Figure 6.1(b) shows the transmittance at λ = 550 nm (T_{550nm}) and average transmittance ($T_{avg.}$) in the visible region of the solar spectrum (calculated for wavelength range from 400 to 800 nm) as a function of Ag layer thickness. It can be observed from the figure that at the lowest thickness of Ag layer (i.e, ~5 nm) the transmittance was low. Many previous studies have reported that at lower thickness Ag layer shows island like structure (Volmer-Weber growth mode) instead of continuous film, which affects the optical and electrical properties of multilayer adversely (Wang et al., 2006). While increasing the thickness of Ag layer, transmittance increased. Maximum transmittance of ~88.6% at λ = 550 nm was achieved when the Ag layer thickness was ~13 nm, and after that, the transmittance started to decline. At the same

time average transmittance was maximum (~83%) when Ag layer thickness was 9 nm; then it started to decrease.
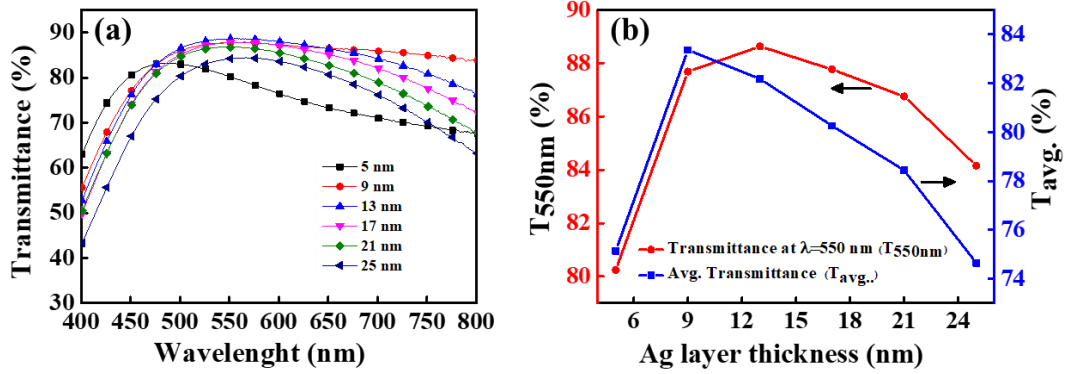
Figure 6.1: (a) Total visible transmittance; (b) transmittance at $\lambda = 550$ nm and average transmittance of IAI multilayers coated glass as a function of Ag layer thickness.

As described in the section 1.5.1 of Chapter 1, if each layer in IAI multilayer structure is considered as a parallel connection of three different resistances, the total sheet resistance (R_S) can be calculated from equation (1.8.). However, in the present work the top and bottom ITO layers have same thicknesses and were prepared at the same experimental conditions, the sheet resistance of both ITO should be equal. Therefore, the equation (1.8) can be modified as;

$$\frac{1}{R_S} = \frac{2}{R_{ITO}} + \frac{1}{R_{Ag}} \qquad (6.2)$$

On the other hand, the sheet resistance of ITO film (R_{ITO}) prepared at room temperature will be much higher than the sheet resistance of Ag film (R_{Ag}), therefore, R will be almost equal to the sheet resistance of Ag film alone. Indluru and Alford (2009) have reported that, as the work function of Ag (~4.4 eV) is smaller than the work function of ITO (~5.1 eV), the transfer of electrons from the metallic Ag film to ITO films will be easy (Indluru and Alford, 2009). Hence, the total resistance of multilayer will be near or lesser than the sheet resistance of metallic interlayer. Therefore, the role of ITO layers in IAI system is just to provide the high optical transmittance in the visible region. In this study, ~60 nm ITO film deposited on glass substrate in room temperature shows sheet resistance of ~500 Ω/sq., while a 13 nm thick Ag film on glass substrate shows sheet resistance of ~7.4 Ω/sq., which is very similar to the sheet resistance of

IAI coating with Ag thickness of ~13 nm (~7.1 Ω/square). Figure. 6.2(a) shows the measured sheet resistance and resistivity of IAI multilayer as a function of Ag layer thickness. Resistivity of the IAI multilayer was calculated as per the equation (2.4.). When the Ag layer thickness is too low (i.e., ~5 nm) the sheet resistance and resistivity were on the higher side (~42.9 Ω/sq. and ~5.37x10^{-4} Ω-cm, respectively), while increasing the Ag layer thickness both were decreased. Jeong and Kim (2009) have reported that, at lower thickness, the agglomerated island like growth of Ag films will not provide conducting path for electrons and the resistance will be high for IAI multilayer structure (Jeong and Kim, 2009). From Figures 6.1(b) and 6.2(a), it is very clear that ~9 nm is the minimum Ag layer thickness to form the continuous layer of Ag film, which is in very good agreement with the value reported in the literature (Jeong and Kim, 2009). Lowest sheet resistance ~4.8 Ω/sq. and resistivity ~7.0 x 10^{-5} Ω-cm were achieved when the Ag layer thickness was ~25 nm.
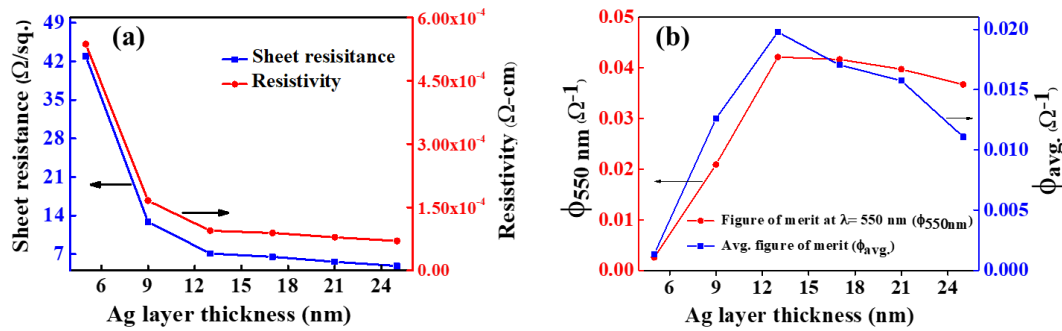
Figure 6.2: (a) Sheet resistance and resistivity; (b) figure of merit at λ = 550 nm ($\phi_{550\ nm}$) and average figure of merit ($\phi_{avg.}$) of IAI multilayer coated glass as a function of Ag layer thickness.

For transparent conductors figure of merit is an important parameter while optimizing the coating. To find out the optimum Ag thickness the figure of merit (ϕ) was calculated as per the equation (3.3). Figure of merit was calculated corresponding to the transmittance at λ = 550 nm, $\phi_{550\ nm}$, and average visible region transmittance, $\phi_{avg.}$. Figure 6.2(b) shows $\phi_{550\ nm}$ and $\phi_{avg.}$ of IAI coating for different thicknesses of middle Ag layer keeping both top and bottom ITO layer thicknesses at 60 nm. From

the figure, it can be seen that when the Ag film thickness is ~5 nm; lowest figure of merit ($\phi_{550\ nm}$~ 3 x 10^{-3} Ω^{-1} and $\phi_{avg.}$~ 1 x 10^{-3} Ω^{-1}) is achieved, because both the transmittance and the sheet resistance were very low. But with increasing thickness, the figure of merit increases. The maximum figure of merit ($\phi_{550\ nm}$~ 42 x 10^{-3} Ω^{-1} and $\phi_{avg.}$ ~ 20 x 10^{-3} Ω^{-1}) is achieved when the Ag thickness was ~13 nm. Beyond 13 nm even the sheet resistance decreased marginally, the figure of merit did not improve because the transmittance reduced due to higher Ag layer thickness. Therefore, from these results ~13 nm Ag thickness is found to be the optimum value for the transparent conductors.

To improve the figure of merit a porous nanostructured surface was fabricated on the non-coated side of glass substrate using a simple cost effective HF vapour phase etching process. The fabricated nanoporous surface acts as an antireflecting layer, which enhances the transmittance of glass substrate by ~3%. The details of vapor phase etching can be found elsewhere (Kumar et al., 2016). However, the structural and stoichiometry of IAI film will be intact and there will not be any change in the electrical properties of IAI film as the etching of the glass slide was on the non-coated side. An ITO (60 nm)/Ag (13 nm)/ITO (60 nm) multilayer was deposited on one side etched glass, which shows the transmittance of ~91.4% at λ = 550 nm and average transmittance of 86.8% in the visible region of the solar spectrum. Figure 6.3 shows the optical transmittance spectra of uncoated and IAI multilayer coated plain and etched glass substrates. Because of this improved transmittance of IAI multilayer through the etched glass, the figure of merit of IAI coating on etched glass improved to $\phi_{550\ nm}$ ~ 57 x 10^{-3} Ω^{-1} and $\phi_{avg.}$ ~ 33 x 10^{-3} Ω^{-1}. The figure of merit value attained in this work for IAI multilayer deposited on one side etched glass substrate is highest reported so far for indium tin oxide layer deposited using metal alloy target (In:Sn), and these values are much higher than the figure of merit value optimized for flat panel display applications (Bender et al., 1998; Girtan, 2012; Kim et al., 2010). Table 6.1 shows a comparison of figure of merit of different multilayer structure coatings on glass substrate.

Table 6.1: Comparison of figure of merit of different multilayer structures deposited on glass substrate.

S. No.	Multilayer structure*	Deposition method	Target for dielectric films deposition	$\phi_{\lambda=550\,nm}$ $(10^{-3}\,\Omega^{-1})$	Ref.
1	ITO/Ag/ITO	Sputtering	Oxide (10% SnO_2, 90% In_2O_3)	85[#1]	Guillén and Herrero, 2008
2	ITO/Cu/ITO	Sputtering	Oxide (10% SnO_2, 90% In_2O_3)	50	Guillén and Herrero, 2008
3	ITO/Ag/ITO	Reactive sputtering	Metallic (90% In, 10% Sn)	21	Girtan, 2012
4	ITO/Au/ITO	Reactive sputtering	Metallic (90% In, 10% Sn)	17	Girtan, 2012
5	ITO/Ag/Au/ITO	Reactive sputtering	Metallic (90% In, 10% Sn)	24	Girtan, 2012
6	ZnO/Ag/ZnO	Reactive sputtering	Metallic (Zn 100%)	7	Girtan, 2012
7	ZnO/Au/ZnO	Reactive sputtering	Metallic (Zn 100%)	58	Girtan, 2012
8	ITO/Ag/ITO	Sputtering	Oxide (10% SnO_2, 90% In_2O_3)	51.9[#2]	Kim et al., 2016
9	ITO/AgCu/ITO	Sputtering	Oxide (10% SnO_2, 90% In_2O_3)	28.3	Bender et al., 1998
10	ITO/Ag/ITO	Sputtering	Oxide (10% SnO_2, 90% In_2O_3)	49.3	Jeong and Kim, 2009
11	ITO/Ag/ITO	Sputtering	Oxide (10% SnO_2, 90% In_2O_3)	47.8	Y.-S. Park et al., 2009
12	ITO/Cu/ITO	Sputtering	Oxide (10% SnO_2, 90% In_2O_3)	~4	Y.-S. Park et al., 2009
13	ITO/Ag/AZO	Sputtering	Oxide (10% SnO_2, 90% In_2O_3)	22	Boscarino et al., 2014
14	ITO/Ag/ITO	Sputtering	Oxide (10% SnO_2, 90% In_2O_3)	4.9	Boscarino et al., 2014
15	AZO/Ag/AZO	Sputtering	Oxide (5% Al_2O_3, 95% ZnO)	20	H. K. Park et al., 2009
16	GZO/Ag/GZO	Sputtering	Oxide (3% Ga_2O_3, 97% ZnO)	32	H. K. Park et al., 2009
17	ZnS/Cu/Ag/ZnS	evaporation	ZnS powder	70[#2]	Mouchaal et al., 2015
18	MoO_3/Ag/MoO_3	evaporation	MoO_3 powder	16[#2]	Cattin et al., 2013
19	AZO/Ag/AZO	e-Beam	Oxide (2% Al_2O_3, 98% ZnO)	25	Sahu et al., 2008
20	ITO/Ag/ITO	Reactive sputtering	Metallic (In 90%: Sn 10%)	42	Present work
21	ITO/Ag/ITO	Reactive sputtering	Metallic (In 90%: Sn 10%)	57	Present work

*S.No. 1-20 deposited on glass substrate, whereas Sl.No 21 deposited on one side etched glass.
ϕ calculated with #1 discounting the substrate transmittance, #2 average transmittance
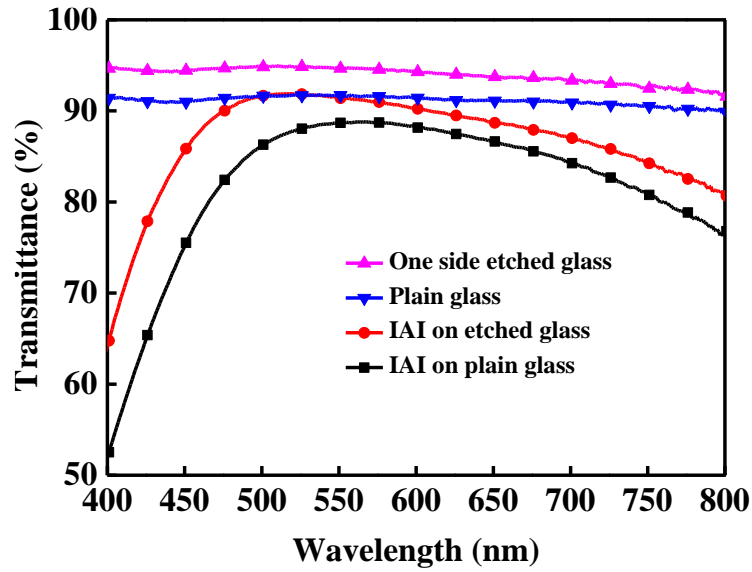
Figure 6.3: Total visible transmittance of IAI multilayer deposited on plain and one side etched glass substrates along with the transmittance of uncoated plain and etched glass substrate.

6.3.2 IAI coating on flexible FEP substrate (IAI/FEP)

The optimized ITO (60 nm)/Ag (13 nm)/ITO (60 nm) coating was coated on flexible FEP substrate. The transmittance spectra of IAI coated FEP and glass along with transmittance of uncoated substrates are shown in Figure 6.4. IAI coating on FEP showed higher transmittance than the IAI on rigid glass substrates. The transmittance of IAI coating reached to ~90.2% at $\lambda = 550$ nm on FEP substrate compared to ~88.6% transmittance on plain glass substrate, which is attributed to the high transmittance of FEP substrate (T ~ 95.2% at $\lambda = 550$ nm). The measured sheet resistance of IAI multilayer on FEP was ~6.9 Ω/sq. Therefore, high figure of merit, $\phi_{550\,nm}$ ~ 52 x 10^{-3} Ω^{-1} and $\phi_{avg.}$ ~ 29 x 10^{-3} Ω^{-1} was obtained for IAI multilayer on FEP substrate. This is also the highest transparent conductor figure of merit value attained for IAI multilayer on a flexible substrate using metal alloy (In:Sn) target for depositing ITO layers. Table 6.2 shows a comparison of figure of merit of different multilayer coatings on different flexible substrates reported in the literature. No reported figure of merit for IAI multilayer deposited on FEP substrate was found in the literature.
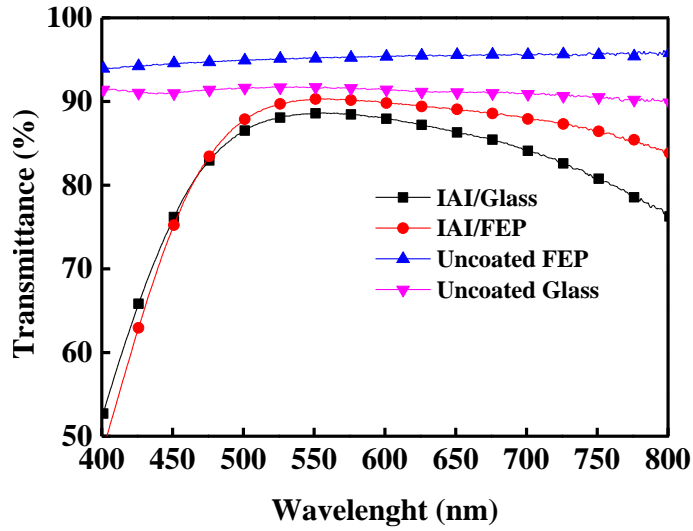
Figure 6.4: Total visible transmittance of IAI multilayer deposited on plain FEP and glass substrates along with the transmittance of uncoated glass and FEP substrates.

Table 6.2: Comparison of figure of merit of different multilayer structures deposited on flexible substrates.

Flexible substrate	Multilayer structure	Deposition method	Target for dielectric film deposition	$\phi_{\lambda=550\,nm}$ $(10^{-3}\,\Omega^{-1})$	Ref.
Polyethersulfone (PES)	ITO/Ag/ITO	Sputtering	Oxide (10% SnO_2, 90% In_2O_3)	75	Y.-S. Park et al., 2009
Polyethylene terephthalate (PET)	ITO/Ag/ITO	Reactive sputtering	Metallic (In 90%: Sn 10%)	29	Girtan, 2012
Polyethylene terephthalate (PET)	ITO/Au/ITO	Reactive sputtering	Metallic (In 90%: Sn 10%)	16	Girtan, 2012
Polyethylene terephthalate (PET)	ITO/Ag/Au/ITO	Reactive sputtering	Metallic (In 90%: Sn 10%)	28	Girtan, 2012
Polyethylene terephthalate (PET)	ZnO/Ag/Au/ZnO	Reactive sputtering	Metallic (Zn)	15	Girtan, 2012
Polyethylene naphthalate (PEN)	ITO/Ag/ITO	Sputtering	Oxide (10% SnO_2, 90% In_2O_3)	26.1	Indluru and Alford, 2009
Polyethylene terephthalate (PET)	ITO/Ag/ITO	Sputtering	Oxide (10% SnO_2, 90% In_2O_3)	7	Fahland et al., 2001
Polyethylene naphthalate (PEN)	TiO_2/Ag/TiO_2	Sputtering	Oxide (TiO_2 100%)	6.4	Dhar and Alford, 2014 Dhar and A
Polycarbonate (PC)	ITO/Cu/ITO	Sputtering	Oxide (5% ZnO, 95% In_2O_3)	0.14	Lee et al., 2009
Polycarbonate (PC)	ITO/Au/ITO	Sputtering	Oxide (10% SnO_2, 90% In_2O_3)	6.6	Lee et al., 2009
Fluorinated ethylene propylene (FEP)	ITO/Ag/ITO	Reactive sputtering	Metallic (In 90%: Sn 10%)	52	Present work

102

6.3.3 Bending test of IAI/FEP

For realizing the mechanical stability of the flexible IAI multilayer, bending test of IAI/FEP was performed using a lab made automatic and speed controllable bending test system. Figure 6.5(a) shows the photograph of the initial position of IAI/FEP mounted on the bending tester. One side of the substrate was fixed on an immovable stand and the other side of the substrate was clamped on a movable plate. Figure 6.5(b) shows the photograph of bent position of IAI/FEP. Minimum bending radius of 3 mm could be possible by this bending test setup. The speed of movable plate was adjusted to 10 mm/sec, that is 15 bending cycle per minute. IAI/FEP was tested for 5000 bending cycles. The sheet resistance of IAI multilayer was measured after certain intervals of bending cycles. Change in the sheet resistance (ΔR_S) of IAI multilayer was calculated as $\Delta R_S = R_{S1} - R_S$, where R_S is the sheet resistance of IAI/FEP before bending test and R_{S1} is the sheet resistance after bending test (Park et al., 2016; Y.-S. Park et al., 2009).
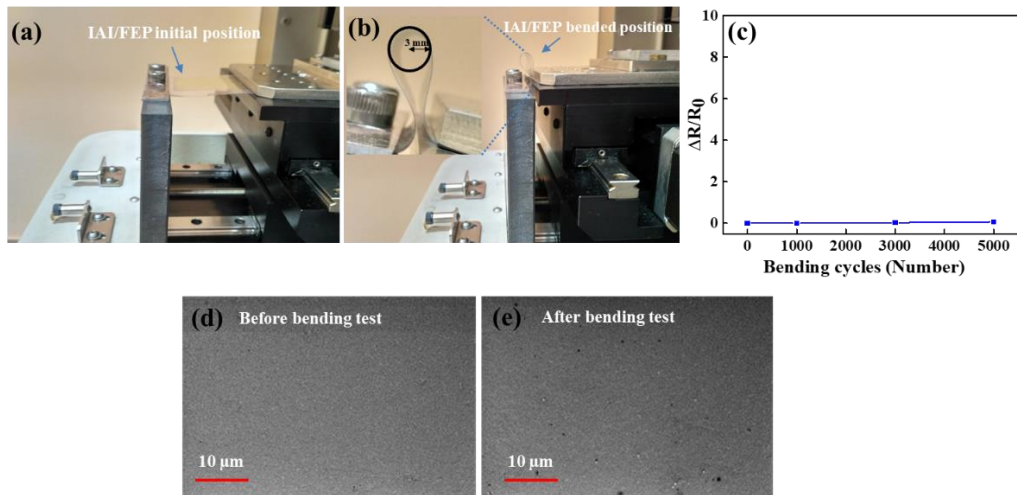
Figure 6.5: IAI/FEP bending test setup (a) initial position and (b) bent position. Inset of (b) shows the minimum bending radius of IAI/FEP substrate. (c) Shows the change in sheet resistance ($\Delta R_S/R_S$) of IAI multilayer as a function of bending cycle. (d) and (e) show FESEM micrographs of IAI/FEP substrate before and after bending test.

Figure 6.5(c) shows the $\Delta R_S/R_S$ value of IAI/FEP as a function of bending cycles. IAI/FEP showed very low $\Delta R_S/R_S$ value throughout the bending test, which

shows that the IAI multilayer on FEP substrate has very good flexibility and can be used for the flexible electrode applications. Figures 6.5(d) and (e) show the FESEM images of IAI/FEP before and after bending test, respectively, which display no cracks or delamination on the coating after bending tests.

6.3.4 Solar selectivity study of IAI/FEP

Lampert (1981) has reported that FEP substrate can be used as a substrate or as it is for the heat mirror application (Lampert, 1981). The solar spectrum selective property of IAI/FEP substrate also has been studied. Figure 6.6 shows the broad range solar spectrum (λ range from 250 to 2500 nm) transmittance and reflectance spectra of IAI coated FEP substrate. From the figure it can be seen that IAI deposited on FEP shows high transmittance in the whole visible spectrum region with minimum reflectance; at the same time high reflectance at NIR region with low transmittance. When IAI/FEP is used for the cover plate or electrode of solar cell the unwanted heat radiation reflects back, which can prevent the solar cell from heating and losing the efficiency (Ju et al., 2012). In addition, the solar spectrum selectivity of IAI/FEP can be useful in flexible solar segregator applications for hybrid solar cell to filter the visible and higher wavelength regions.
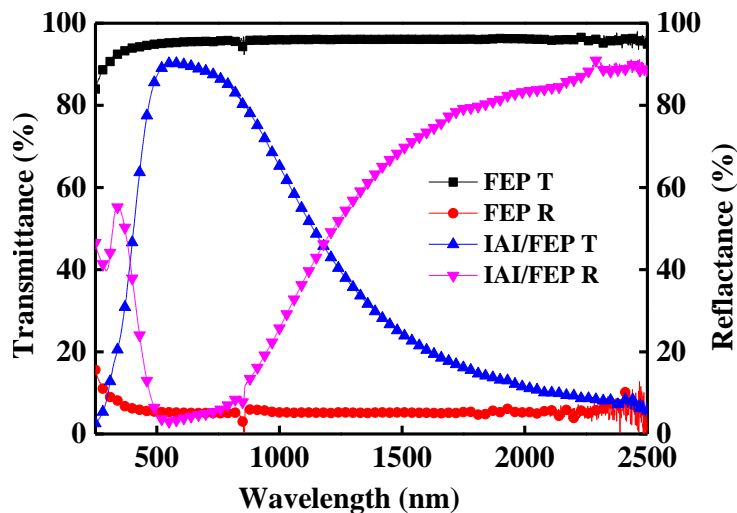
Figure 6.6: Solar spectrum total transmittance and reflectance of uncoated and IAI/FEP substrates for wavelength range of 250 to 2500 nm.

6.3.5 Structural and morphological studies

Figures 6.7(a) and (b) show the FESEM images of IAI multilayer on FEP and glass substrates, respectively, which show a fully covered and well-connected granular morphology of IAI coating on both the substrates. From the figure it can be noticed that IAI grains on FEP substrate are slightly larger than that on the glass substrate. Figures 6.7(c) and (d) show the respective AFM images of IAI multilayer on glass and FEP substrates. The average roughness (R_a) of IAI deposited on glass was ~1.6 nm and for IAI deposited on FEP, R_a was ~8.6 nm. The difference in the roughness values of IAI multilayer on glass and FEP substrate is because of the higher substrate roughness of FEP compared to glass substrate. To confirm this AFM images of uncoated FEP and glass were taken and the data is shown in Figures 6.7(e) and (f). From the figures it can be observed that glass has a smooth surface morphology with R_a ~ 0.9 nm, and the FEP substrate shows marginally higher roughness (i.e., R_a ~ 5.6 nm).

X-ray diffraction (XRD) patterns of IAI coated FEP and glass were taken to compare the crystalline structure (see Figure 6.8). The XRD patterns of ITO (60 nm)/Ag (13 nm)/ ITO (60 nm) multilayer on both substrates show a broad ITO (222) peak and Ag (111) peak. Usually a standard transparent and conducting ITO film exhibits a well polycrystalline cubic structure, but in the present case the broad single ITO peak indicates a nanocrystalline phase of ITO film (Girtan, 2012; Indluru and Alford, 2009). It has been reported that the ITO film crystallization depends on the thickness of the film. At lower thicknesses, ITO films are amorphous and with increasing film thickness the crystallization increases. Irrespective of higher grains on FEP substrate that can be observed from the FESEM images, much broader peaks were obtained for IAI coating on FEP. This is because of the superimposition of XRD peaks of bare FEP substrate and those of ITO and Ag. From these results, it is inferred that the structure of IAI coating on both glass and FEP substrates is almost similar.
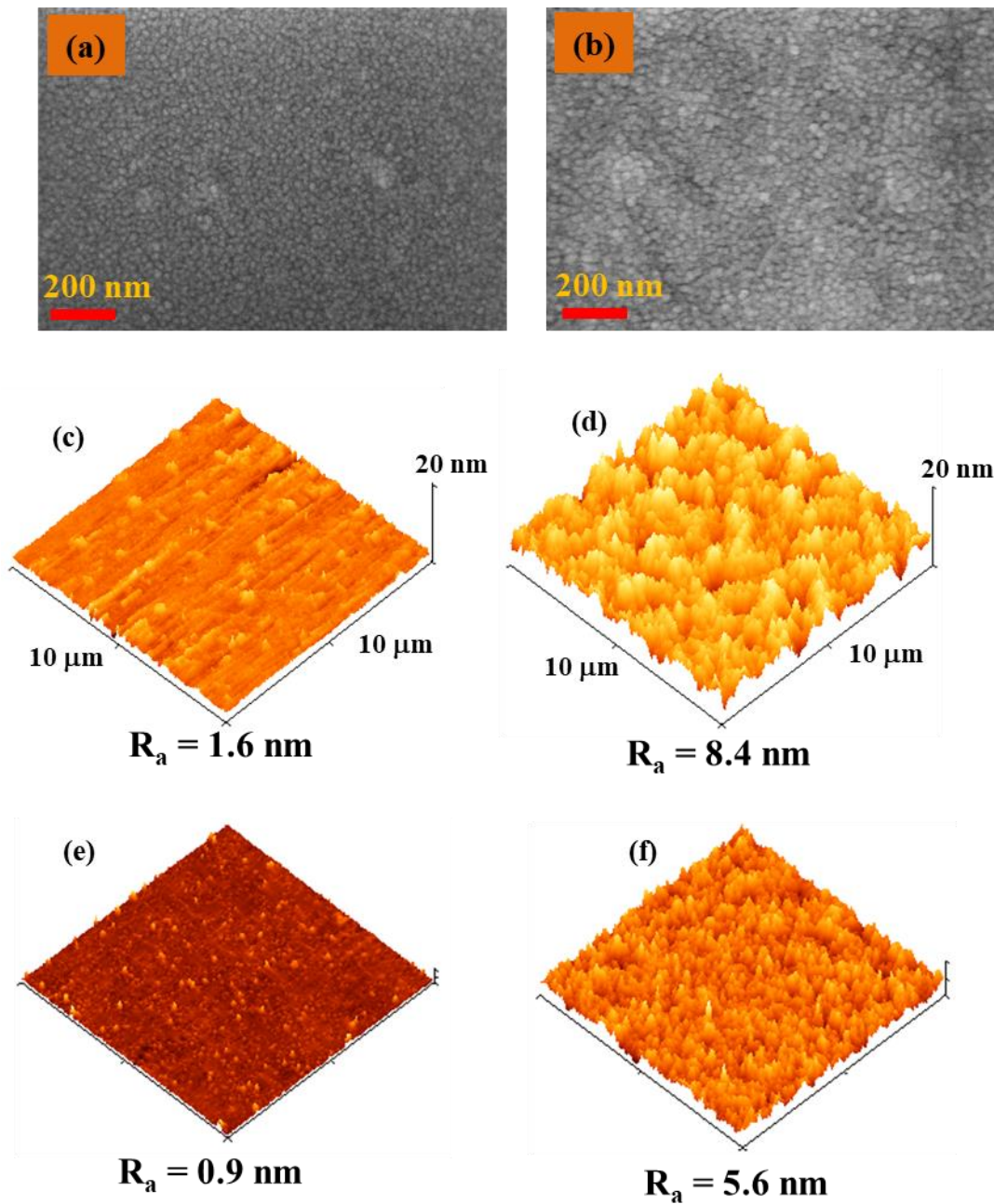
Figure 6.7: (a) and (b) show the FESEM images and (c) and (d) show the AFM images of IAI/Glass and IAI/FEP, respectively. (e) and (f) show the AFM images of uncoated glass and FEP substrates.
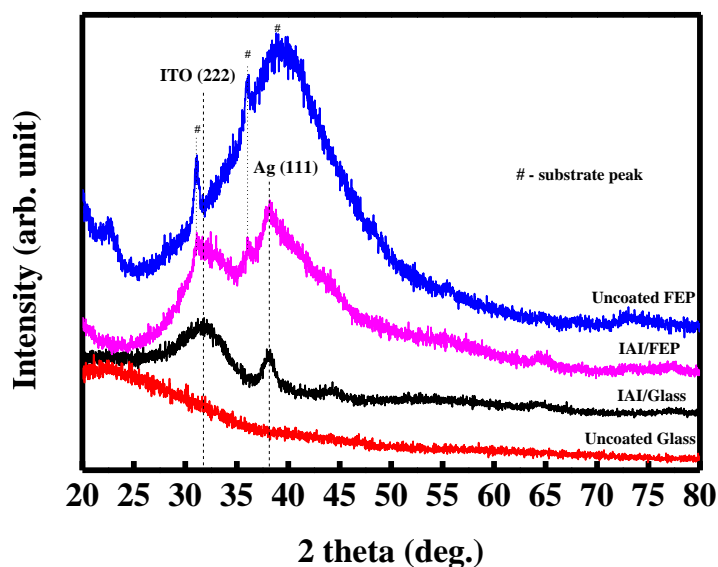
Figure 6.8: The XRD patterns of uncoated and IAI coated FEP and glass substrates. # denotes reflections from FEP substrate.

6.3.6 Haze measurements

The average haze factor of the optimized ITO (60 nm)/Ag (13 nm)/ ITO (60 nm) multilayer on a plain glass substrate was found to be ~0.4%. However, average haze of IAI multilayer of the same optimized thickness on the etched glass increased to ~1.5%. The increase in the haze factor of IAI multilayer deposited on etched glass is due to the roughness created on the glass substrate while etching.

The haze of IAI multilayer deposited on etched FEP substrate was also studied. FEP etching was carried out using RF plasma. Only one side of the FEP substrate was etched. Etching was done for different durations to increase the surface roughness. Figures 6.9(a-c) show the AFM images of etched surface of FEP substrate for different durations. A large difference in the average roughness was found after plasma etching. Roughens increased with an increase in etching time. R_a of ~80 nm has been obtained for 14 min etched sample. Further, the optimized IAI multilayer (ITO (60 nm)/ Ag (13 nm)/ ITO (60 nm)) was deposited on the non-etched side of the FEP (IAI/FEP-etched) substrates, and the total, specular and scattered transmittance and haze factor were measured (see Figure 6.9(d)). From Figure 6.9(d) it can be seen that there was no much difference in the total transmitted (T_{total}) light through the IAI/FEP-etched samples,

107

however, the diffused or scattered part of the transmitted radiation ($T_{diffuse}$) through IAI/FEP-etched samples increased with increasing etching duration. The specular transmittance ($T_{specular}$) shows a decrease with increasing the FEP etching duration.

Figure 6.9(e) shows the haze measurement of IAI/FEP-etched samples. As expected, the measured haze of IAI/FEP-etched substrates showed significant increase with an increase in the etching duration. The average haze value is calculated and plotted along with the change in the roughness as the function of etching duration in Figure 6.9(f). From the figure it can be seen that the average haze increased linearly with increasing the roughness of FEP. Therefore, without any additional coating or texturing of IAI multilayer it could be possible to increase the haze value from ~1.2% of plain FEP (0 min etched) to as higher as ~42% for 14 min etched FEP with R_a of ~80 nm. However, further increasing the etching duration the haze did not improve. As the roughness was introduced on the non-coated side, there will not be any change in the sheet resistance of IAI multilayer. Therefore, when IAI/FEP-etched is used as a transparent electrode in solar cell, the increased haze value increases the efficiency of the solar cell. From these observations it can be concluded that haze of IAI/FEP can be tuned with respect to the application by introducing the roughness on the non-coated side of the substrate.
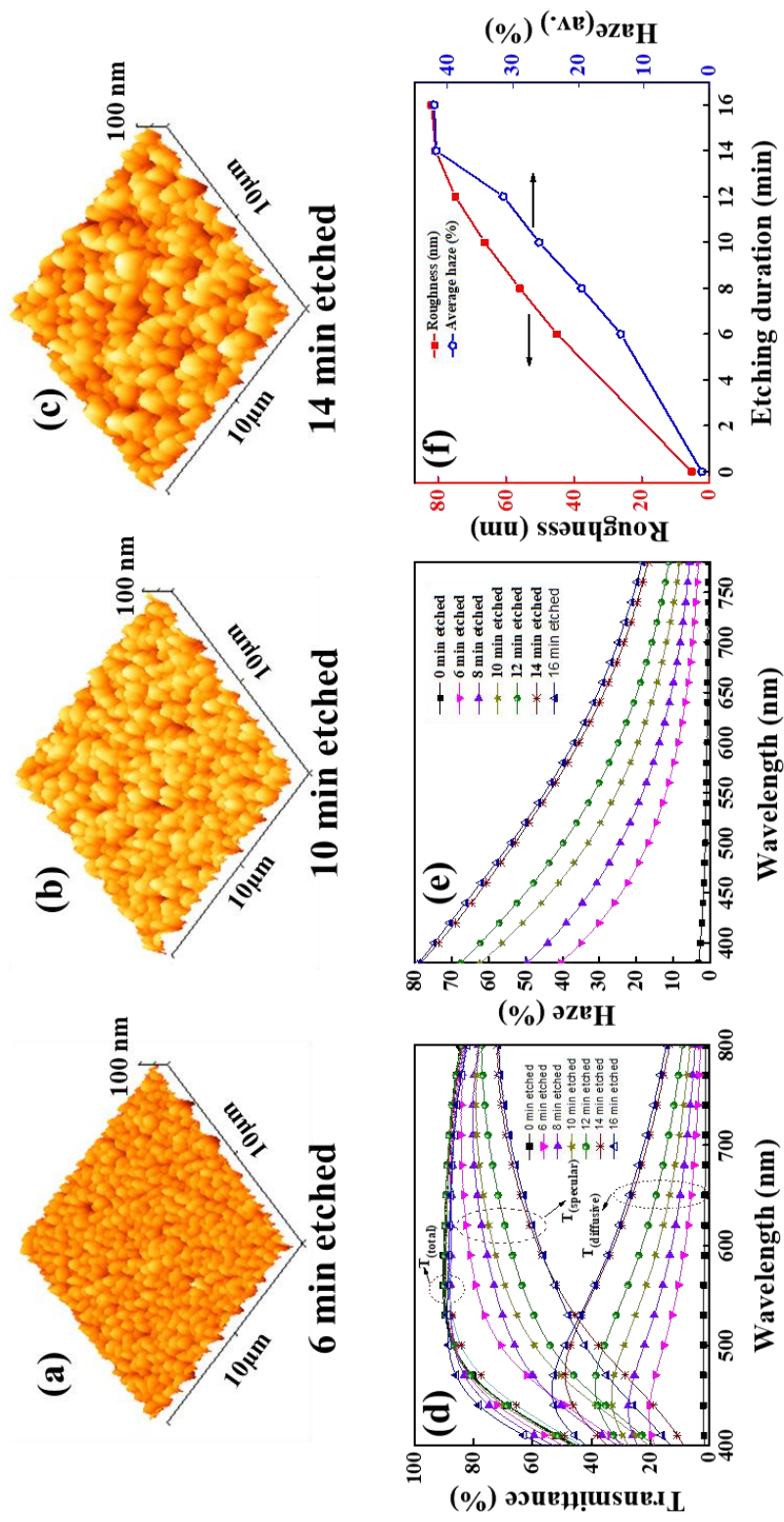
Figure 6.9: (a-c) show the AFM surface images of etched FEP substrate for different durations. (d) shows the total, specular and diffuse transmittance of IAI/FEP-etched for different durations of etching. (f) shows the average roughness and average haze as a function of etching duration.

6.3.7 IAI multilayers on flexible Kapton® substrate

The optimized ITO (60 nm)/Ag (13 nm)/ITO (60 nm) was coated on flexible Kapton® substrate also. Figure 6.10(a) shows the schematic diagram of IAI layers on the Kapton® substrate. Figure 6.10(b) shows the photographs of IAI coated and bare Kapton® substrates. IAI coated Kapton® substrate shows almost same optical transmittance as the bare Kapton® substrate. Moreover, all layers were deposited at room temperature, therefore no deformation occurred for Kapton® substrate during the deposition.
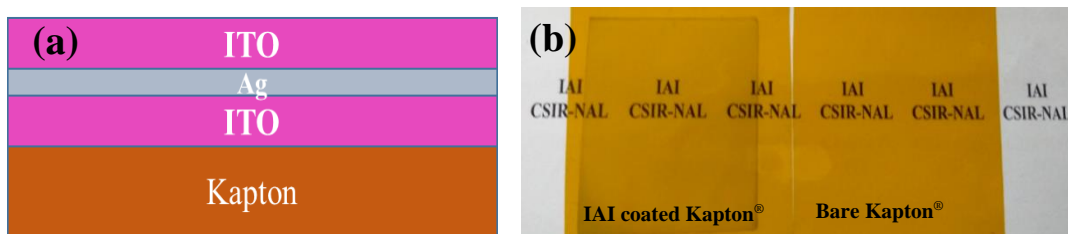
Figure 6.10: (a) Schematic diagram of ITO/Ag/ITO coating on Kapton® substrate (b) Photograph of bare and IAI coated Kapton®.

Figure 6.11 shows the transmittance and reflectance spectra of bare and IAI coated Kapton® substrates. From the figure, it can be seen that IAI coating did not decrease the transmittance of bare Kapton® much in visible region of the solar spectrum. Maximum transmittance as high as ~81.3% at 650 nm with sheet resistance value of 8.54 Ω/sq. has been achieved for IAI coated Kapton® while bare Kapton® shows transmittance of ~83.1% at 650 nm and sheet resistance >40 M Ω/sq. However, the transmittance decreases with increasing the wavelength at high wavelength side, which is ascribed to the reflection of the incident radiation by high electron density of IAI film (Edwards et al., 2004). Reflectance data of IAI coated and bare Kapton® substrates are shown in Figure 6.11(b). From the reflectance spectra, it is clear that reflectance has increased at higher wavelength.
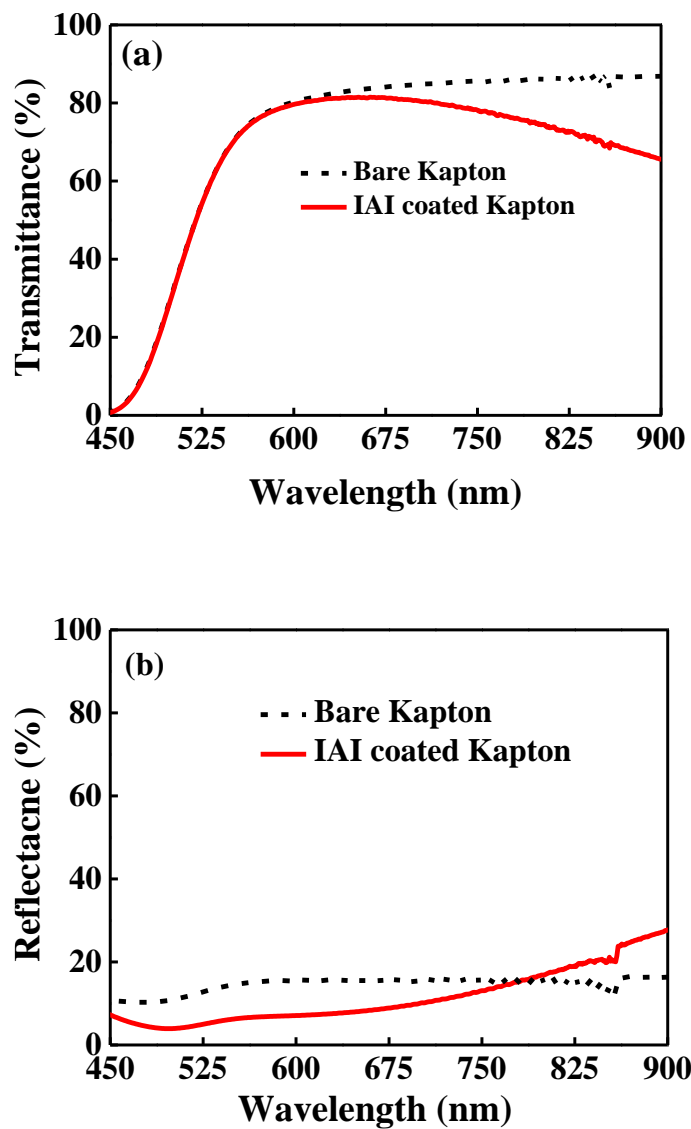
Figure 6.11: (a) Transmittance and (b) reflectance spectra of bare and ITO/Ag/ITO coated Kapton® substrates.
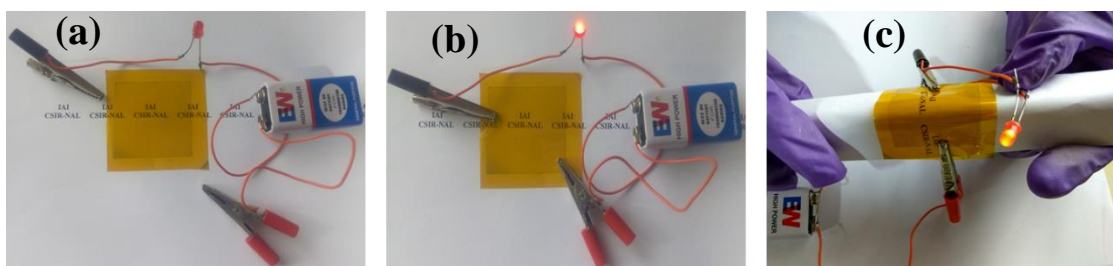
Figure 6.12: Photographs of (a) open circuit (b) closed circuit and (c) closed bent IAI coated Kapton® substrate.

In order to demonstrate the effectiveness of IAI coated Kapton® as the transparent flexible electrode, a circuit have been designed as shown in the Figure 6.12. Figure 6.12(a) shows the photograph of an open circuit, where the battery terminals are not connected to the IAI Kapton® so the LED was not glowing. Figure 6.12(b) shows the closed circuit with IAI coated Kapton® electrode, where it can be seen that LED is glowing, which proves that the electrical charge could pass through the IAI coated Kapton® because of its low resistance. Therefore, the IAI coated flexible Kapton® can be used it in optoelectronic devices as a transparent electrode. To check its mechanical flexibility IAI coated Kapton® substrate has been bent during closed circuit, however, the LED was still glowing even at bent position (Figure 6.12(c)), which shows the continuous electrical conductance through the IAI. These results show that IAI coated Kapton® can be used in flexible electronic applications.

The haze factor of bare and IAI coated Kapton® substrate was measured for wavelength range 450 nm to 780 nm. Figure 6.13 shows the haze measurement of IAI coated Kapton® substrate. From the figure, it can be seen that the optical haze of IAI coated Kapton® was very less and within the range required for optical coatings, which makes it a good candidate for optical applications like displays, smart windows, etc.
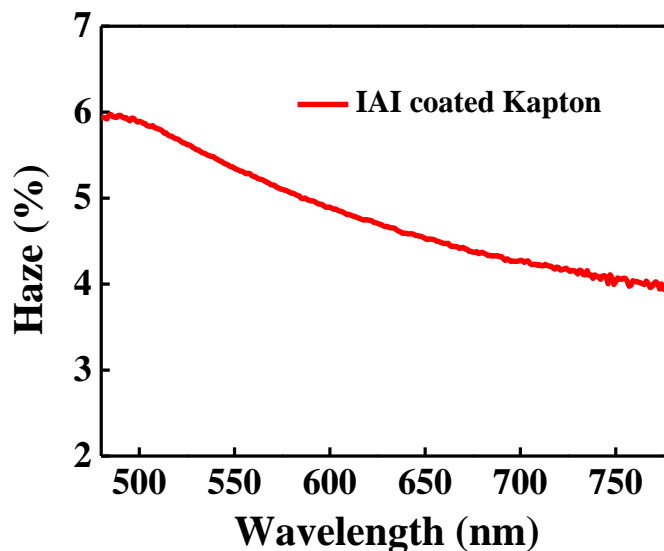
Figure 6.13: Haze factor of IAI coated Kapton® substrate.

Figure of merit (ϕ) values of IAI coating are calculated. Figure 6.14 shows the figure of merit values in the visible region of spectrum at different wavelength. ϕ at

550 nm was $3.28 \times 10^{-3} \ \Omega^{-1}$, and the maximum ϕ of $15 \times 10^{-3} \ \Omega^{-1}$ was achieved at 650 nm.
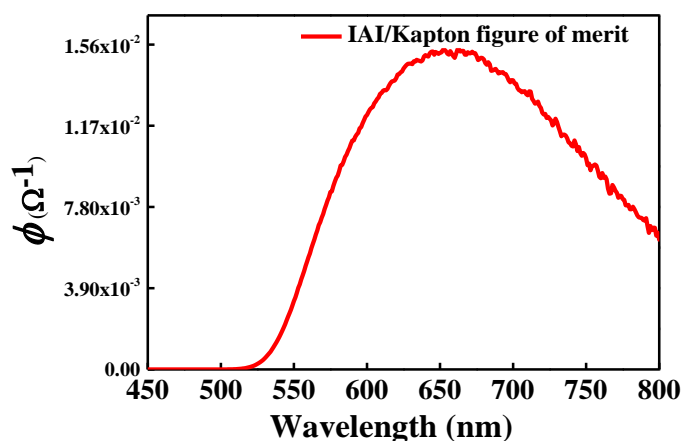
Figure 6.14: Figure of merit of IAI coated Kapton® substrate in the visible spectrum.

6.4   Summary

ITO/Ag/ITO multilayers were sputter deposited on glass and flexible FEP substrates by reactive magnetron sputtering system using In:Sn (90%:10%) and Ag metal targets at room temperature. The influence of Ag layer thickness on the optical and electrical properties of IAI multilayer was studied by keeping bottom and top ITO layers thicknesses at 60 nm. It is found that when Ag layer thickness was low (i.e., ~5 nm) the optical and electrical properties of IAI multilayer were not good. With increasing the Ag layer thickness, the transmittance increased and after reaching optimum thickness the transmittance decreases. Sheet resistance of IAI multilayer decreased with increasing Ag layer thickness. From the calculated figure of merit (ϕ) it is found that when the bottom and top ITO layers are ~60 nm thick, ~13 nm Ag thick layer is the optimum thickness needed for transparent conducting applications. Transmittance of ~88.6% at $\lambda = 550$ nm and a sheet resistance ~7.1 Ω/sq. were achieved for ITO (60 nm)/Ag (13 nm)/ITO (60 nm) coating on glass substrate with $\phi_{550 \ nm}$ of ~42 x $10^{-3} \ \Omega^{-1}$. HF vapour phase etching has been done on one side of the glass substrate to increase the transmittance of glass substrate by antireflection effect. IAI deposited on one side etched glass substrate showed improved transmittance of ~91.4% at $\lambda =$

550 nm, which also enhanced the $\phi_{550\ nm}$ to ~57 x 10^{-3} Ω^{-1}. Optimized IAI multilayer deposited on flexible FEP substrate showed transmittance of ~90.2% at $\lambda = 550$ nm and sheet resistance of ~6.9 Ω/sq. along with a $\phi_{550\ nm}$ of ~52 x 10^{-3} Ω^{-1}. FESEM images of IAI multilayer on glass and flexible FEP substrates show a well-connected granular morphology. IAI deposited FEP showed good solar spectrum selective properties. High transmittance in the visible region and high reflection in the NIR region of solar radiation spectrum of IAI/FEP can be useful in heat mirror applications. Further, it was demonstrated that without changing structural and electrical properties of IAI multilayer, the haze can be increased by creating the roughness on the non-coated side of the substrates by plasma etching. IAI coating deposited on Kapton® substrate shows maximum transmittance of ~81.3 % at $\lambda = 650$ nm and sheet resistance of 8.36 Ω/square. In summary, IAI coating on flexible FEP and Kapton® substrates show very good electrical and optical properties with good mechanical flexibility. Therefore, it will be useful in many flexible electronic applications.

CHAPTER 7

CONCLUSIONS AND SCOPE FOR THE FUTURE WORK

This Chapter summarizes the important findings of the present research work. In addition to that the scope of the future work is also included in the present Chapter.

7.1   Conclusions

The present work primarily aims at deposition of ITO and ITO/Ag/ITO (IAI) multilayer thin films on glass and flexible substrates, for their usefulness in space, solar and flexible optoelectronic applications. The salient features of this work is summarized below:

➢ Sputter deposited ITO thin film on FEP substrate shows desirable thermo-optical and sheet resistance properties for spacecraft application when the ITO film thicknesses are in the range of 10-15 nm.

➢ The simulated environmental study proved that ITO coatings deposited on Kapton® and aluminized Kapton® substrates, even without any surface treatment before the ITO deposition, are stable in harsh space environments.

➢ RF plasma etching is suitable to improve the adhesion of ITO coating on FEP substrates without changing FEP's thermo-optical properties.

➢ For solar spectrum splitter application the maximum figure of merit (Z-factor) of beam splitter is achieved for IAI multilayer on glass substrate, when the middle Ag layer thickness is 21 nm and top and bottom ITO layers thicknesses are at 60 nm.

➢ The transmittance of IAI multilayer in visible region of the solar spectrum, without affecting the high NIR-IR reflectance and cut-off wavelength, is increased by using HF vapour etched glass substrate

➢ ITO/Ag/ITO multilayer shows highest transparent and conducting figure of merit (ϕ) on glass substrate when the bottom and top ITO layers are at ~60 nm thick and middle Ag layer at ~13 nm thickness.

➢ Transparent conductor figure of merit of IAI/Glass can be increased by making an antireflection layer on the non-coated side of the glass substrate via HF vapour etching without affecting the sheet resistance of IAI multilayer.

➢ Another novelty of the present work is the deposition of IAI multilayer on flexible FEP and Kapton® substrates at room temperature.

➢ Haze study of IAI/FEP-etched showed that without any additional coating or texturing of IAI electrode, haze factor can be increased to 42% from 1.2% of plain FEP by increasing the roughness on non-coated side of FEP substrate by plasma etching.

To conclude, all the objectives of the thesis have been accomplished by providing significant amount of data and analysis thereof, in particular, optical and electrical properties of ITO based thin films for space, solar and flexible electronics applications are described in this work.

7.2   Scope for the future work

❖ Fabrication of thin film solar cell on glass substrate using IAI multilayer as the front transparent electrode.

❖ Fabrication of flexible solar cell using IAI multilayer electrode deposited on flexible FEP and Kapton® substrates.

❖ Practical use of IAI multilayer deposited one side etched glass substrate in a photovoltaic-thermoelectric hybrid solar conversion system and to evaluate the overall efficiency of the system.

❖ Finding an alternative for ITO thin films for spacecraft applications with required optical, electrical and thermal, and having the same stability as ITO in space environments.

❖ To improve the optical, electrical and mechanical properties of ITO electrode by incorporating other materials such as graphene, silver nanowires, metal mesh, etc.

❖ To enhance the stability of ITO coating on flexible substrate by surface passivation of substrate.

❖ To study the optical, electrical and mechanical properties of different types of dielectric/metal/dielectric multilayer systems for transparent conductor applications.

References:

Adamson, P., (2014). "Characteristic brewster angles for anisotropic interfaces" *Optik*, 125, 7247–7257.

Agarwal, M., Modi, P. and Dusane, R.O. (2013). "Study of electrical, optical and structural properties of Al-doped ZnO thin films on PEN substrates". *J. Nano-Electron. Phys.*, 5, 2027-1-4.

Agraharam, S., Hess, D.W., Kohl, P.A. and Allen, S.A.B. (1999). "Plasma chemistry in fluorocarbon film deposition from pentafluoroethane/argon mixtures". *J. Vac. Sci. Technol. A*, 17(6), 3265–3271.

Ahn, J.-H. and Hong, B.H. (2014). "Graphene for displays that bend". *Nat. Nanotechnol.*, 9, 737–738.

Ahn, M.H., Cho, E.S. and Kwon, S.J., (2014). "Characteristics of ITO-resistive touch film deposited on a PET substrate by in-line DC magnetron sputtering". *Vaccum*, 101, 221–227.

Al-Kuhaili, M.F., Al-Aswad, A.H., Durrani, S.M.A. and Bakhtiari, I.A. (2012). "Energy-saving transparent heat mirrors based on tungsten oxide–gold WO_3/Au/WO_3 multilayer structures". *Sol. Energy*, 86, 3183–3189.

Al-Kuhaili, M.F., Al-Aswad, A.H., Durrani, S.M.A. and Bakhtiari, I.A. (2009). "Transparent heat mirrors based on tungsten oxide–silver multilayer structures". *Sol. Energy*, 83, 1571–1577.

Álvarez-Fraga, L., Jiménez-Villacorta, F., Sánchez-Marcos, J., De Andrés, A. and Prieto, C. (2015). "Indium-tin oxide thin films deposited at room temperature on glass and PET substrates: optical and electrical properties variation with the H_2 – Ar sputtering gas mixture". *Appl. Surf. Sci.*, 344, 217–222.

Arfsten, N.J. (1984). "Sol-gel derived transparent IR-reflecting ITO semisconductor coatings and future applications". *J. Non. Cryst. Solids*, 63, 243–249.

118

ASTM D1003-00 (2000). "Standard test method for haze and luminous transmittance of transparent plastics," *ASTM International*, West Conshohocken, PA, www.astm.org.

ASTM D3359-07 (2007). "Standard test methods for measuring adhesion by tape test," *ASTM International*, West Conshohocken, PA, www.astm.org.

Badeker, K. (1907). "Über die elektrische leitfähigkeit und die thermoelektrische kraft einiger schwermetallverbindungen". *Ann. Phys*, 22, 749–766.

Bagal, A., Dandley, E.C., Zhao, J., Zhang, X.A., Oldham, C.J., Parsons, G.N. and Chang, C. (2015). "Multifunctional nano-accordion structures for stretchable transparent conductors". *Mater. Horizons*, 2, 486–494.

Barshilia, H.C., Selvakumar, N. and Rajam, K.S. (2008). "Structure and optical properties of pulsed sputter deposited Cr_xO_y/Cr/Cr_2O_3 solar selective coatings". *J. Appl. Phys.*, 103, 23507-1–11.

Bender, M., Seelig, W., Daube, C., Frankenberger, H., Ocker, B. and Stollenwerk, J. (1998). "Dependence of film composition and thicknesses on optical and electrical properties of ITO–metal–ITO multilayers". *Thin Solid Films*, 326, 67–71.

Bierwagen, O. (2015). "Indium oxide—a transparent, wide-band gap semiconductor for (opto)electronic applications". *Semicond. Sci. Technol.*, 30, 24001-1–16.

Bingel, A., Kevin, F., Kaiser, N. and Andreas, T. (2013). "Pulsed DC magnetron sputtering of transparent conductive oxide layers". *Chinese Opt. Lett.*, 11, S10201(1-5).

Binning, G., Quate, C.F. and Gerber, C. (1986). "Atomic force microscope". *Phys. Rev. Lett.*, 56, 930–934.

Biswas, N., Ghosh, P., Sarkar, S., Moitra, D., Biswas, P.K., Jana and S., Mukhopadhyay, A.K. (2015). "Nanomechanical properties of dip coated indium

tin oxide films on glass". *Thin Solid Films*, 579, 21–29.

Boscarino, S., Crupi, I., Mirabella, S., Simone, F. and Terrasi, A. (2014). "TCO/Ag/TCO transparent electrodes for solar cells application". *Appl. Phys. A*, 116, 1287–1291.

Bou, A., Torchio, P., Barkel, D., Thoulon, P.Y. and Ricci, M. (2016). "Numerical and experimental investigation of transparent and conductive TiOx/Ag/TiO electrode." *Thin Solid Films*, 617, 86-94

Brundle, C.R. and Baker, A.D. (1978). "*Electron Spectroscopy: Theory, Techniques and Applications-Volume 2*". Academic Press, New York.

Busscher, H.J., Stokroos, I., Van Der Mei, H.C., Rouxhet, P.G. and Schakenraad, J.M. (1992). "Preparation and characterization of superhydrophobic FEP-Teflon surfaces". *J. Adhes. Sci. Technol.*, 6, 347–356.

Camurlu, H.E., Kesmez, O., Burunkaya, E., Kiraz, N., Yesil, Z., Asilturk, M. and Arpac, E. (2012). "Sol–gel thin films with anti-reflective and self-cleaning properties". *Chem. Pap.*, 66, 461–471.

Cattin, L., Lare, Y., Makha, M., Fleury, M., Chandezon, F., Abachi, T., Morsli, M., Napo, K., Addou, M. and Bernède, J.C. (2013). "Effect of the Ag deposition rate on the properties of conductive transparent MoO_3/Ag/MoO_3 multilayers". *Sol. Energy Mater. Sol. Cells*, 117, 103–109.

Cattin, L., Morsli, M., Dahou, F., Abe, S.Y., Khelil, A. and Bernède, J.C. (2010). "Investigation of low resistance transparent MoO_3/Ag/MoO_3 multilayer and application as anode in organic solar cells". *Thin Solid Films*, 518, 4560–4563.

Chang, C.-H., Hsu, M.-H., Tseng, P.-C., Yu, P., Chang, W.-L., Sun, W.-C. and Hsu, W.-C. (2011). "Enhanced angular characteristics of indium tin oxide nanowhisker-coated silicon solar cells". *Opt. Express*, 19, A219–A224.

Chang, R., Tsai, F. and Tu, C. (2013). "A direct method to measure the fracture toughness of indium tin oxide thin fi lms on fl exible polymer substrates". *Thin*

Solid Films, 540, 118–124.

Chang, T., Wu, S., Xing, Z. and Wei, X. (2014). "Research on reverse association mechanism of the thermal control performance of conducting optical solar reflector and its antistatic properties". *Laser Mater. Process. Micro/Nano Technol.*, 9295, 929502-1-8.

Chen, A., Zhu, K., Zhong, H., Shao, Q. and Ge, G. (2014). "A new investigation of oxygen flow influence on ITO thin films by magnetron sputtering". *Sol. Energy Mater. Sol. Cells*, 120, 157–162.

Chen, P.-H., Chang, T.-C., Chang, K.-C., Tsai, T.-M., Pan, C., Chen, M., Su, Y., Lin, C., Tseng, Y., Huang, H., Wu, H., Deng, N., Qian, H. and Sze, S.M. (2016). "Resistance switching characteristics induced by O_2 plasma treatment of an indium tin oxide film for use as an insulator in resistive random access memory". *ACS Appl. Mater. Interfaces*, 9, 3149–3155.

Chen, S.-W., Bai, C.-Y., Jain, C.-C., Zhan, C.-J., Koo and C.-H. (2007). "Durability of indium tin oxide-silver-indium tin oxide films against moisture investigated through the wettability of the top oxide layer". *Mater. Trans.*, 48, 2230–2234.

Chendo, M.A.C., Jacobson, M.R. and Osborn, D.E. (1987). Liquid and thin-film filters for hybrid solar energy conversion systems". *Sol. Wind Technol.*, 4, 131–138.

Choi, K.H., Kim, J.Y., Lee, Y.S. and Kim, H.J. (1999). "ITO/Ag/ITO multilayer films for the application of a very low resistance transparent electrode." *Thin Solid Films*, 341, 152–155.

Chopra, K.L., Major, S. and Pandya, D.K. (1983). "Transparent conductors-a status review". *Thin Solid Films*, 102, 1–46.

Chow, T.T. (2010). "A review on photovoltaic/thermal hybrid solar technology". *Appl. Energy*, 87, 365–379.

Chuang, M. (2010). "ITO films prepared by long-throw magnetron sputtering without oxygen partial pressure". *J. Mater. Sci. Technol.*, 26, 577–583.

Colgrove, J. (2016). " Touch screen with ITO-replacement going to mainstream." ITO replacement, http://www.touchdisplayresearch.com (Apr. 30,2018).

Coutts, T.J., Young, D.L., Li, X., Mulligan, W.P. and Wu, X. (2000). "Search for improved transparent conducting oxides : A fundamental investigation of CdO , Cd_2SnO_4 , and Zn_2SnO_4". *J. Vac. Sci. Technol.*, A 18, 2646–2660.

Cullity, B.D. (1956). "*Elements of X-ray Diffraction*". Addison-Wesley Publishing Company, New York.

Czeremuszkin, G., Latrèche, M. and Wertheimer, M.R. (2001). "Charging/discharge events in coated spacecraft polymers during electron beam irradiation in a scanning electron microscope". *Nucl. Instruments Methods Phys. Res. B*, 185, 88–99.

Dalapati, G.K., Masudy-Panah, S., Chua, S.T., Sharma, M., Wong, T.I., Tan, H.R. and Chi, D. (2016). "Color tunable low cost transparent heat reflector using copper and titanium oxide for energy saving application". *Sci. Rep.*, 6, 20182-1-14.

Dang, M.T., Lefebvre, J. and Wuest, J.D. (2015). "Recycling indium tin oxide (ITO) electrodes used in thin-film devices with adjacent hole-transport layers of metal oxides". *ACS Sustain. Chem. Eng.*, 3, 3373−3381.

Dang, M.T., Wantz, G., Hirsch, L. and Wuest, J.D. (2017). "Recycling indium tin oxide (ITO) anodes for use in organic light-emitting diodes (OLEDs)". *Thin Solid Films*, 638, 236–243.

Dasilva, W., Entenberg, A., Kahn, B., Debies, T. and Takacs, G.A. (2012). Adhesion of copper to poly(tetrafluoroethylene-co-hexafluoropropylene) (FEP) surfaces modified by vacuum UV photo-oxidation downstream from Ar microwave plasma". *J. Adhes. Sci. Technol.*, 18, 1465–1481.

Dasilva, W., Entenberg, A., Kahn, B., Debies, T. and Takacs, G.A. (2006).

"Surface modification of Teflon® PFA with vacuum UV photo-oxidation". *J. Adhes. Sci. Technol.*, 20, 437–455.

Deubener, J., Helsch, G., Moiseev, A. and Bornhoft, H. (2009). "Glasses for solar energy conversion systems". *J. Eur. Ceram. Soc.*, 29, 1203–1210.

Dhar, A. and Alford, T.L. (2014). "Optimization of TiO2/Cu/TiO2 multilayer as transparent composite electrode (TCE) deposited on flexible substrate at room temperature". *ECS Solid State Lett.*, 3, N33–N36.

Dobrikov, G.H., Rassovska, M.M., Andreev, N.M., Boyadzhiev, S.I., Gesheva, K.A., Ivanova, T.M., Sharlandjiev, P.S. and Nazarowa, D.I. (2009). "Development of transparent heat mirrors based on metal oxide thin fi lm structures". *Thin Solid Films*, 518, 1091–1094.

Durrani, S.M.A., Khawaja, E.E., Al-shukri, A.M. and Al-kuhaili, M.F. (2004). "Dielectric/Ag/dielectric coated energy-efficient glass windows for warm climates". *Energy Build.*, 36, 891–898.

Edwards, P.P., Porch, A., Jones, M.O., Morgan, D.V. and Perks, R.M. (2004). "Basic materials physics of transparent conducting oxides". *Dalton Trans.*, 19, 2995–3002.

Ellmer, K. (2012). "Past achievements and future challenges in the development of optically transparent electrodes". *Nat. Photonics*, 6, 809–817.

Eshaghi, A. and Graeli, A. (2014). "Optical and electrical properties of indium tin oxide (ITO) nanostructured thin films deposited on polycarbonate substrates "thickness effect"". *Optik*, 125, 1478–1481.

Fahland, M., Karlsson, P. and Charton, C. (2001). "Low resisitivity transparent electrodes for displays on polymer substrates". *Thin Solid Films*, 392, 334–337.

Fahlteich, J., Steiner, C., Schiller, N., Miesbauer, O., Noller, K., Deichmann, K.-J., Mirza, M. and Amberg-Schwab, S. (2017). "Roll-to-roll thin film coating on fluoropolymer webs – status, challenges and applications". *Surf. Coatings*

Technol., 314, 160–168.

Fan, J.C.C. and Bachner, F.J. (1976). "Transparent heat mirrors for solar-energy applications". *Appl. Opt.*, 15, 1012–1017.

Fan, J.C.C., Goodenough, J.B., Fan, J.C.C. and Goodenough, J.B. (1977). "X-ray photoemission spectroscopy studies of Sn-doped indium-oxide films". *J. Appl. Phys.*, 48, 3524–3531.

Fix, A.R., Lopez, G.A., Brauer, I., Nuchter, W. and Mittemeijer, E.J. (2005). " Microstructural development of Sn-Ag-Cu solder joints". *J. Electron. Meter.*, 34, 137-142.

French, R.H., Rodriguez-Parada, J.M., Yang, M.K., Derryberry, R.A. and Pfeiffenberger, N.T. (2011). "Optical properties of materials for concentrator photovoltaic systems". *Sol. Energy Mater. Sol. Cells*, 95, 2077–2086.

Fuchs, F. and Bechstedt, F. (2008). "Indium-oxide polymorphs from first principles: Quasiparticle electronic states". *Phys. Rev. B*, 77, 155107-1–10.

Gilmore, D.G. (2002). "*Spacecraft Thermal Control Handbook, Fundamental Technologies, Vol. I* ". The Aerospace Press, California.

Girtan, M., (2012). "Comparison of ITO/metal/ITO and ZnO/metal/ZnO characteristics as transparent electrodes for third generation solar cells". *Sol. Energy Mater. Sol. Cells*, 100, 153–161.

Goldstein, R.D., Brown, E.M. and Maldoon, L.C. (1982). "Usage of ITO to prevent spacecraft charging". *IEEE Trans. Nucl. Sci.*, NS-29, 1621–1628.

Gordon, R.G. (2000). "Criteria for choosing transparent conductors". *Mrs Bull.*, August, 52–57.

Gorgolis, G. and Karamanis, D. (2016). "Solar energy materials for glazing technologies". *Sol. Energy Mater. Sol. Cells*, 144, 559–578.

Granqvist, C.G. (2007). "Transparent conductors as solar energy materials: a panoramic review". *Sol. Energy Mater. Sol. Cells*, 91, 1529–1598.

Granqvist, C.G. (1981). "Radiative heating and cooling with spectrally selective surfaces". *Appl. Opt.*, 20, 2606–2615.

Granqvist, C.G. and Hultåker, A. (2002). "Transparent and conducting ITO films: new developments and applications". *Thin Solid Films*, 411, 1–5.

Griffiths, P., Batty, W.J., Probert, S.D. and Knight, C. (1992). "Solar-control films". *Appl. Energy*, 41, 261–284.

Guillen, C. and Herrero, J. (2003). "Electrical contacts on polyimide substrates for flexible thin film photovoltaic devices". *Thin Solid Films*, 432, 403–406.

Guillén, C. and Herrero, J. (2011). "TCO/metal/TCO structures for energy and flexible electronics". *Thin Solid Films*, 520, 1–17.

Guillén, C. and Herrero, J. (2009). "Transparent conductive ITO/Ag/ITO multilayer electrodes deposited by sputtering at room temperature". *Opt. Commun.*, 282, 574–578.

Guillén, C. and Herrero, J. (2008). "ITO/metal/ITO multilayer structures based on Ag and Cu metal films for high-performance transparent electrodes". *Sol. Energy Mater. Sol. Cells*, 92, 938–941.

Gupta, N., Kavya, M. V, Singh, Y.R.G., Jyothi, J. and Barshilia, H.C. (2013). "Superhydrophobicity on transparent fluorinated ethylene propylene films with nano-protrusion morphology by Ar+O_2 plasma etching: study of the degradation in hydrophobicity after exposure to the environment". J. Appl. Phys., 114, 164307-1-8.

Haacke, G. (1976). "New figure of merit for transparent conductors". *J. Appl. Phys.*, 47, 4086–4089.

Han, H., Mayer, J.W. and Alford, T.L. (2006). "Band gap shift in the indium-tin-

oxide films on polyethylene napthalate after thermal annealing in air". *J. Appl. Phys.*, 100, 083715-1-6.

Hao, L., Diao, X., Xu, H., Gu, B. and Wang, T. (2008). "Thickness dependence of structural, electrical and optical properties of indium tin oxide (ITO) films deposited on PET substrates". *Appl. Surf. Sci.*, 254, 3504–3508.

Heavens, O.S. (1955). "*Optical Properies Of Thin Solid Films*". Dover Publications Inc, New York.

Hecht, D.S., Hu, L. and Irvin, G. (2011). "Emerging transparent electrodes based on thin films of carbon nanotubes, graphene, and metallic nanostructures". *Adv. Mater.*, 23, 1482–1513.

Heo, Y.H., You, D.J., Lee, H., Lee, S. and Lee, H. (2014). "ZnO:B back reflector with high haze and low absorption enhanced triple-junction thin film Si solar modules". *Sol. Energy Mater. Sol. Cells*, 122, 107–111.

Herrando, M. and Markides, C.N. (2016). "Hybrid PV and solar-thermal systems for domestic heat and power provision in the UK: Techno-economic considerations." *Appl. Energy*, 161, 512–532.

Herrero, J. and Guille, C. (2006). "Influence of oxygen in the deposition and annealing atmosphere on the characteristics of ITO thin films prepared by sputtering at room temperature". *Vacuum*, 80, 615–620.

Hirschmann, B., Oreski, G. and Pinter, G. (2014). "Thermo-mechanical characterisation of fluoropolymer films for concentrated solar thermal applications". *Sol. Energy Mater. Sol. Cells*, 130, 615–622.

Hong, C.H., Jo, Y.J., Kim, H.A., Lee, I. and Kwak, J.S. (2011). "Effect of electron beam irradiation on the electrical and optical properties of ITO/Ag/ITO and IZO/Ag/IZO films". *Thin Solid Films*, 519, 6829–6833.

Hong, K., Kim, K., Kim, S., Lee, I., Cho, H., Yoo, S., Choi, H.W., Lee, N., Tak, Y. and Lee, J. (2011). "Optical properties of WO_3/Ag/WO_3 multilayer as

transparent cathode in top-emitting organic light emitting diodes". *J. Phys. Chem. C*, 115, 3453–3459.

Ichino, T., Sasaki, S. and Hasuda, Y. (1986). "Development of high-performance flexible optical solar reflectors". *Electron. Commun. Japan*, 69, 199–205.

Im, H., Jeong, S., Jin, J., Lee, J., Youn, D., Koo, W., Kang, S., Kim, H., Jang, J., Lee, D., Kim, H., Kim, I., Lee, J. and Bae, B. (2016). "Hybrid crystalline-ITO/metal nanowire mesh transparent electrodes and their application for highly flexible perovskite solar cells". *NPG Asia Mater.*, 8, e282-1–8.

Imenes, A.G. and Mills, D.R. (2006). "Spectral beam splitting technology for increased conversion efficiency in solar concentrating systems : a review". *Sol. Energy Mater. Sol. Cells*, 84, 19–69.

Indluru, A. and Alford, T.L. (2009). "Effect of Ag thickness on electrical transport and optical properties of indium tin oxide – Ag – indium tin oxide multilayers". *J. Appl. Phys.*, 105, 123528-1–9.

Inerbaev, T.M., Sahara, R., Mizuseki, H., Kawazoe, Y. and Nakamura, T. (2007). "Interstitial oxygen and dopant atoms arrangement in tin-doped indium oxide". *Mater. Trans.*, 48, 666–669.

Jang, Y., Kim, J. and Byun, D. (2013). "Invisible metal-grid transparent electrode prepared by electrohydrodynamic (EHD)". *J. Phys. D Appl. Phys.*, 46, 155103-1–5.

Jeong, J.-A., Kim and H.-K. (2009). "Low resistance and highly transparent ITO–Ag–ITO multilayer electrode using surface plasmon resonance of Ag layer for bulk-heterojunction organic solar cells". *Sol. Energy Mater. Sol. Cells*, 93, 1801–1809.

Jin, P., Xu, G., Tazawa, M. and Yoshimura, K. (2003). "Design, formation and characterization of a novel multifunctional window with VO_2 and TiO_2 coatings". *Appl. Phys. A*, 77, 455–459.

Jorgensen, G., Kennedy, C., King, D. and Terwilliger, K. (2000). "Optical durability testing of candidate solar mirrors". NREL/TP-520-28110, 1–58.

Jradi, M., Ghaddar, N. and Ghali, K. (2012). "Experimental and theoretical study of an integrated thermoelectric–photovoltaic system for air dehumidification and fresh water production". *Int. J. Energy Res.*, 36(9), 963-974.

Ju, X., Wang, Z., Flamant, G., Li, P. and Zhao, W. (2012). "Numerical analysis and optimization of a spectrum splitting concentration photovoltaic – thermoelectric hybrid system". *Sol. Energy*, 86, 1941–1954.

Jung, Y.S., Lee, D.W. and Jeon, D.Y. (2004). "Influence of DC magnetron sputtering parameters on surface morphology of indium tin oxide thin films". *Appl. Surf. Sci.*" 221, 136–142.

Karazhanov, S.Z., Ravindran, P., Vajeeston, P., Ulyashin, A., Finstad, T.G. and Fjellvåg, H. (2007). "Phase stability, electronic structure, and optical properties of indium oxide polytypes". *Phys. Rev. B*, 76, 75129-1–13.

Karbach, A. and Drechsler, D. (1999). "Atomic force microscopy-a powerful tool for industrial applications". *Surf. interface Anal.*, 27, 401–409.

Kerkache, L., Layadi, A. and Mosser, A. (2009). "Effect of oxygen partial pressure on the structural and optical properties of dc sputtered ITO thin films". *J. Alloys Compd.*, 485, 46–50.

Khusayfan, N.M. and El-Nahass, M.M. (2013). "Study of structure and electro-optical characteristics of indium tin oxide thin films". *Adv. Condens. matter Phys*,. 2013, 408182-1-8.

Kim, H., Horwitz, J.S., Piqué and A., Gilmore, C.H. (2000). "Electrical and optical properties of indium tin oxide thin films grown by pulsed laser deposition". *Appl. Phys. A*, 69, S447-S450.

Kim, H., Seo, K.-W., Kim, H.Y., Choi, J. and Kim, H. (2015). "Direct laser patterning of transparent ITO–Ag-ITO multilayer anodes for organic solar cells".

Appl. Surf. Sci., 328, 215–221.

Kim, J.H., Kang, T., Kwon, S., Na, S., Yoo, Y., Im, H. and Seong, T. (2016). "Transparent conductive ITO/Ag/ITO electrode deposited at room temperature for organic solar cells". *J. Electron. Mater.*, 46, 306–311.

Kim, T.-H., Park, S.-H., Kim, D.-H., Nah, Y.-C., Kim and H.-K. (2017). "Roll-to-roll sputtered ITO/Ag/ITO multilayers for highly transparent and flexible electrochromic applications". *Sol. Energy Mater. Sol. Cells*, 160, 203–210.

Kim, T.H., Choi, B.H., Park, J.S., Lee, S.M., Lee, Y.S. and Park, L.S. (2010). "Transparent conductive ITO/Ag/ITO multilayer films prepared by low temperature process and physical properties". *Mol. Cryst. Liq. Cryst.*, 520, 209/[485]-214/[490].

Kim, Y.S., Park, J.H., Choi, D.H., Jang, H.S., Lee, J.H., Park, H.J., Choi, J.I., Ju, D.H., Lee, J.Y. and Kim, D. (2007). "ITO/Au/ITO multilayer thin films for transparent conducting electrode applications". *Appl. Surf. Sci.*, 254, 1524–1527.

Kostlin, H. and Frank, G. (1982). "Optimization of transparent heat mirrors based on a thin silver film between antireflection films". *Thin Solid Films*, 89, 287–293.

Kumar, A., Porwal, D., Dey, A., Sridhara, N., Mukhopadhyay, A.K. and Sharma, A.K., Barshiliad, H.C. (2015). "Evaluation of elasto-plastic properties of ITO film using combined nanoindentation and finite element approach". *Ceram. Int.*, 42, 1225-1233.

Kumar, A., Siddhanta, S. and Barshilia, H.C. (2016). "Extraordinary high broadband specular transmittance of sodalime glass substrate by vapor phase etching". *Sol. Energy*, 129, 147–155.

Kumar, K.J., Raju, N.R.C. and Subrahmanyam, A. (2011). "Thickness dependent physical and photocatalytic properties of ITO thin films prepared by reactive DC magnetron sputtering". *Appl. Surf. Sci.*, 257, 3075–3080.

Kurdesau, F., Khripunov, G., da Cunha, A.F., Kaelin, M. and Tiwari, A.N. (2006).

"Comparative study of ITO layers deposited by DC and RF magnetron sputtering at room temperature". *J. Non. Cryst. Solids*, 352, 1466–1470.

Kusano, E., Kawaguchi, J. and Enjouji, K. (1986). "Thermal stability of heat reflective films consisting of oxide – Ag – oxide deposited by dc magnetron sputtering". *J. Vac. Sci. Technol. A*, 4, 2907–2910.

Lampert, C.M. (2003). "Large-area smart glass and integrated photovoltaics". *Sol. Energy Mater. Sol. Cells*, 76, 489–499.

Lampert, C.M. (1981). "Heat mirror coatings for energy conserving windows". *Sol. Energy Mater.*, 6, 1–41.

Layani, M., Kamyshny, A. and Magdassi, S. (2014). "Transparent conductors composed of nanomaterials". *Nanoscale*, 6, 5581–5591.

Lee, C., Chen, S. and Jaing, C. (1996). "Optical monitoring of silver-based transparent heat mirrors". *Appl. Opt.*, 35, 5698–5703.

Lee H.L., Flynn N.T. (2006) "X-Ray Photoelectron Spectroscopy. In: Vij D. (Edt.) *Handbook of Applied Solid State Spectroscopy*". Springer, Boston, MA

Lee, H., Na, J., Moon, Y., Seong, T. and Kim, S. (2015). "Design of near-unity transmittance dielectric/Ag/ITO electrodes for GaN-based light-emitting diodes". *Curr. Appl. Phys.*, 15, 833–838.

Lee, H. and Park, O.O. (2006). "The evolution of the structural , electrical and optical properties in indium-tin-oxide thin film on glass substrate by DC reactive magnetron sputtering". *Vacuum*, 80, 880–887.

Lee, H.J., Kang, J.W., Hong, S.H., Song, S.H. and Park, S.J. (2016). "$Mg_xZn_{1-x}O/Ag/Mg_xZn_{1-x}O$ multilayers as high-performance transparent conductive electrodes". *ACS Appl. Mater. Interfaces*, 8, 1565–1570.

Lee, J.Y., Yang, J.W., Chae, J.H., Park, J.H., Choi, J.I., Park, H.J. and Kim, D. (2009). "Dependence of intermediated noble metals on the optical and electrical

properties of ITO/metal/ITO multilayers". *Opt. Commun.*, 282, 2362–2366.

Lewis, J., Grego, S., Chalamala, B., Vick, E. and Temple, D. (2004). "Highly flexible transparent electrodes for organic light-emitting diode-based displays". *Appl. Phys. Lett.*, 85, 3450–3452.

Lin, K.-M., Lin, R.-L., Hsiao, W.-T., Kang, Y.-C., Chou, C.-Y. and Wang, Y.-Z. (2017). "Effects of the structural properties of metal oxide/Ag/metal oxide multilayer transparent electrodes on their optoelectronic performances". *J. Mater. Sci. Mater. Electron.*, 28, 12363–12371.

Liu, H., Chang, C.-H., Lin, C.-C. and Yu, P. (2011). "Haze measurement and scattering analysis of novel indium-tin-oxide (ITO) nanowhiskers for enhance absorption in thin-film solar cells", In *Photovoltaic Specialists Conference (PVSC), 2011 37th IEEE*, 000652-000655.

Mahadik, D.B., Lakshmi, R.V. and Barshilia, H.C. (2015). "High performance single layer nano-porous antireflection coatings on glass by sol–gel process for solar energy applications". *Sol. Energy Mater. Sol. Cells*, 140, 61–68.

Malathy, V., Sivaranjani, S., Vidhya, V.S., Prince, J.J., Balasubramanian, T., Sanjeeviraja, C. and Jayachandran, M. (2009). "Amorphous to crystalline transition and optoelectronic properties of nanocrystalline indium tin oxide (ITO) films sputtered with high rf power at room temperature". *J. Non. Cryst. Solids*, 355, 1508–1516.

Meng, L. and Santos, M.P. (1998). "Properties of indium tin oxide films prepared by rf reactive magnetron sputtering at different substrate temperature". *Thin Solid Films*, 322, 56–62.

Mientus, R. and Ellmer, K. (2001). "Reactive magnetron sputtering of tin-doped indium oxide (ITO) : influence of argon pressure and plasma excitation mode". *Surf. Coatings Technol.*,142–144, 748–754.

Mittal, K.L. and Pizzi, A. (1999). "*Adhesion Promotion Techniques Technological*

Applications". Marcel dekker Inc., New York.

Miyazaki, E. and Yamagata, I. (2009). "Results of space-environment exposure of the flexible optical solar reflector". *J. Spacecr. Rockets*, 46, 28–32.

Mojiri, A., Taylor, R., Thomsen, E. and Rosengarten, G. (2013). "Spectral beam splitting for efficient conversion of solar energy-A review". *Renew. Sustain. Energy Rev.*, 28, 654–663.

Mouchaal, Y., Louarn, G., Khelil, A., Morsli, M., Stephant, N., Bou, A., Abachi, T., Cattin, L., Makha, M., Torchio, P. and Bernède, J.C. (2015). "Broadening of the transmission range of dielectric/metal multilayer structures by using different metals". *Vacuum*, 111, 32–41.

Muneshwar, T.P., Varma, V., Meshram, N., Soni, S. and Dusane, R.O. (2010). "Development of low temperature RF magnetron sputtered ITO films on flexible substrate". *Sol. Energy Mater. Sol. Cells*, 94, 1448–1450.

Nelson, A. and Aharoni, H., (1987). "X-ray photoelectron spectroscopy investigation of ion beam sputtered indium tin oxide films as a function of oxygen pressure during deposition". *J. Vac. Sci. Technol. A*, 5, 231–233.

Osborn, D.E., Chendo, M.A.C., Hamdy, M.A., Luttmann, F., Jacobson, M.R., Macleod, H.A. and Swenson, R. (1986). "Spectral selectivity applied to hybrid concentration systems". *Sol. Energy Mater.*, 14, 299–325.

Padera, F. (2009). "Haze measurements using an integrating sphere." *PerkinElmer UV/Vis/NIR Spectroscopy Resource Page*, November 4, 1-4.

Pammi, S.V.N., Jung, H.J. and Yoon, S.G. (2011). "Low-temperature nanocluster deposition (NCD) for improvement of the structural, electrical, and optical properties of ITO thin films". IEEE Trans. Nanotechnol., 10, 1059–1065.

Parekh, B., Zheng, S., Entenberg, A., Debies, T. and Takacs, G.A. (2007). "Surface modification of poly(tetrafluoroethylene-co-hexafluoropropylene) with vacuum UV radiation from rotating helium dc arc plasmas". *J. Adhes. Sci.*

Technol., 21, 983–998.

Park, H.K., Kang, J.W., Na, S.I., Kim, D.Y. and Kim, H.K. (2009). "Characteristics of indium-free GZO/Ag/GZO and AZO/Ag/AZO multilayer electrode grown by dual target DC sputtering at room temperature for low-cost organic photovoltaics". *Sol. Energy Mater. Sol. Cells*, 93, 1994–2002.

Park, S.-H., Lee, S.-M., Ko, E.-H., Kim, T.-H., Nah, Y.-C., Lee, S.-J.L., Lee, J.H. and Kim, H.-K. (2016). "Roll-to-Roll sputtered ITO/Cu/ITO multilayer electrode for flexible, transparent thin film heaters and electrochromic applications". *Sci. Rep.*, 6, 33868-1-12.

Park, Y.-S., Choi, K.-H. and Kim, H.-K. (2009a). "Room temperature flexible and transparent ITO/Ag/ITO electrode grown on flexile PES substrate by continuous roll-to-roll sputtering for flexible organic photovoltaics". *J. Phys. D. Appl. Phys.*, 42, 235109-1-7.

Park, Y.-S., Park, H.-K., Jeong, J.-A., Kim, H.-K., Choi, K.-H., Na, S.-I. and Kim, D.-Y. (2009b). "Comparative investigation of transparent ITO/Ag/ITO and ITO/Cu/ITO electrodes grown by dual-target dc sputtering for organic photovoltaics". *J. Electrochem. Soc.* 156, H588–H594.

Peng, S., Cao, X., Pan, J., Wang, X., Tan, X., Delahoy, A.E. and Chin, K.K. (2017). "X-ray photoelectron spectroscopy study of indium tin oxide films deposited at various oxygen partial pressures". *J. Electron. Mater.*, 46, 1405–1412.

Pipptin, G., Normand, E. and Woll, S. (2001). "Analysis of Ag/FEP thermal from control blanket performance multiple satellites". *NASA Tech. Reports*, 2001002023, 1–15.

Pracchia, J.A. and Simon, J.M. (1981). "Transparent heat mirrors : influence of the materials on the optical characteristics". *Appl. Opt.*, 20, 251–258.

Preston, C., Xu, Y., Han, X., Munday, J.N. and Hu, L. (2013). "Optical haze of transparent and conductive silver nanowire films." *Nano Res.*, 6, 461–468.

Qiao, Z., Latz, R. and Mergel, D. (2004). "Thickness dependence of In$_2$O$_3$:Sn film growth". *Thin Solid Films*, 466, 250–258.

Quass, M., Eggs, C. and Wulff, H. (1998). " Structural studies of ITO thin films with the Rietveld method". *Thin Solid Films*, 332, 277-281.

Ramamoorthy, K., Kumar, K., Chandramohan, R. and Sankaranarayanan, K. (2006). "Review on material properties of IZO thin films useful as epi-n-TCOs in opto-electronic (SIS solar cells , polymeric LEDs) devices". *Mater. Sci. Eng. B*, 126, 1–15.

Reddy, I.N., Reddy, V.R., Sridhara, N., Rajendra, A., Rao, V.S., Dey, A. and Sharma, A.K. (2013). "Development and environmental stability of ITO thin film for spacecraft application". *Mater. Res. Innov.*, 17, 22–26.

Remya, R. and Deb, B. (2017). "Ultrathin organic spin-on layers on indium tin oxide as a prospective tool for enhanced light throughput". *Mater. Lett.*, 186, 220–223.

Rosen, J. and Warschkow, O. (2009). "Electronic structure of amorphous indium oxide transparent conductors". *Phys. Rev. B*, 80, 1–10.

Rosenwaks, Y., Shikler, R., Glatzel, T. and Sadewasser, S. (2004). "Kelvin probe force microscopy of semiconductor surface defects". Phys. Rev. B, 70, 85320-1–7.

Sahu, D.R., Lin S.Y. and Huang, J.L. (2008). "Investigation of conductive and transparent Al-doped ZnO/Ag/Al-doped ZnO multilayer coatings by electron beam evaporation". *Thin Solid Films*, 516, 4728–4732.

Sattler, K.D. (2016). "*Carbon Nanomaterials Source Book*". CRC Press, Boca Raton.

Schmidt, R.E. (1980). "Charging control techniques", *in: NASA. Lewis Research Center Spacecraft Charging Technol.,* pp. 267–286.

Selvakumar, N., Biswas, A., Rajaguru, K., Gouda, G.M. and Barshilia, H.C. (2015). "Nanometer thick tunable AlHfN coating for solar thermal applications: transition from absorber to antireflection coating". *Sol. Energy Mater. Sol. Cells*, 137, 219–226.

Sharma, A., Hotchkiss, P.J., Marder, S.R., Kippelen, B., Sharma, A., Hotchkiss, P.J., Marder, S.R. and Kippelen, B. (2009). "Tailoring the work function of indium tin oxide electrodes in electrophosphorescent organic light-emitting diodes". *J. Appl. Phys.*, 105, 084507-1-6.

Sharma, A.K. and Sridhara, N. (2012). "Degradation of thermal control materials under a simulated radiative space environment". *Adv. Sp. Res.*, 50, 1411–1424.

Shou, C., Luo, Z., Wang, T., Shen, W., Rosengarten, G., Wei, W., Wang, C., Ni, M. and Cen, K. (2012). "Investigation of a broadband TiO_2/SiO_2 optical thin-film filter for hybrid solar power systems". *Appl. Energy,* 92, 298–306.

Sierros, K.A., Morris, N.J., Ramji, K. and Cairns, D.R. (2009). "Stress-corrosion cracking of indium tin oxide coated polyethylene terephthalate for flexible optoelectronic devices". *Thin Solid Films*, 517, 2590–2595.

Singh, D., Singh, S., Kumar, U., Srinivasa, R.S. and Major, S.S. (2014). "Transparent conducting Ga-doped ZnO thin fi lms grown by reactive co-sputtering of Zn and GaAs". *Thin Solid Films,* 555, 126–130.

Smith, B.C. (2011). "*Fundamentals Of Fourier Transform Infrared Spectroscopy*". CRC Press, Boca Raton.

Smits, F.M. (1958). "Measurement of sheet resistivities with the four-point probe". *Bell Syst. Tech. J.*, 37, 711–718.

Soule, E. and Wood, E. (1986). "Heat-mirror spectral profile optimization for TCS hybrid solar conversion". *Opt. Mater. Technol. Energy Effic. Sol. Energy Convers.*, 653, 172–180.

Soum-Glaude, A., Tian, L., Blanquet, E., Brize, V., Cagnon, L., Giusti, G., Salhi,

R., Daniele, S., Ternon, C. and Bellet, D. (2012) "Atomic layer deposition of TiO$_2$ ultrathin films on 3D substrates for energy applications". *Mater. Res. Soc. Symp. Proc.*, 1439, 63-68.

Stadler, A. (2012). "Transparent Conducting Oxides—An Up-To-Date Overview". *Materials* 5, 661–683.

Subrahmanyam, A. and Barik, U.K., (2006). "Electrical and optical properties of silver doped indium oxide thin films prepared by reactive DC magnetron sputtering". *J. Phys. Chem. Solids*, 67, 1518–1523.

Sugiyama, K., Ishii, H., Ouchi, Y. and Seki, K. (2000). "Dependence of indium – tin – oxide work function on surface cleaning method as studied by ultraviolet and x-ray photoemission spectroscopies." *J. Appl. Phys.*, 87, 295–298.

Sun, K., Zhou, W., Tang, X., Huang, Z., Lou, F. and Zhu, D. (2011). "Effect of the heat treatment on the infrared emissivity of indium tin oxide (ITO) films". *Appl. Surf. Sci.*, 257, 9639–9642.

Tahar, R.B.H., Ban, T., Ohya, Y. and Takahashi, Y. (1998). "Tin doped indium oxide thin films: electrical properties". *J. Appl. Phys.*, 83, 2631–2645.

Teissier, A., Dudon, J., Aubert, P., Vidal, F., Ramaury, S., Crouzet, J. and Chevrot, C. (2012). "Feasibility of conducting semi-IPN with variable electro-emissivity : a promising way for spacecraft thermal control". *Sol. Energy Mater. Sol. Cells*, 99, 116–122.

Tetsuka, H., Ebina, T., Tsunoda, T., Nanjo, H. and Mizukami, F. (2008). "Fabrication and characterization of ITO thin films on heat-resistant transparent flexible clay films". *Surf. Coatings Technol.*, 202, 2955–2959.

Thermal Control Overview [WWW Document], www.sheldahl.com/documents/Thermal%20Control%20Overview.pdf.

Tran, D., Lu, H. and Lin, C. 2015. "Effects of cyclic deformation on conductive characteristics of indium tin oxide thin fi lm on polyethylene terephthalate

substrate". *Surf. Coat. Technol.*, 283, 298–310.

Tuna, O., Selamet, Y., Aygun, G. and Ozyuzer, L. (2010). "High quality ITO thin films grown by dc and RF sputtering without oxygen". *J. Phys. D. Appl. Phys.*, 43, 55402.

Uzu, H., Ichikawa, M., Hino, M., Nakano, K., Meguro, T., Hernandez, J.L., Kim, S., Park, N.-G. and Yamamoto, K. (2015). "High efficiency solar cells combining a perovskite and a silicon heterojunction solar cells via an optical splitting system". *Appl. Phys. Lett.*, 106, 013506-1-4.

Vorobiev, Y., Gonzalez-Hernandez, J., Vorobiev, P. and Bulat, L. (2006). "Thermal-photovoltaic solar hybrid system for efficient solar energy conversion". *Sol. Energy*, 80, 170–176.

Wang, F., Du, R., Ren, Q., Wei, C., Zhao, Y. and Zhang, X. (2017). "Improving crystallization and electron mobility of indium tin oxide by carbon dioxide and hydrogen dual-step plasma treatment". *Appl. Surf. Sci.*, 426, 856–863.

Wang, F., Wu, M.Z., Wang, Y.Y., Yu, Y.M., Wu, X.M. and Zhuge, L.J. (2013). "Influence of thickness and annealing temperature on the electrical, optical and structural properties of AZO thin films". Vacuum, 89, 127–131.

Wang, N., Han, L., He, H., Park, N.-H. and Koumoto, K. (2011). "A novel high-performance photovoltaic–thermoelectric hybrid device". *Energy Environ. Sci.*, 4, 3676–3679.

Wang, Z., Cai, X., Chen, Q. and Li, L. (2006). "Optical properties of metal-dielectric multilayers in the near UV region". Vacuum, 80, 438–443.

Wheeler, D. and Pepper, V. (1983). "Use of hight L.E.T. radiation to improve adhesion of metals to polytetrafluoroethylene". *NASA Tech. Memo.*, 83413, 1-14.

Yan, L., Song, Y., Zhou, Y., Song, B. and Li, Y. (2015). "Effect of PEI cathode interlayer on work function and interface resistance of ITO electrode in the inverted polymer solar cells". *Org. Electron.*, 17, 94–101.

Yang, D. and Yin, H., (2011). "Energy conversion efficiency of a novel hybrid solar system for photovoltaic, thermoelectric, and heat utilization". *IEEE Trans. Energy Convers.*, 26, 662–670.

Yu, X., Marks, T.J. and Facchetti, A. (2016). "Metal oxides for optoelectronic applications". *Nat. Mater.*, 15, 383–396.

Yuste, M., Galindo, R. E., Carvalho, S., Albella, J.M. and Sanchez, O. (2011) " Improving the visible transmittance of low-e titanium nitride based coatings for solar thermal applications" *App. Surf. Sci.,* 258, 1784-1788.

Zhang, L., Zhou, Y., Guo, L., Zhao, W., Barnes, A., Zhang, H., Eaton, C., Zheng, Y., Brahlek, M., Haneef, H.F., Podraza, N.J., Chan, M.H.W., Gopalan, V., Rabe, K.M. and Engel-herbert, R., (2015). "Correlated metals as transparent conductors". *Nat. Mater.*, 15, 204–210.

Zhang, X., Zhao, L., Fan, C., Liang, Z. and Han, P. (2012). "Effects of oxygen vacancy on the electronic structure and absorption spectra of bismuth oxychloride. *Comput. Mater. Sci.* 61, 180–184.

Zhou, W. and Wang, Z.L. (2006). "Scanning Microscopy For Nanotechnology". Springer, New York.

Zilberberg, K. and Riedl, T. (2016). "Metal-nanostructures – a modern and powerful platform to create transparent electrodes for thin-film photovoltaics". *J. Mater. Chem. A 4*, 14481–14508.

Zimmermann, Y., Niewersch, C., Lenz, M., Kül, Z., Corvini, P.F., Schaeffer, A. and Wintgens, T. (2014). "Recycling of indium from CIGS photovoltaic cells : potential of combining acid-resistant nanofiltration with liquid-liquid-extraction". *Environ. Sci. Technol.*, 48, 13412–13418.

Zudans, I., Paddock, J.R., Kuramitz, H., Maghasi, A.T., Wansapura, C.M., Conklin, S.D., Kaval, N., Shtoyko, T., Monk, D.J., Bryan, S.A., Hubler, T.L., Richardson, J.N., Seliskar, C.J. and Heineman, W.R. (2004). "Electrochemical and

optical evaluation of noble metal – and carbon – ITO hybrid optically transparent electrodes". *J. Electroanal. Chem.*, 565, 311–320.

CURRICULUM VITAE

PERSONAL INFORMATION:

- Full name   : Sibin Kunhi Purayil
- Date of birth   : 21 December 1988
- Gender   : Male
- Place of birth   : Mayyil, Kannur
- Citizenship   : Indian
- Marital status   : Single

Permanent Address:

K.P.N. HOUSE, POST M M BAZAR

KANNUR, KERALA, INDIA, PIN-670306

Mobile. (+91)-8951870381, E-mail: sibinkp@gmail.com

Researchgate ID: https://www.researchgate.net/profile/Sibin_K_P

Academic Qualification:

- 2009-2011: **Master of Science in Physics**, Department of Physics, National Institute of Technology Karnataka (*NITK*), Surathkal, Karnataka, India.
- 2006-2009: **Bachelor of Science in Physics, Chemistry and Mathematics**, St. Aloysius College, Mangalore, Mangalore University, Karnataka, India.
- 2004-2006: **Plus Two (Science)**, Government Higher Secondary School Mathamangalam, Kannur, Kerala, India.
- 2004   : **S.S.L.C**. Government Hıgher Secondary School, Mathamangalam, Kannur, Kerala, India

Work experience:

➢ Project Assistant (Gr. III) (September 2017-December 2017), CSIR-National Aerospace Laboratories (NAL), Bangalore.

➢ Senior Research Fellow (August 2015-August 2017), CSIR-National Aerospace Laboratories (NAL), Bangalore.

➢ Junior Research Fellow (August 2013-August 2015), CSIR-National Aerospace Laboratories (NAL), Bangalore.

➢ Research trainee (May 2012- May 2013), CSIR-National Aerospace Laboratories (NAL), Bangalore.

Research Publications:

Articles in International Journals: 6

Articles in International Proceedings: 1